



# **NAVAL POSTGRADUATE SCHOOL**

**MONTEREY, CALIFORNIA**

## **DISSERTATION**

**FINE SURFACE CONTROL OF FLEXIBLE SPACE  
MIRRORS USING ADAPTIVE OPTICS AND ROBUST  
CONTROL**

by

Daniel C. Burtz

March 2009

Dissertation Supervisor:

Brij N. Agrawal

**Approved for public release, distribution is unlimited.**

THIS PAGE INTENTIONALLY LEFT BLANK

<b>REPORT DOCUMENTATION PAGE</b>			Form Approved OMB No. 0704-0188	
Public reporting burden for this collection of information is estimated to average 1 hour per response, including the time for reviewing instruction, searching existing data sources, gathering and maintaining the data needed, and completing and reviewing the collection of information. Send comments regarding this burden estimate or any other aspect of this collection of information, including suggestions for reducing this burden, to Washington headquarters Services, Directorate for Information Operations and Reports, 1215 Jefferson Davis Highway, Suite 1204, Arlington, VA 22202-4302, and to the Office of Management and Budget, Paperwork Reduction Project (0704-0188) Washington DC 20503.				
<b>1. AGENCY USE ONLY (Leave blank)</b>		<b>2. REPORT DATE</b> March 2009	<b>3. REPORT TYPE AND DATES COVERED</b> Dissertation	
<b>4. TITLE AND SUBTITLE:</b> Fine Surface Control of Flexible Space Mirrors Using Adaptive Optics and Robust Control			<b>5. FUNDING NUMBERS</b>	
<b>6. AUTHOR(S)</b> Daniel C. Burtz				
<b>7. PERFORMING ORGANIZATION NAME(S) AND ADDRESS(ES)</b> Naval Postgraduate School Monterey, CA 93943-5000			<b>8. PERFORMING ORGANIZATION REPORT NUMBER</b>	
<b>9. SPONSORING / MONITORING AGENCY NAME(S) AND ADDRESS(ES)</b> N/A			<b>10. SPONSORING / MONITORING AGENCY REPORT NUMBER</b>	
<b>11. SUPPLEMENTARY NOTES</b> The views expressed in this thesis are those of the author and do not reflect the official policy or position of the Department of Defense or the U.S. Government.				
<b>12a. DISTRIBUTION / AVAILABILITY STATEMENT</b> Approved for public release; distribution is unlimited			<b>12b. DISTRIBUTION CODE</b>	
<b>13. ABSTRACT (maximum 200 words)</b> <p>Future space telescopes will contain lightweight, flexible, segmented mirrors. Traditional control approaches for mirror alignment and shape control may be inadequate due to flexibilities and low natural frequencies. Using adaptive optics for space telescopes presents a possible solution. This research proposes innovative <math>H_\infty</math> robust control techniques for these types of systems. An <math>H_\infty</math> controller is synthesized for a complex analytical model with 997 inputs, 936 outputs, and 332 states. To accomplish this, a new technique for model reduction using Zernike polynomials was developed. The <math>H_\infty</math> controller was able to achieve a minimum 15 Hz control bandwidth. The previous integral controller was unable to meet the 10 Hz bandwidth requirement. The <math>H_\infty</math> design process used was validated on a simpler adaptive optics testbed. The experimental verification also showed that the robust control techniques outperformed the classical control techniques in the presence of disturbances.</p> <p>The significant contributions are a Zernike polynomial method for model reduction, robust controller synthesis for a complex adaptive optics analytical model, and experimental verification on an AO testbed. Although the robust control design is more complex, it provides improved performance in the presence of uncertainty in the disturbances and modeling.</p>				
<b>14. SUBJECT TERMS</b> Robust control, adaptive optics, segmented mirrors, Shack-Hartmann wavefront sensor, space telescopes, $H_\infty$ , flexible structures			<b>15. NUMBER OF PAGES</b> 115	
			<b>16. PRICE CODE</b>	
<b>17. SECURITY CLASSIFICATION OF REPORT</b> Unclassified	<b>18. SECURITY CLASSIFICATION OF THIS PAGE</b> Unclassified	<b>19. SECURITY CLASSIFICATION OF ABSTRACT</b> Unclassified	<b>20. LIMITATION OF ABSTRACT</b> UU	

THIS PAGE INTENTIONALLY LEFT BLANK

**Approved for public release; distribution is unlimited**

**FINE SURFACE CONTROL OF FLEXIBLE SPACE MIRRORS USING ADAPTIVE  
OPTICS AND ROBUST CONTROL**

Daniel C. Burtz  
Major, United States Air Force  
B.S., United States Air Force Academy, 1997  
M.Eng., University of Colorado, 1998

Submitted in partial fulfillment of the  
requirements for the degree of

**DOCTOR OF PHILOSOPHY IN ASTRONAUTICAL ENGINEERING**

from the

**NAVAL POSTGRADUATE SCHOOL  
March 2009**

Author:

\_\_\_\_\_  
Daniel C. Burtz

Approved by:

\_\_\_\_\_  
Brij N. Agrawal  
Distinguished Professor of Mechanical  
and Astronautical Engineering  
Dissertation Supervisor and Committee  
Chair

\_\_\_\_\_  
Marcello Romano  
Assistant Professor of Mechanical  
and Astronautical Engineering

\_\_\_\_\_  
Oleg Yakimenko  
Associate Professor of Mechanical and  
Astronautical Engineering

\_\_\_\_\_  
Roberto Cristi  
Professor of Electrical and  
Computer Engineering

\_\_\_\_\_  
Ty Martinez  
Naval Research Laboratory

Approved by:

\_\_\_\_\_  
Knox Millsaps, Chair, Department of Mechanical and Astronautical Engineering

Approved by:

\_\_\_\_\_  
Douglas Moses, Associate Provost for Academic Affairs

THIS PAGE INTENTIONALLY LEFT BLANK

## ABSTRACT

Future space telescopes will contain lightweight, flexible, segmented mirrors. Traditional control approaches for mirror alignment and shape control may be inadequate due to flexibilities and low natural frequencies. Using adaptive optics for space telescopes presents a possible solution. This research proposes innovative  $H_\infty$  robust control techniques for these types of systems. An  $H_\infty$  controller is synthesized for a complex analytical model with 997 inputs, 936 outputs, and 332 states. To accomplish this, a new technique for model reduction using Zernike polynomials was developed. The  $H_\infty$  controller was able to achieve a minimum 15 Hz control bandwidth. The previous integral controller was unable to meet the 10 Hz bandwidth requirement. The  $H_\infty$  design process used was validated on a simpler adaptive optics testbed. The experimental verification also showed that the robust control techniques outperformed the classical control techniques in the presence of disturbances.

The significant contributions are a Zernike polynomial method for model reduction, robust controller synthesis for a complex adaptive optics analytical model, and experimental verification on an AO testbed. Although the robust control design is more complex, it provides improved performance in the presence of uncertainty in the disturbances and modeling.

THIS PAGE INTENTIONALLY LEFT BLANK



# TABLE OF CONTENTS

<b>I.</b>	<b>INTRODUCTION.....</b>	<b>1</b>
A.	<b>MOTIVATION .....</b>	<b>1</b>
B.	<b>ADAPTIVE OPTICS SYSTEMS .....</b>	<b>6</b>
1.	<b>Wavefront Sensors .....</b>	<b>8</b>
2.	<b>Adaptive Optical Components .....</b>	<b>9</b>
3.	<b>Control Algorithms .....</b>	<b>11</b>
C.	<b>OBJECTIVES .....</b>	<b>12</b>
1.	<b>Analytical .....</b>	<b>12</b>
2.	<b>Experimental .....</b>	<b>12</b>
D.	<b>CURRENT STATE OF RESEARCH IN THE FIELD .....</b>	<b>13</b>
E.	<b>DISSERTATION OUTLINE .....</b>	<b>14</b>
F.	<b>CONTRIBUTIONS .....</b>	<b>15</b>
<b>II.</b>	<b>TESTBED AND MODEL OVERVIEW.....</b>	<b>17</b>
A.	<b>SEGMENTED SPACE TELESCOPE MODEL.....</b>	<b>17</b>
1.	<b>Model Purpose.....</b>	<b>17</b>
2.	<b>Model Complexity .....</b>	<b>17</b>
B.	<b>ADAPTIVE OPTICS TESTBED .....</b>	<b>20</b>
1.	<b>Layout .....</b>	<b>20</b>
2.	<b>Hardware .....</b>	<b>23</b>
a.	<i>Laser .....</i>	<i>24</i>
b.	<i>Micromachined Deformable Mirror .....</i>	<i>24</i>
c.	<i>Shack-Hartmann Wavefront Sensor .....</i>	<i>25</i>
d.	<i>Control Computer .....</i>	<i>25</i>
<b>III.</b>	<b>ROBUST CONTROL .....</b>	<b>27</b>
A.	<b>TRADITIONAL CONTROL APPROACH .....</b>	<b>27</b>
B.	<b>JUSTIFICATION FOR ROBUST CONTROL .....</b>	<b>29</b>
C.	<b>MATHEMATICAL FOUNDATIONS.....</b>	<b>31</b>
1.	<b>Norms .....</b>	<b>31</b>
2.	<b>Singular Values .....</b>	<b>31</b>
3.	<b>Small Gain Theorem.....</b>	<b>32</b>
4.	<b>Sensitivity Functions.....</b>	<b>33</b>
5.	<b>Weighting Functions.....</b>	<b>34</b>
D.	<b>MODEL UNCERTAINTY.....</b>	<b>36</b>
E.	<b>CONTROLLER SYNTHESIS.....</b>	<b>38</b>
<b>IV.</b>	<b>MODEL REDUCTION TECHNIQUES .....</b>	<b>43</b>
A.	<b>INPUT/OUTPUT REDUCTION.....</b>	<b>43</b>
1.	<b>Singular Value Decomposition.....</b>	<b>43</b>
2.	<b>Zernike Polynomials .....</b>	<b>44</b>
B.	<b>STATE REDUCTION WITH HANKEL SINGULAR VALUES.....</b>	<b>49</b>
<b>V.</b>	<b>APPLICATION TO SEGMENTED SPACE TELESCOPE MODEL .....</b>	<b>51</b>

A.	MODEL REDUCTION .....	51
1.	SVD Only Reduction.....	51
2.	Zernike Reduction .....	54
3.	State Reduction .....	58
B.	ROBUST CONTROLLER SYNTHESIS .....	59
C.	PERFORMANCE AND STABILITY MARGINS .....	61
D.	ANALYTICAL RESULTS .....	70
1.	System Performance .....	72
2.	Disturbance Rejection .....	74
VI.	EXPERIMENTAL APPLICATION TO ADAPTIVE OPTICS TESTBED .....	77
A.	SYSTEM IDENTIFICATION .....	77
B.	ROBUST CONTROLLER SYNTHESIS .....	77
C.	EXPERIMENTAL RESULTS.....	81
1.	System Performance .....	81
2.	Disturbance Rejection .....	85
VII.	SUMMARY, FUTURE WORK, AND CONCLUSIONS.....	91
A.	SUMMARY .....	91
B.	FUTURE WORK .....	92
C.	CONCLUSIONS .....	93
	LIST OF REFERENCES .....	95
	INITIAL DISTRIBUTION LIST .....	99

## LIST OF FIGURES

Figure 1	Angular Resolution Geometry. ....	3
Figure 2	James Webb Space Telescope From [2]. ....	5
Figure 3	Generalized AO System From [3]. ....	7
Figure 4	Lenslet Array Spot Formation From [3]. ....	9
Figure 5	Mirror Segment and Lenslet Orientation. ....	19
Figure 6	Uncorrected AO Testbed Image. ....	21
Figure 7	Corrected AO Testbed Image. ....	21
Figure 8	AO Testbed Schematic From [3]. ....	22
Figure 9	AO Testbed Picture. ....	22
Figure 10	MMDM Schematic Section From [19]. ....	24
Figure 11	MMDM Actuator Locations and Positioning From [19]. ....	25
Figure 12	Standard Robust Control System. ....	29
Figure 13	System with Uncertainty. ....	32
Figure 14	Robust Control Loopshaping From [20]. ....	34
Figure 15	Schematic of System with Weighting Functions. ....	35
Figure 16	Additive Uncertainty From [20]. ....	36
Figure 17	Multiplicative Uncertainty From [20]. ....	36
Figure 18	Structured and Unstructured Model Uncertainty Sources From [20]. ....	37
Figure 19	Augmented Nominal 2-Input, 2-Output Plant. ....	39
Figure 20	Augmented Plant and Controller. ....	41
Figure 21	Twenty Common Zernike Modes From [25]. ....	45
Figure 22	Singular Values from Original System. ....	52
Figure 23	Mirror Segment and Lenslet Orientation. ....	55
Figure 24	Singular Values from Zernike Output Reduced System. ....	57
Figure 25	Hankel Singular Values. ....	59
Figure 26	Model Weighting Function Bode Plot. ....	60
Figure 27	Closed Loop Poles for SVD only Reduced Model. ....	62
Figure 28	Closed Loop Poles for Zernike Polynomial Reduced Model. ....	62
Figure 29	Imaginary Axis Vicinity for SVD Reduction Closed Loop Poles. ....	63
Figure 30	Imaginary Axis Vicinity for Zernike Polynomial Reduction Closed Loop Poles. ....	63
Figure 31	Singular Values for Original System Model, $G_{red}$ . ....	64
Figure 32	Singular Values for $H_\infty$ Controller, $K_{SVD}$ . ....	65
Figure 33	Singular Values for $H_\infty$ Controller, $K_{Zern}$ . ....	66
Figure 34	Open Loop System Singular Values for $GK_{SVD}$ . ....	67
Figure 35	Open Loop System Singular Values for $GK_{Zern}$ . ....	67
Figure 36	Closed Loop System Singular Values for $GK_{SVD}$ . ....	68
Figure 37	Closed Loop System Singular Values for $GK_{Zern}$ . ....	69
Figure 38	Segmented Space Telescope Controller Validation Model. ....	70
Figure 39	Disturbance Input Representation. ....	72

Figure 40	Step Input for SVD Only Reduced Model.....	73
Figure 41	Step Input for Zernike Polynomial Reduced Model.....	73
Figure 42	Simulation Model with Zernike Coefficient Conversion.....	75
Figure 43	Zernike Polynomial Coefficients in Presence of Random Disturbance for SVD Reduced Controller.....	75
Figure 44	Zernike Polynomial Coefficients in Presence of Random Disturbance for Zernike Reduced Controller.....	76
Figure 45	AO Testbed Robust Controller Weighting Functions.....	79
Figure 46	AO Testbed Controller Singular Values.....	80
Figure 47	AO Testbed Open Loop Singular Values.....	80
Figure 48	AO Testbed Closed Loop Singular Values.....	81
Figure 49	Classical Controller Peak-to-Valley Wavefront Error.....	83
Figure 50	Classical Controller RMS Wavefront Error.....	83
Figure 51	Robust Controller Peak-to-Valley Wavefront Error.....	84
Figure 52	Robust Controller RMS Wavefront Error.....	85
Figure 53	Classical Controller Peak-to-Valley Wavefront Error with 1.3963 Hz Disturbance.....	86
Figure 54	Classical Controller RMS Wavefront Error with 1.3963 Hz Disturbance.....	87
Figure 55	Robust Controller Peak-to-Valley Wavefront Error with 1.3963 Hz Disturbance.....	87
Figure 56	Robust Controller RMS Wavefront Error with 1.3963 Hz Disturbance.....	88
Figure 57	Classical Controller Peak-to-Valley Wavefront Error with 6.2832 Hz Disturbance.....	88
Figure 58	Classical Controller RMS Wavefront Error with 6.2832 Hz Disturbance.....	89
Figure 59	Robust Controller Peak-to-Valley Wavefront Error with 6.2832 Hz Disturbance.....	89
Figure 60	Robust Controller RMS Wavefront Error with 6.2832 Hz Disturbance.....	90

## LIST OF TABLES

Table 1	Segmented Space Telescope Input/Output Summary.....	20
Table 2	Table of Zernike Polynomials From [24]. .....	47
Table 3	Closed Loop Poles Closest to $j\omega$ Axis.....	64
Table 4	AO Testbed Disturbance Rejection Simulations. ....	90

THIS PAGE INTENTIONALLY LEFT BLANK

## **ACKNOWLEDGMENTS**

I would like to thank the members of my committee for their encouragement and guidance in preparing this dissertation. They have devoted numerous hours to instructing me, and providing constructive comments to improve my final product. I also owe a special debt of gratitude to my fellow researchers in the Spacecraft Research and Design Center, Professor Jae Jun Kim, Dr. Hyungjoo Yoon, and Dr. Anne Marie Johnson. Despite having their own work to do, they were always willing to stop what they were doing to help me solve a problem or understand a concept more clearly. Their assistance was invaluable.

Special thanks also goes to Dr. Alain Carrier and his colleagues for their insights into the analytical segmented space telescope model. His availability to answer my questions and provide suggestions for areas needing further research was quite helpful.

Dr. Sergio Restaino and Dr. Ty Martinez from the Naval Research Lab were instrumental in the setup and operation of the testbed hardware. Capt Matt Allen, USAF, did much of the initial development work on the testbed algorithms.

Finally, I am extremely grateful to my wife Angie, partly for her efforts in helping to edit my dissertation, but mostly for helping keep me sane during this process and shouldering the majority of the work of raising two small boys while I conducted my research.

THIS PAGE INTENTIONALLY LEFT BLANK



# I. INTRODUCTION

## A. MOTIVATION

Optical systems have long been used for imagery and intelligence gathering for both civilian and military purposes. Since the first recorded use of telescopes in the early 17th century, the goal has been to improve the technology that would give the user the advantage of increased resolution at greater distance. Some of the early pioneers in the field such as Galileo and Newton experimented with refractive (lens) and reflective (mirror) systems. As the technologies allowing remote optical sensing evolved, military commanders on the battlefield, as well as naval commanders at sea, found new applications for them. Naturally, the military application of these tactics evolved with the advent of air and space vehicles from which to conduct reconnaissance. The trend has continually moved towards smaller angular resolution at increased distance.

As shown in Equation (1.1), the diffraction limited angular resolution using Raleigh criterion, as denoted by  $\alpha_R$ , is a function of the wavelength of the electromagnetic radiation, approximately 600 nanometers for visible light, and the diameter,  $D$ , of the light gathering aperture

$$\alpha_R = 1.22\lambda / D \quad (1.1)$$

The angular diffraction limited resolution is usually measured in radians, arcseconds, or some equivalent measure. Since the wavelength being observed is usually fixed, the aperture diameter is the only remaining variable factor. Obviously, there are physical size limitations to which the primary optic in a telescope can be manufactured.

The most obvious limitation arises from the physical process of machining the lens or mirror. Ideally, a reflective mirror would have a parabolic shape to minimize the amount of aberration resulting from the reflection process. In practice, however, spherical mirrors are much easier to machine, giving rise to one of the most common optical aberrations, appropriately known as spherical. Additional constraints on the diameter of the primary optic arise in the support structure used to encase or hold the optic stationary. Large telescope optics will often be quite rigid, a design characteristic to

prevent sagging or warping of the optical surface due to gravitational or other inertial forces. Mechanisms to support and move these heavy optics can themselves become quite large and cumbersome.

This support structure problem has less consequence for ground-based observing platforms, but for airborne platforms, weight becomes more important. This realization becomes immensely important when considering space-based platforms where the cost per pound to orbit is prohibitively high. Space platforms are perhaps even more limited by size constraints than weight constraints. The basic shape of every launch vehicle that launches spacecraft into orbit is cylindrical. Even the space shuttle orbiter, whose exterior is *not* cylindrical, has a cylindrical payload bay that carries the spacecraft aloft. The diameter of the rocket body becomes a physical limitation for the size of the primary optic of a space-based telescope. Considering the distance involved in orbital altitudes, this diameter is certainly less than that needed to achieve the angular resolution desired by image analysts.

Despite these challenges, the attraction of space-based imagery, and in particular, high altitude imagery, is quite appealing. Beyond the immediate advantages of a wider field of view and higher vantage point, a high altitude orbit also results in lower orbital speeds, which translates to increased dwell time over a given part of the earth. This can be taken to the extreme of the geostationary orbit, which would maintain continual presence over a point above the equator and have nearly a third of the surface of the planet in its field of view at any time. The tradeoff comes in the distance to geostationary altitude. Whereas a low earth orbiting satellite might orbit a few hundred kilometers above the surface, geostationary spacecraft require an altitude of approximately 36,000 km. The effect of this distance is illustrated in Figure 1 and Equation (1.2), where the angular resolution is equal to that from Equation (1.1), and  $R$  represents, in this case, distance from the orbital altitude to the surface of the earth.

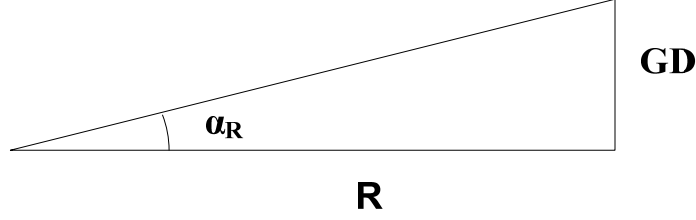


Figure 1 Angular Resolution Geometry.

$$R\alpha_R = GD \quad (1.2)$$

where  $GD$  is the ground resolution.

Although increasing altitude does not decrease the angular resolution per se, it does increase the minimum separation needed to differentiate two objects on the surface. Said another way, space telescopes at geostationary altitudes require much larger diameter primary optics to differentiate the same level of ground detail as low earth orbiting satellites. Clearly, a way is needed to combine the benefits of better image quality obtained from lower orbits with that of improved dwell time from higher orbits. Multiple solutions exist and are not limited to individual spacecraft. A concept of operations could be developed which utilizes a constellation of spacecraft at varying altitudes to maximize resolution and dwell time over particular areas of interest. Another solution involves achieving primary optic diameters larger than would fit inside a conventional payload fairing, by segmenting, and deploying on orbit. These segmentation techniques will be the topic of this dissertation.

Traditional telescopes utilize a spherical, continuous face sheet mirror. Its size is constrained, however, by the aforementioned limitations. If instead of a continuous face sheet, the primary optic can be made of a series of smaller segments, these segments can be folded or packaged in some way that the segments are deployed or assembled into a large diameter mirror after the rocket's payload fairings have been jettisoned and the spacecraft is on-orbit. The concept is not unlike that which is done with spacecraft solar arrays, which are often folded like an accordion before launch and unfolded once in

space. To be clear, though, the on-orbit assembly of mirror segments is vastly more complex than that of solar arrays, communications antennas, or any other spacecraft structures deployed on-orbit.

The added complexity stems partly from the fact that mirror segments are extremely delicate components with sensitive optical coatings, but primarily from the precise alignment criteria required of the segments. Recall that the wavelength of visible light is on the order of 600 nm. With wavelengths this small, even a slight misalignment of mirror segments can cause aberrations to degrade image quality beyond what is useful. This problem is so daunting in fact, that a separate area of research is being devoted entirely to the problem of initial alignment for segmented optics [1]. Once the coarse initial alignment has been successfully accomplished, only fine adjustments will be necessary to account for remaining optical aberrations. More on those aberrations will be discussed later. This research will focus only on the finer surface corrections after initial alignment has been completed.

Numerous folding and deploying scenarios could be considered for segmented optics. One important design criterion is the electromagnetic radiation wavelength collected through the aperture. The emphasis here will be on visible wavelengths. A current example of a space telescope under construction that will utilize segmented optics is NASA's James Webb Space Telescope, an infrared astronomy telescope planned for launch in 2013. An artist's concept of this spacecraft is shown in Figure 2. Notice the gold-colored primary optic, which is comprised of 18 hexagonal segments. The launch configuration of this spacecraft calls for the three leftmost and three rightmost segments to be folded back in order to fit within the payload fairings. Two hinged motions will deploy those six segments along with a host of other deployments from the launch configuration involving, but not limited to, the struts supporting the secondary optic and the blue and red sun shield. Although the primary optic deployment may seem rather simple, it is important to remember that the remaining twelve segments are still individual segments, and vibrations and stresses of the launch environment will make for a very challenging initial alignment problem.

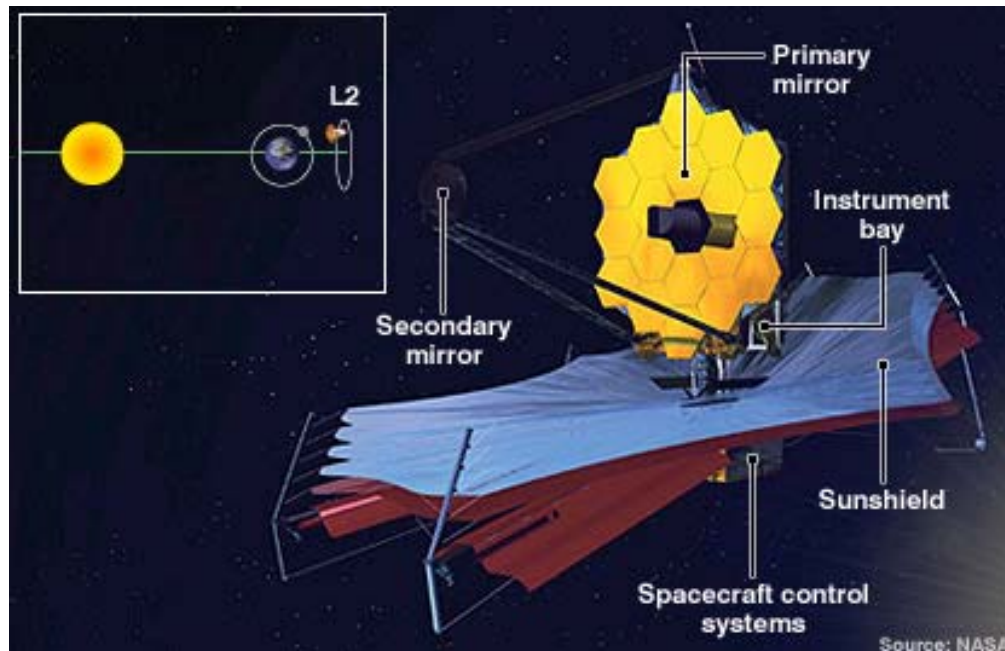


Figure 2 James Webb Space Telescope From [2].

Another challenging aspect of the space telescope observation platform involves the structural properties of the primary optic. Spacecraft designers are constantly attempting to decrease the mass of the onboard components to reduce the costs of placing them into orbit. Large, rigid, monolithic optics work fine for most terrestrial applications, but their weight becomes prohibitive for spacecraft operations. Whether segmented or a continuous face sheet, space telescope optics are most economical when lightweight. Being lightweight causes particular challenges in the control and alignment of mirror segments or other means of mirror shape control. The natural frequencies will be lower, resulting in control and structure interactions.

Both segmented and continuous face sheet mirrors will have actuators attempting to correct the mirror shape due to measured aberrations. If the bandwidth controlling these actuators overlaps, or even falls close to the natural frequencies of the structure, then the controller may actually exacerbate the aberrations. Typically, large ground-based mirrors have their lowest natural frequency well over 1000 Hz so control bandwidths below 100 Hz have no chance of exciting natural frequencies. With segmented mirrors, such as the one researched in this dissertation, the lowest natural

frequency can be around 30 Hz, which becomes a concern for the control system designer. Additionally, for space platforms, the natural frequencies are often tightly packed and have very little damping. The robust control techniques researched demonstrate an innovative way to design controllers for these lightweight segmented space telescopes.

## **B. ADAPTIVE OPTICS SYSTEMS**

The term adaptive optics refers to any optical system in which some optical component; be it a mirror, lens, or some other device, undergoes adaptation or modification to improve the resulting wavefront. The preceding discussion on controlling the shape of the primary optic on space telescopes fits the general description of an adaptive optics (AO) system. To be clear on the nomenclature, the *adaptive optic* is that component of the system such as the mirror, which is altered; whereas *adaptive optics* usually refers to the entire system.

The optical wavefront is a perpendicular cross section or slice of a propagating beam of photons, which is measured by a wavefront sensing device such as a camera. For example, a beam of coherent light from a laser propagates along a cylindrical path. At that point, taking a sensor measurement at any location or at any instant of time yields a representation of the wavefront. Ideally, the wavefront from a high-quality laser would be planar, or flat. In reality, aberrations cause the wavefront to be non-planar and wavy.

Aberrations in optical systems come from a variety of sources. Light traveling through the vacuum of space would be the most un-aberrated light possible. As the light propagates through a dynamic atmosphere, or any other medium, it becomes aberrated to an observer on the other side of that medium. Other aberrations arise from imperfections in optical components. Even the human eye is not immune to aberrations, hence the need for corrective lenses or eye surgery. For machined optics, the imperfections result from uneven coatings, imperfect shapes, or impurities in glass among others. Light passing

through even one optical component has become aberrated beyond its original form. A moving or vibrating platform can also lead to wavefront aberrations, which is of particular concern for spacecraft.

AO systems come in a variety of styles and designs, but there are usually three components common to all. Those components are a wavefront sensor, an adaptive optical component, and a control computer. This is not unlike a standard control system that consists of a sensor, control algorithm, and actuators influencing a plant. Each of these portions will be discussed subsequently. A generalized schematic is shown in Figure 3. This research focuses exclusively on the design of new and innovative control algorithms. The optical components and wavefront sensors used on the experimental testbed are commercially available, off-the-shelf pieces of hardware. Although the emphasis here is on controls, adaptive optics is truly a multi-disciplinary field and draws on expertise in physics, structures, controls engineering, and electrical engineering to name a few.

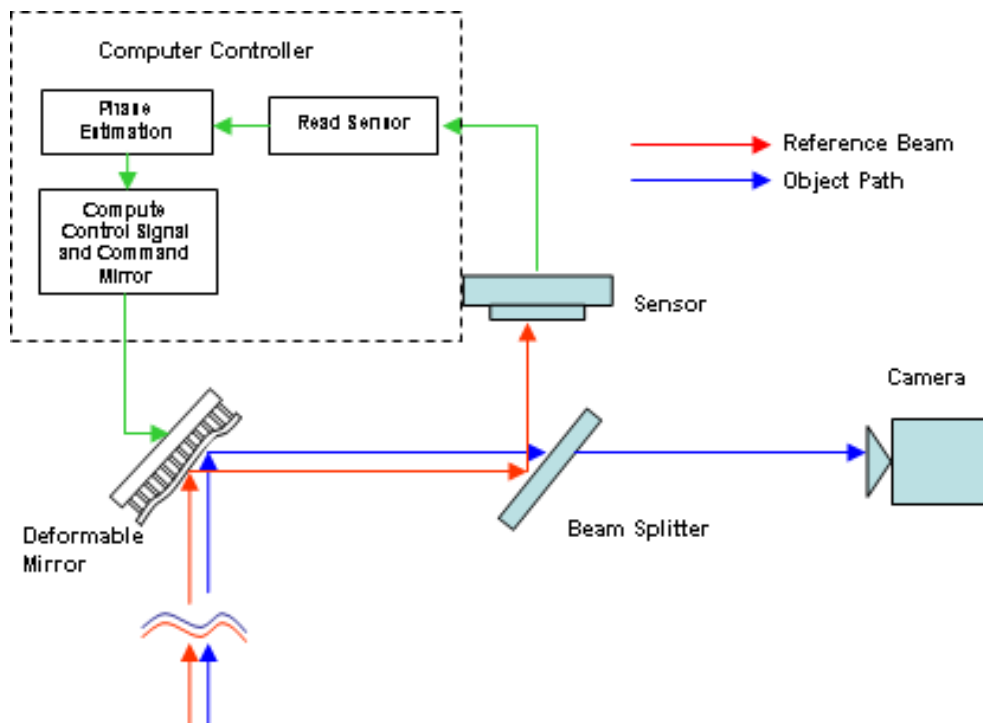


Figure 3 Generalized AO System From [3].

## 1. Wavefront Sensors

A wavefront sensor takes an optical measurement of some object of interest and represents that information as a set of discrete data points. One of the most common wavefront sensors for AO systems is the Shack-Hartmann wavefront sensor. It consists of two basic parts, a camera, and a lenslet array. The camera operates like any CCD or CMOS camera. Incident light excites pixels in an array and the light intensity is converted to voltages, which is output along with the location of pixels that were excited. The other main element of the Shack-Hartmann wavefront sensor is the lenslet array at the front entrance pupil of the camera. To understand its purpose, first envision a card that is placed at the entrance pupil, blocking all light from reaching the camera sensor. Now poke a series of holes in the card in a geometric pattern, such as a square matrix. Light from the incident wavefront will pass through these holes, undergo diffraction, and strike the CCD sensor. Now replace the holes with an equal number of small lenses (known as lenslets) which abut up against each other such that there is no remaining surface of the card. The entire blockage now consists of a grid of lenslets.

Each of these lenslets is identical and will focus the incoming light on the CCD behind it. The distance from the lenslet array to the CCD is the focal length of the lenslets. For a planar incoming wavefront, the location of the focused spots on the CCD will be evenly spaced in the same geometric pattern as the lenslet array.

If, however, the incoming wavefront is not planar, then the resulting spots on the CCD will not be evenly spaced. Whereas a planar wavefront will come to focus directly behind each lenslet, an aberrated wavefront will cause the spot to come to focus at some  $x$  and  $y$  displacement on the CCD. Figure 4 shows an example of an  $x$  displacement from an aberrated wavefront; a  $y$  displacement would be normal to the surface of the page.



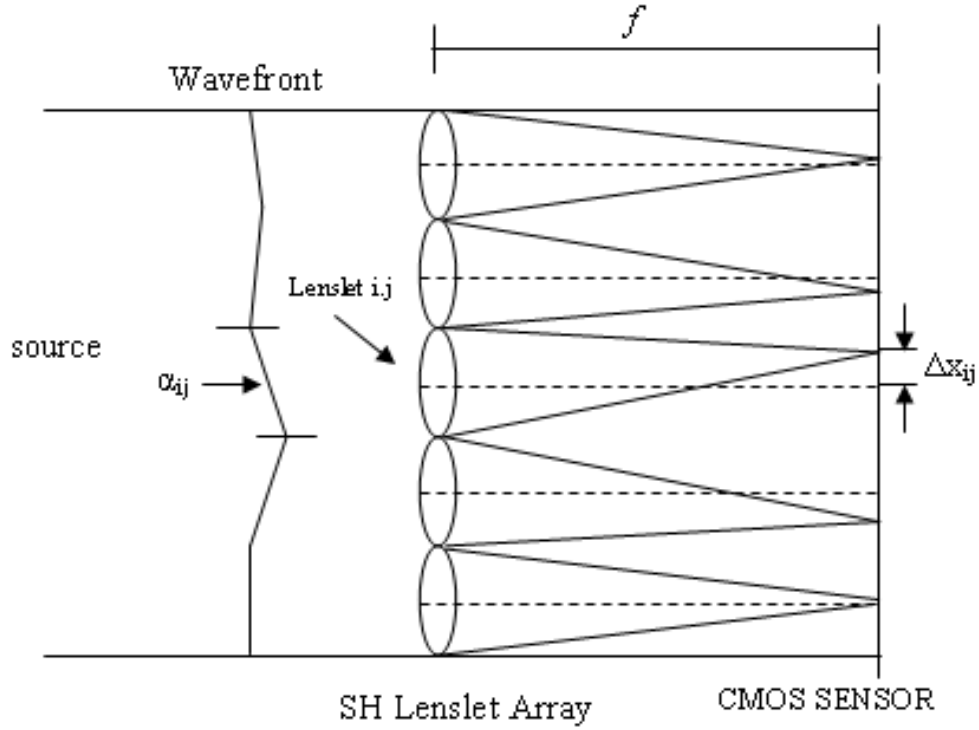


Figure 4 Lenslet Array Spot Formation From [3].

By measuring the actual location of the spots vs. the expected location for a planar wavefront, an estimate of the true shape of the incoming wavefront can be obtained. This information is then used by the control computer to determine what action must be taken to correct the aberration.

The Shack-Hartmann is only one example of a wavefront sensor for an AO system. A phase diversity sensor is another common wavefront sensor that attempts to determine wavefront shape based on the difference in image intensity from typically two cameras placed at different locations in the beam path [4]. Both the analytical model and experimental testbed described in this research use Shack-Hartmann wavefront sensors.

## 2. Adaptive Optical Components

Once the actual shape of the wavefront has been determined, the control algorithms are needed to determine how best to make the wavefront as planar as possible. First, however, it is best to understand the actual methods available to apply a correction

to the wavefront. This is accomplished through use of an adaptive optic. Perhaps the simplest type of adaptive optic to start with would be a Fast Steering Mirror (FSM). The reflecting surface of an FSM is a normal flat mirror. The difference is in the mounting mechanism that supports the mirror in the system. Imagine a pair of orthogonal axes along the surface of the mirror. These axes are commonly referred to as tip and tilt axes. By making small rotations about these axes, the beam of light the mirror is reflecting can be steered. This ability to alter the orientation of the mirror, and therefore the beam path, allows an FSM to be classified as an adaptive optic and an optical system containing an FSM is likewise classified an AO system. An FSM, however, corrects only first order wave aberrations.

One common source of such aberrations in an optical beam is jitter caused by structural vibrations. Since these vibrations are somewhat oscillatory in nature, if the wavefront sensor is fast enough to identify their frequency, an FSM should be able to apply an appropriate phase difference to null out the jitter aberrations in the optical beam. In this example, the system's actuators affect a change in the FSM's tip/tilt orientation.

For higher order wave aberrations, a more complex adaptive optic such as a deformable mirror is used. Unlike the FSM, which has a continuous, flat, face sheet surface, the surface of a deformable mirror can be adjusted to take on other desired shapes that are *not* flat. This is accomplished with a set of actuators on the back surface of the mirror. Piezoelectric actuators are one type and can be bonded to the back surface such that the actuator can be lengthened or shortened to "push" and "pull" the surface of the mirror into the desired shape. Another type consists of electrostatic actuators where a voltage potential creates a deformation of the mirror surface instead of the motion of a physically attached rod.

The purpose behind deformable mirrors is to create a mirror shape that exactly matches the inverse of the measured wavefront. Therefore, if the wavefront is determined to have a particular shape, then by inverting that shape and applying it to the mirror, the wavefront can be made planar. The success of this approach will depend on several factors including having enough lenslets in the wavefront sensor to accurately characterize the wavefront, a control algorithm capable of quickly determining a solution

before the wavefront changes, and enough actuators to create the inverse wavefront with high enough fidelity. Technology has increased to the point where a large number of lenslets and actuators can be packed into a relatively small space on their respective components. This is advantageous in that it allows higher fidelity shapes to be measured and created. The disadvantage lies in the next topic of discussion, the control laws governing the process.

These two brief descriptions of adaptive optical components only scratch the surface of the level of complexity that can exist in AO systems. Remember that for high altitude space based telescopes, the optics will most likely need to be segmented to provide the degree of resolution required. A telescope comprised of even just two segments presents a significant challenge for the design engineer. Future telescopes will be comprised of several individual segments requiring precise alignment, where each segment is its own deformable mirror requiring face sheet control. The analytical model studied in this research is just such a system.

### **3. Control Algorithms**

Adding lenslets and actuators to an AO system not only increases complexity but also lends itself to coupling between actuators. Whereas historically, control laws treated AO systems as a static problem, and to date, adaptive optics has been a field of study largely belonging to the field of astronomy where AO systems are used to correct for ground based observatories peering at distant starlight through a turbulent atmosphere. Using either a naturally occurring or artificially created guide star, the control computer can determine the atmospheric aberration in the guide star's wavefront and use that information to compensate for the atmosphere with the optics. This can be done in either a real-time or in a post-processing manner. For real-time correction, the computer has to compute and apply the corrections before the atmosphere above the telescope changes. This process is made much simpler by the telescope mirrors being large rigid structures where the control bandwidths are well below the natural frequencies, so the structural dynamics can be ignored in the control design. For lightweight space based telescopes, besides having to contend with natural frequency concerns, there is increased probability

that a large piston motion by a particular actuator will have an unintended effect on the mirror surface in the neighboring actuator's space. This effect is magnified in light of the fact that on current deformable mirrors, large numbers of actuators are packed into relatively small areas. If simply ignored, this coupling will have an adverse effect on system performance. The structural flexibility also cannot be ignored in the control design.

Since the design of robust control algorithms for AO systems is the purpose of this research, this brief introduction for AO control algorithms will be sufficient for now. For a more thorough treatment of AO systems, the reader is referenced to [5], considered a primary resource in the field. Specifics of the exact challenges faced and the solutions to those challenges will be addressed throughout the remainder of this dissertation.

## **C. OBJECTIVES**

### **1. Analytical**

The analytical research has the following objectives:

1. Apply robust control techniques for fine surface control of a complex flexible space mirror to minimize wavefront aberrations.
2. Develop improved model reduction techniques with the emphasis of minimizing wavefront aberration.
3. Achieve the desirable control bandwidth.

### **2. Experimental**

The experimental research has the following objectives:

1. Apply robust control to an adaptive optics testbed.
2. Compare the performance of robust control and currently used classical control techniques.

#### D. CURRENT STATE OF RESEARCH IN THE FIELD

Although the majority of AO system controllers have been of a classical nature, there has been some initial research into advanced robust control techniques for AO systems. To date, the author is not aware of any operational systems that employ a robust controller based on  $H_\infty$  techniques. The work of Frazier et al. has looked at incorporating some of these techniques onto testbed systems [6], [7], [8], [9]. Their work has been done on simple testbed setups quite similar to the Spacecraft Research and Design Center adaptive optics testbed at the Naval Postgraduate School used in this research. The adaptive optic in their research was also a 37 channel deformable mirror.

Kun Li et al. have investigated  $H_\infty$  control techniques for segmented telescopes [10], but their approach involves using centralized, decentralized, and overlapping control architectures to handle the complexity of large numbers of states, inputs, and outputs. The technique presented here will instead focus on model reduction techniques to synthesize the  $H_\infty$  controller. Other works have begun to apply  $H_\infty$  techniques to large ground based telescopes that have more flexibility than previous generation telescopes, similar to what space based telescopes will experience [11], [12], [13].

The general theory of  $H_\infty$  control techniques is much more developed than the application to AO systems. Several papers and textbooks have been written that have advanced these techniques on benchmark problems [14], [15], [16], [17]. These works have not been specific to segmented space telescope applications, however. This research will adapt these techniques for complex space telescope models.

The most thorough work on  $H_\infty$  control techniques for lightweight segmented optics has been done by Carrier [18]. His research looked at modeling and robust control techniques for the Advanced Structure/Control Integrated Experiment (ASCIE) testbed, a segmented optical system also used by [10]. In physical appearance, the ASCIE is quite similar to the space telescope model used in this research. It contains hexagonal mirror segments for the primary optic and a lightweight truss support structure. Unlike the model used for this dissertation, however, the ASCIE is not an adaptive optics system. It

contains only 24 sensor inputs versus the 936 sensor measurements used here, and only 18 actuators versus the 997 used here. Also because of some of the computational limitations at the time, the control design was broken into subsystems. Processor capabilities have matured enough to negate the need to form separate subsystems; however, a model reduction is still required. Nonetheless, the modeling and advanced control techniques developed by Carrier form the foundation for much of the application in this dissertation.

Specifically, the work on the ASCIE demonstrated that stochastic controller design methods were impractical due to sensitivities to unmodeled dynamics, modal frequency uncertainty, and modal damping uncertainty. Worst case, or  $H_\infty$ , methods yielded a 10% stability margin to modal frequency uncertainties. Furthermore, the research developed the technique of using input and output multiplicative uncertainties for loopshaping purposes.

This research will take the foundational work from these sources and adapt it for use on a significantly more complex segmented space telescope model. Specifically, the techniques will be adapted for AO systems and the requirement to perform model reduction prior to controller synthesis. The robust controller synthesis process used will be experimentally validated on an AO testbed. A testbed for the analytical model was not available, however, so the control techniques will be demonstrated on a simpler setup and suite of equipment.

## **E. DISSERTATION OUTLINE**

Chapter II of this dissertation will give detailed descriptions of the complex space telescope model along with the AO testbed and its components. Chapter III will give an overview of robust control and the factors considered in the design of robust controllers. Chapter IV will describe the model reduction techniques necessary for the synthesis of the robust controller. Chapter V will apply the model reduction and robust controller synthesis theory to the analytical model and show the performance when subjected to an input disturbance. Chapter VI will describe the same process for the experimental results on the AO testbed. Final analysis and conclusions will be given in Chapter VII.

## **F. CONTRIBUTIONS**

The present research has contributed to the state-of-the-art in the following areas:

1. An  $H_\infty$  robust control technique has been used for surface control of a flexible space telescope model including structural dynamics.
2. Robust control techniques have been able to provide a desired control bandwidth that was not possible with classical control.
3. A new model reduction technique using Zernike polynomials and singular value decomposition has been developed. This technique has been found to provide better performance to reduce the wavefront aberration in the space telescope model.
4. A robust control technique has been applied experimentally to the adaptive optics testbed of the Naval Postgraduate School Spacecraft Research and Design Center. The robust control technique has been found to be superior to classical control in response time and disturbance rejection.

THIS PAGE INTENTIONALLY LEFT BLANK



## **II. TESTBED AND MODEL OVERVIEW**

### **A. SEGMENTED SPACE TELESCOPE MODEL**

#### **1. Model Purpose**

The analytical model researched in this dissertation is a state space model for a space telescope with a segmented primary optic. It was developed and provided by an industry partner as part of a government program to test viability and technology readiness for future space-based telescopes. The model represents an actual system built for test purposes, but not as a flight test model. It involves the latest state-of-the-art technologies for space telescope systems. The analytical research conducted in this dissertation does not involve the actual hardware, only the simulation model.

The model is restricted to the optical payload, and does not include the supporting spacecraft bus. At a basic level it is not unlike other space telescopes with a Cassegrain configuration in that it has a primary mirror that reflects the incoming light back to a secondary mirror, which in turn reflects the light back through a hole in the center of the primary mirror. A suite of science and calibration sensors is located behind the primary optic. The James Webb Space Telescope shown in Figure 2 also has this basic configuration.

Due to the nature of government contracts and funding, this program was somewhat constrained in scope. For example, the control system used standard classical control methods with notch filters. The nature of the system, however, lends itself to research into the feasibility of robust controllers. This is just one of several examples of additional research that could be accomplished on this model.

#### **2. Model Complexity**

The segmented space telescope model is extremely complex. It contains 332 states, 997 inputs, and 936 outputs. This is the main reason that model reduction is necessary before a robust controller can be synthesized. The 332 states come from 166 modes identified in a Finite Element Analysis. The inputs correspond to actuators for

mirror surface control and the outputs are sensor measurements. Most, but not all, of the sensor measurements are of the wavefront. By means of comparison, the segmented space telescope model investigated in [10], which is actually quite similar in appearance and function to the model investigated in this research, has 70 states, 18 inputs, and 18 outputs. The Giant Segmented Mirror Telescope in [12] has 200 states and 91 inputs. The AO testbed in [7] has 37 inputs and 162 outputs. The benchmark problems in [14] and [15] typically have on the order of 10 states. Therefore, as can be seen, the scope and complexity of this model is much greater than that of previous studies.

For this model, the primary mirror is comprised of six identical hexagonal segments. They are arranged in a circular pattern such that in the center is another similarly sized hexagon, only vacant, allowing the light reflected off the secondary optic to pass through to the science instruments. The positioning of the individual segments is accomplished by six coarse control actuators and three fine control actuators per segment, for a total of 54 positioning actuator inputs. Each segment also has a grid of 156 face sheet actuators, for a total of 936 shape control inputs, making each segment a deformable mirror. Besides the adaptive primary optic, this model also has another adaptive optic, a Fast Steering Mirror (FSM), located in the vicinity of the science instruments, and is used to remove global tip and tilt jitter motions. There are an additional seven inputs related to the operation of the FSM thus accounting for the 997 total model inputs.

The model outputs similarly come from several different sources. The majority come from a Shack-Hartmann wavefront sensor. Each of the six segments has 61 Shack-Hartmann lenslets associated with it. Each of these lenslets provides two output measurements, an  $x$  slope, and a  $y$  slope. This results in 732 total Shack-Hartmann outputs. Figure 5 shows a diagram of all six hexagonal segments and the individual lenslets associated with each segment. The lenslets are numbered for one of the segments, which will be important for later discussion. The other segments are numbered sequentially in a counter-clockwise wise direction and the individual lenslets in each segment are numbered similarly if each segment is rotated to the top position.

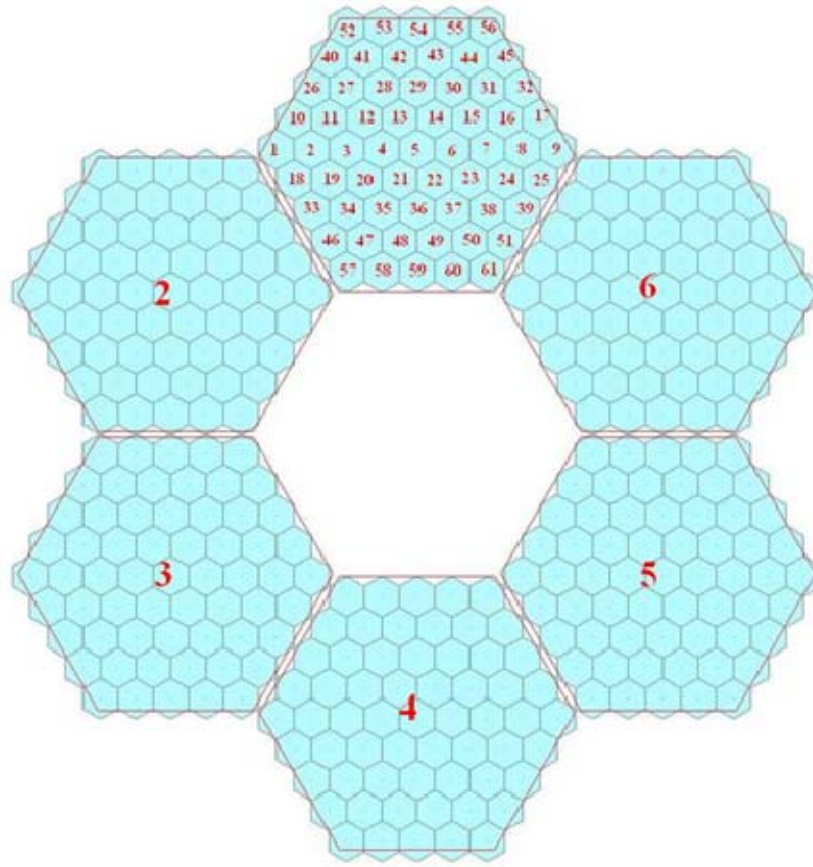


Figure 5 Mirror Segment and Lenslet Orientation.

The model also has a phase diversity wavefront sensor providing 1 piston, 1 tip, and 1 tilt measurement per segment for 18 total, and a jitter sensor providing 2 total tip/tilt measurements. The remaining sensors on the model are 18 gap sensors, three per segment, which measure the distance separating adjacent segments. In sum, there are 770 total sensor measurements. The remaining 166 outputs are the position states. Table 1 provides a summary of the model inputs and outputs.

**Inputs**

<u>Source</u>	<u>Number</u>	per segment
Face Sheet Actuators	936	156
Fine Control Actuators	18	3
Coarse Control Actuators	36	6
Fast Steering Mirror Actuators	7	
<b><u>Total</u></b>	<b><u>997</u></b>	

**Outputs**

<u>Source</u>	<u>Number</u>	per segment
Shack-Hartmann Slopes	732	122
Phase Diversity Sensor	18	3
Gap Sensor	18	3
Jitter Sensor	2	
Position States	166	
<b><u>Total</u></b>	<b><u>932</u></b>	

Table 1     Segmented Space Telescope Input/Output Summary.

**B.     ADAPTIVE OPTICS TESTBED****1.     Layout**

The Spacecraft Research and Design Center (SRDC) at the Naval Postgraduate School (NPS) has a high quality adaptive optics testbed, which was developed in conjunction with personnel from the Naval Research Laboratory (NRL) in Albuquerque, NM. The purpose of the testbed is to apply control techniques to remove aberrations from an optical wavefront. One application that demonstrates this purpose is an imagery application, where adaptive optics are used to improve the image quality of an object of interest. Figure 6 and Figure 7 show an example of the improvement in image quality that can be obtained using this technique. The four lights at the bottom are LEDs used to illuminate the object.



Figure 6      Uncorrected AO Testbed Image.



Figure 7      Corrected AO Testbed Image.

The primary components of the testbed include two deformable mirrors and two Shack-Hartmann wavefront sensors, two fast steering mirrors, a reference laser, a source object, and a science camera. The reference and object light beams are conveyed around

the table by several lenses, mirrors, and beam splitters which relay the pupil plane to the different components. A schematic of the testbed is shown in Figure 8 and a picture is shown in Figure 9.

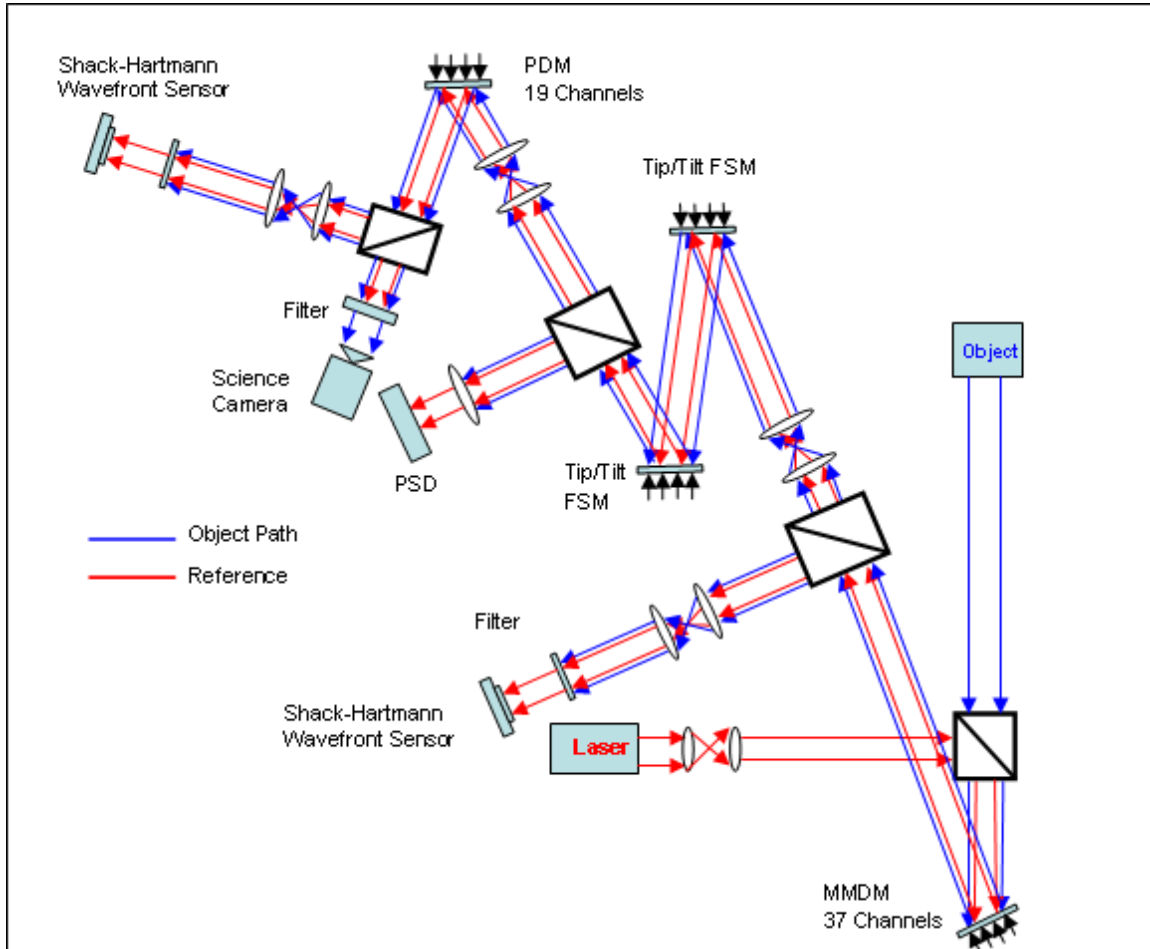


Figure 9 AO Testbed Picture.

Light from the reference laser beam and the object light are combined at the first beam splitter. This combined light is then reflected off a Micromachined Deformable Mirror (MMDM). A Shack-Hartmann wavefront sensor measures a portion of the reflected reference light source and the rest continues through the system. The Shack-Hartmann wavefront sensor sends its CMOS camera image to the control computer, which converts the CMOS image into a set of wavefront slopes. A control algorithm is used to determine the correction necessary to make the wavefront planar, and a set of

voltages is sent to the deformable mirror to implement the correction. This is the first closed loop control system on the testbed.

A filter in front of the Shack-Hartmann wavefront sensor removes the white object light prior to hitting the lenslet array. Therefore, any wavefront aberrations are measured on the reference beam, not the object light. There are two important assumptions of this setup. The first is that the same aberrations are present in the reference beam as the image beam. Second, correcting the reference beam will also correct the object light. It is possible that since the laser light is monochromatic while the object light contains all visible wavelengths, some of the optical elements on the table could cause chromatic aberrations in the object light that are not present in the laser beam. These differences are assumed to be negligible.

After the first closed loop wavefront correction process, the combined light beam next encounters two Fast Steering Mirrors (FSMs). Including just one FSM allows tip/tilt jitter aberrations to be removed. The presence of two FSMs allows the injection of a disturbance with the first FSM to simulate an on-board jitter, and the removal of the jitter with the second FSM. Of course, in their nominal configuration, when no commands are sent to the actuators on the FSMs, they behave as ordinary planar mirrors. The Position Sensing Detector (PSD) in the schematic is the wavefront sensor used to close the control loop with the second FSM.

The combined light beam next encounters a second deformable mirror, this one having piezoelectric actuators (PDM). Like the first DM, the light reflected off it is imaged by a Shack-Hartmann wavefront sensor and analyzed by a second control computer to determine the proper correction to be applied by the DM. This completes the final closed loop system on the testbed. Finally, the reference laser beam is filtered out and a science camera is able to take an image of the object light as seen in Figure 7.

## **2. Hardware**

This section will give specifics on some of the AO testbed hardware. The control laws developed involve only the components in the first closed loop system; the MMDM and one Shack-Hartmann wavefront sensor. The other components did not have an active role in verifying the performance of the control laws.

**a. Laser**

The laser on the testbed is a red HeNe laser with a wavelength of 632.8 nm. It is manufactured by JDS Uniphase and the model number is 1137P.

**b. Micromachined Deformable Mirror**

The MMDM is manufactured by OKO Technologies of Delft, the Netherlands. The following information is taken from the user manual [19]. The aperture is 15 mm in diameter. Thirty-seven actuators are located under a 12 mm diameter of the membrane with 1.8 mm center-to-center spacing between actuators. A diagram is shown in Figure 10. The mirror itself is a silicon chip coated with a silicon nitride membrane. The numbering and two-dimensional positioning of the actuators is shown in Figure 11.

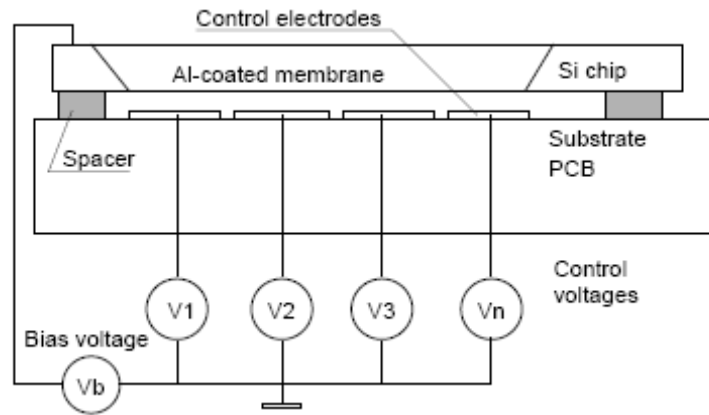


Figure 10 MMDM Schematic Section From [19].



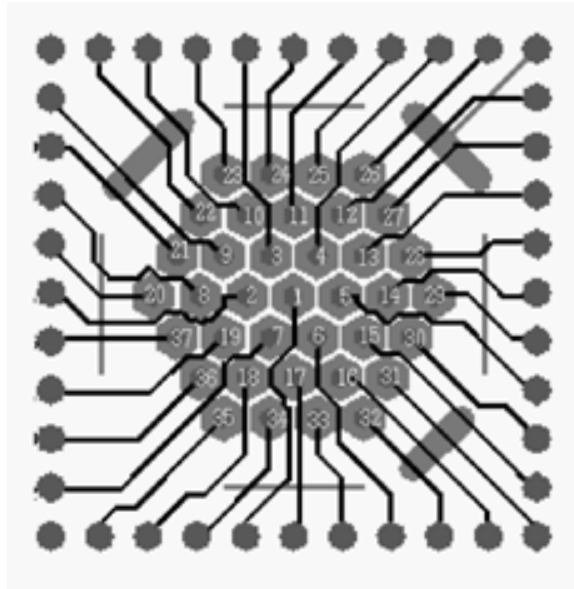


Figure 11 MMDM Actuator Locations and Positioning From [19].

***c. Shack-Hartmann Wavefront Sensor***

OKO Technologies [19] also provides the Shack-Hartmann wavefront sensor on the testbed. It is a ½-inch CMOS A601f camera manufactured by the German company Basler with a Hartmann lenslet mask from OKO installed. The sensor has 656 x 491 pixels and a frame rate of 30 frames per second. The lenslet mask has 127 lenslets laid out in a hexagonal array and coated with a fused silica coating. The aperture size is 3.5 mm and the subaperture of each lenslet is 100  $\mu\text{m}$ . The appearance of the array is similar to that of one of the segments in the segmented space telescope model array shown in Figure 5, only with 127 lenslets vs. 61.

***d. Control Computer***

The control algorithms are implemented on a standard desktop PC and Matlab software. The computer is a Pentium D with a 2.8 GHz processor and 1.0 GB of RAM. The operating system is Windows XP version 2002, service pack 2. The Matlab version is R2007a. The Basler camera is connected via fire wire to the computer, and two PCI cards connect the computer to the MMDM. One card controls 19 actuators, the other, 18.

THIS PAGE INTENTIONALLY LEFT BLANK

### III. ROBUST CONTROL

#### A. TRADITIONAL CONTROL APPROACH

The purpose of any control system is to provide stability and achieve certain performance objectives. For adaptive optics systems, classical control techniques have always been adequate. Their simpler design process and more intuitive nature make them the controller of choice for most applications. The following will give a brief overview of the traditional AO system control approach and identify the shortcomings that led to this research into more advanced control techniques.

Traditionally, the adaptive optic in large ground based AO systems is treated as a static system with no dynamics. In the case of a deformable mirror, it is assumed that the coupling between actuators is static. Classical control approaches neglect the dynamics associated with this coupling thereby simplifying the control process [3], [5]. Obviously, as the optics for space telescopes become lighter as discussed in Chapter I, and as more actuators are packed into a given area to provide higher spatial correction, this simplifying assumption becomes less realistic. For systems with a high degree of internal dynamics, instability can result from a controller designed from a static model.

At the basis of the control algorithm, the reconstruction, or influence matrix, relates the actuators with the aberrations in the wavefront. The reconstruction matrix is formed by starting with the mirror in a neutral position and then actuating or poking each actuator in turn while measuring the effect on the wavefront. For this reason, the reconstruction matrix is often referred to as the poke matrix. As an example, consider a deformable mirror with 10 actuators and a Shack-Hartmann wavefront sensor with 20 lenslets. Assume the neutral position of each actuator is represented by a 0, and it can be commanded to any value from -1 to +1. Actuator 1 is given full positive stroke and an image is taken with the Shack-Hartmann wavefront sensor. This measurement yields a vector of 40 measurements (20  $x$  and 20  $y$ .) Actuator 1 is reset to 0, and the process is repeated for actuator 2. The end result is a reconstruction matrix with dimensions of  $[40 \times 10]$  where each column represents the  $x$  and  $y$  pixel displacements on the camera sensor

for each individual actuator. These  $x$  and  $y$  pixel displacements can be easily converted to  $x$  and  $y$  slopes by multiplying by the physical pixel width and dividing by the camera focal length.

This process creates a map of how an actuator position or command affects the wavefront, but it neglects the structural dynamics of the mirror. The mathematical expression of the reconstruction matrix,  $R$ , is given as

$$R = \begin{pmatrix} S_1^{x1} & \dots & S_1^{xm} \\ \vdots & & \vdots \\ S_n^{x1} & \dots & S_n^{xm} \\ S_1^{y1} & \dots & S_1^{ym} \\ \vdots & & \vdots \\ S_n^{y1} & \dots & S_n^{ym} \end{pmatrix} \quad (3.1)$$

where  $S$  is the slope in the  $x$  or  $y$  direction,  $n$  is the number of lenslets, and  $m$  is the number of actuators. The relationship between the actuator input vector,  $\underline{u}$ , and the slope measurement vector,  $\underline{S}$ , is given by

$$\underline{S} = R\underline{u} \quad (3.2)$$

Since the slope is the measured quantity, the pseudo-inverse of the reconstruction matrix is used to determine the control inputs. One possible control approach is to subtract the product of the inverted reconstruction matrix (found with a pseudo-inverse technique) and measured slope from the previous control input as shown in Equation (3.3). This will drive the control signal to a steady state value and the wavefront slope to zero, resulting in a planar wavefront.

$$\underline{u}_{new} = \underline{u}_{old} - R^\dagger \underline{S} \quad (3.3)$$

Variations on how the wavefront is determined from the slopes (e.g., modal or zonal) and variations on the feedback method (e.g., direct, indirect, iterative, etc.) can be employed to improve the performance for this traditional control law [3].

As stated before, the classical control approach ignores the structural dynamics of a system. Even if a more complex multi-input, multi-output control approach was used that accounted for dynamics and coupling between actuators, it would still need to

perform satisfactorily in the presence of external disturbances and unmodeled dynamics. These uncertainties give credence to the idea of designing robust controllers for AO systems.

## B. JUSTIFICATION FOR ROBUST CONTROL

Robust control addresses the problem of designing a control system that yields a desired performance in the presence of model uncertainties and external disturbances. For the purposes of this research, the plant to be controlled is a state space model of the following form

$$G = \begin{cases} \dot{x} = Ax + Bu \\ y = Cx + Du \end{cases} \quad (3.4)$$

where  $x$  is the state,  $y$  is the measured output, and  $u$  is the control input. The robust control synthesis process augments the plant,  $G$ , into a modified system,  $P$ , with two input vectors and two output vectors. The process of constructing the modified plant,  $P$ , will be described later. The robust controller,  $K$ , is then designed for this augmented plant shown in Figure 12

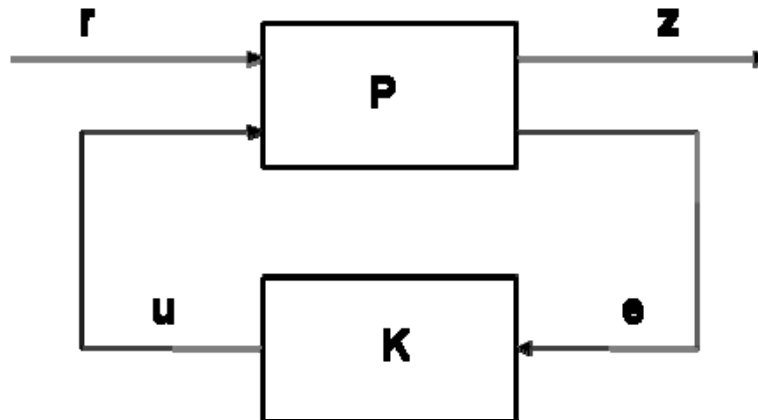


Figure 12 Standard Robust Control System.

where the plant,  $P$ , and controller,  $K$ , are both state space models,  $r$  is the external input (which contains a reference input, external disturbances, and noise),  $z$  is the performance measure,  $u$  is the control input, and  $e$  is the error between the reference input and measured output. For the specific case of the segmented space telescope model used for

this research, the state space plant model describes both the actuators and the Shack-Hartmann wavefront sensor outputs. The external inputs,  $r$ , are all zero. The reference input is usually zero for adaptive optics applications since a planar wavefront is desired; however, in some situations a non-zero reference input may be used if a particular aberration mode is desired. Since the error signal,  $e$ , is the difference between the measured output,  $y$ , and the reference,  $r$ , and the reference is zero, the error becomes simply the negative of the measured output. The control input,  $u$ , is a vector of actuator voltages. For this research the performance measure,  $z$ , is comprised of two components, the first is the error signal,  $e$ , and the second is the measured output,  $y$ . These two performance measures will be penalized or weighted differently for the controller synthesis process. This weighting process will be discussed shortly. The end goal then of the robust controller synthesis process is to minimize the  $\infty$ -norm of the operators from  $r \rightarrow z$ .

The overall goal of a robust controller is to provide stability for a system in the presence of uncertainty or unmodeled dynamics as discussed in Chapter I. Ideally, a robust controller will be able to handle these uncertainties better than other controllers such as classical PID controllers or optimal linear quadratic regulators. When speaking of robustness, there are two different performance criteria implied: the ability to handle uncertainty in the model, and the ability to reject disturbances and noise. What separates the robust control design process from a traditional control design process is that these uncertainties are explicitly accounted for in the design process to improve performance in the face of uncertainties that are poorly understood or modeled. The  $H_\infty$  robust control method minimizes the upper bound of the performance signal.

What follows are some of the mathematical foundations that form the backbone of robust control theory. Much of the material is general in nature and not specific to the research performed on the analytical segmented space telescope model. The topics include system norms, sensitivity and complimentary sensitivity functions, uncertainty modeling, and some of the tools necessary for the formulation of the appropriate augmented system matrix,  $P$ , to which the controller is synthesized. The application of these techniques to the analytical model will be covered in Chapter V.

## C. MATHEMATICAL FOUNDATIONS

### 1. Norms

The basic premise of robust control involves minimizing a system norm. The type of norm is dependent on the type of robust controller being designed. A general overview of norms follows. From a conceptual point of view, a norm is nothing more than a measure of how large something is, such as the size of a vector. The general form of a vector norm in  $\mathbb{R}^p$  as shown in [16] is given as

$$\|x\|_p := \left( \sum_{i=1}^N |x_i|^p \right)^{1/p}, \quad 1 \leq p < \infty \quad (3.5)$$

where  $p$  takes on the value of the desired norm. The 1-norm and 2-norm (also known as the Euclidean norm) are common norms. In the case of robust control, a common norm, and the one used in this research, is the infinity-norm, given as

$$\|x\|_\infty := \max_{1 \leq i \leq n} |x_i| \quad (3.6)$$

The standard designation for this type of controller is  $H_\infty$ , where the  $H$  refers to the Hardy space for stable systems.

For matrix operations, the induced norm becomes more useful, where the norm can alternately be thought of as a gain. Given the following simple transformation where  $A$  is the gain or amplification of the system

$$y = Ax \quad (3.7)$$

the induced matrix norm is given as

$$\|A\|_p = \max_{x \neq 0} \frac{\|Ax\|_p}{\|x\|_p} \quad (3.8)$$

### 2. Singular Values

Singular values are used extensively for robust control synthesis. Using a standard definition for linear algebra, singular values are the square root of the eigenvalues of a matrix times its adjoint (i.e., complex conjugate transpose) as shown by

$$\sigma_i = \sqrt{\lambda_i(A^*A)} \quad (3.9)$$

It can be shown that the largest gain for any input direction is equal to the maximum singular value,  $\bar{\sigma}$ , and that the smallest gain for any input is equal to the minimum singular value,  $\underline{\sigma}$ . The  $H_\infty$  norm can also be defined as the least upper bound on the maximum singular value. The  $H_\infty$  norm for a linear time invariant system,  $G$ , is given as

$$\|G\|_\infty = \sup_{\omega} \bar{\sigma}(G(j\omega)) \quad (3.10)$$

For multi-input, multi-output systems, a plot of the maximum singular values is analogous to the Bode magnitude plot for single-input, single-output systems.

### 3. Small Gain Theorem

One of the most fundamental concepts for robust control is the small gain theorem, which follows from the above discussion of norms. For stability analysis, the small gain theorem replaces the traditional concepts of gain and phase margin. Consider the system in Figure 12 with uncertain elements  $\Delta$  added as shown in Figure 13.

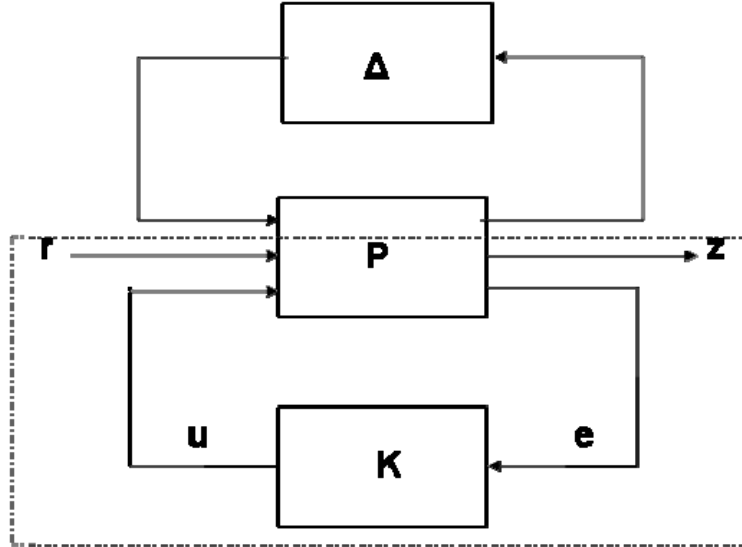


Figure 13 System with Uncertainty.



Let the region inside the dashed line, which is identical to the system in Figure 12, be represented as  $M$ . The small gain theorem requires that the gain (norm) of the uncertainty,  $\Delta$ , multiplied by the gain of the system,  $M$ , must be less than 1 for the system to be robustly stable as shown by

$$\|\Delta\| * \|M\| < 1 \quad \forall \Delta \quad (3.11)$$

where the  $*$  represents a multiplication.

Another common form of the small gain theorem is given as

$$\|\Delta\|_{\infty} \leq 1/\gamma \quad \text{iff} \quad \|M\|_{\infty} < \gamma \quad (3.12)$$

where  $\gamma$  is a bound and  $\gamma > 0$ .

#### 4. Sensitivity Functions

Two other necessary concepts for robust control design are the sensitivity function and the complementary sensitivity function. These functions allow the designer to shape the frequency response of the system in a manner similar to classical loopshaping techniques. The sensitivity function is important for shaping the response of lower frequencies, while the complementary sensitivity function helps shape the high frequency response [20]. Mathematically, for a system consisting of a plant,  $G$ , and a controller,  $K$ , with negative feedback, the sensitivity function,  $S$ , has the following form

$$S = (I + GK)^{-1} \quad (3.13)$$

From this, it follows that the complementary sensitivity function,  $T$ , has the following form

$$T = GK(I + GK)^{-1} \quad (3.14)$$

Due to their complementary nature, the following is true

$$S + T = 1 \quad (3.15)$$

A control design process that incorporates loopshaping with both the sensitivity and complementary sensitivity functions is often referred to as a mixed-sensitivity problem [20]. In this instance, the sensitivity function influences the performance of the controller, and the complementary sensitivity function influences the stability of the system at higher frequencies. Figure 14 gives a representation of how loopshaping of the

sensitivity and complementary sensitivity functions can affect the controller / plant system, represented by  $L$  ( $L = GK$ ) in the figure.

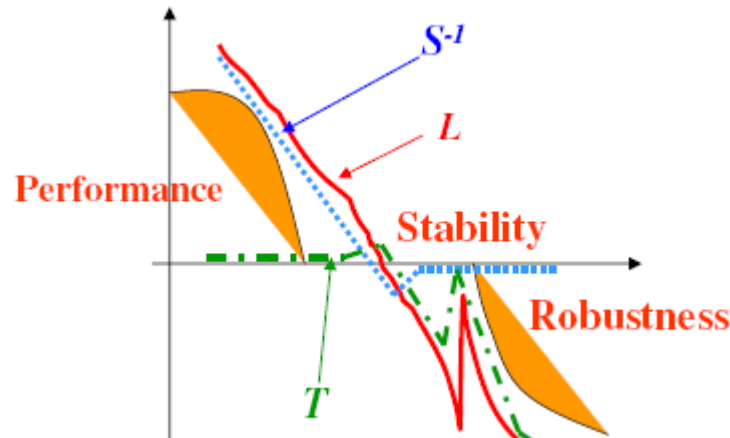


Figure 14 Robust Control Loopshaping From [20].

At low frequencies, the loop transfer function,  $L$ , is weighted to follow the inverse of the sensitivity function. The sensitivity function of the system describes how well the controller does at providing for disturbance rejection, tracking errors, and negating any plant parametric variations. Shaping the sensitivity function indirectly shapes the loop transfer function, and in some cases vice versa. At higher frequencies, the shape of the complementary sensitivity function describes the transient response and stability. The complementary sensitivity function is shaped by weighting functions in the same way as the sensitivity function.

## 5. Weighting Functions

At this point, it is necessary to introduce a set of weighting functions that will manipulate or shape the sensitivity and complementary sensitivity functions. The weighting functions can take whatever form is appropriate for the system, but for the purpose of this research, first order transfer functions are satisfactory. The first weighting function, introduced as  $W_1$ , is a penalty on the error and affects the lower frequencies and shape of the sensitivity function. A second weighting function,  $W_2$ , is a penalty on the control signal but is not used in this research. The final weighting function,  $W_3$ , is a penalty on the measured output and affects the complementary

sensitivity function and higher frequencies. Figure 15 shows a schematic of a nominal system with a plant, a controller, and weights  $W_1$  and  $W_3$ . Note that the transfer functions shown in the figure merely represents a generic transfer function and not the actual weights used.

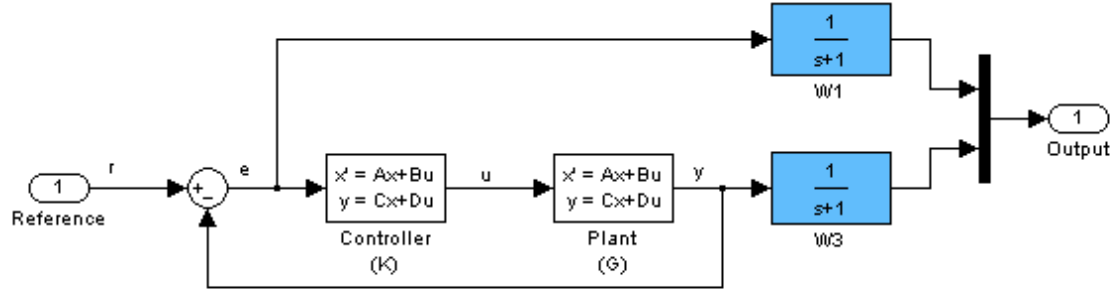


Figure 15 Schematic of System with Weighting Functions.

The weighted error and measured output signals together form the performance measure previously identified in Figure 12 as  $z$ . The error that is weighted by  $W_1$  is minimized in order to achieve the desired performance by influencing the sensitivity function. The output that is weighted by  $W_3$  is minimized in order to achieve stability in the presence of higher frequency disturbances by influencing the complementary sensitivity function. Satisfying both of these goals simultaneously may not be possible; thus an iterative approach to synthesizing the robust controller is used. If the weights selected are too restrictive on the design, a robust controller meeting the design requirements cannot be synthesized.

The closed loop system with weight  $W_1$  is said to have robust performance if the following condition of the small gain theorem is met

$$|W_1| < |1 + GK| \quad \forall \omega \quad (3.16)$$

Similarly, when considering  $W_3$  and the complementary sensitivity function, the system is robustly stable if the following condition is true

$$|W_3 GK| < |1 + GK| \quad \forall \omega \quad (3.17)$$

Combing equations (3.16) and (3.17), the system has both robust performance and stability if the following is true

$$\|W_1S\| + \|W_3T\|_{\infty} < 1 \quad (3.18)$$

Designs that employ a weight on both the sensitivity function and the complementary sensitivity function are referred to as weighted mixed sensitivity problems [20].

#### D. MODEL UNCERTAINTY

The main advantage of designing a robust controller over other simpler classical techniques is the ability to handle model uncertainties. While certain designs allow for wide latitude in handling uncertainties, it would be nearly impossible to design one controller for all possible uncertainties a system might encounter over its lifetime. Therefore, it is necessary to understand what kinds of uncertainty are likely, where they come from, and how to bound the uncertainties to simplify some of the design constraints. Uncertainty can be added to a system in two different ways, an additive fashion or a multiplicative fashion. The following two figures depict these two methods. Perturbations of these types can be added to any combination of inputs or outputs to the system.

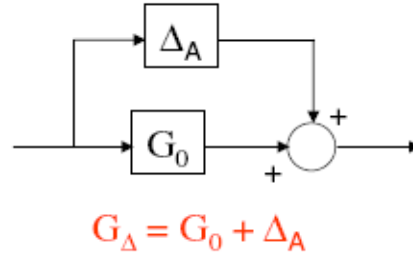


Figure 16 Additive Uncertainty From [20].

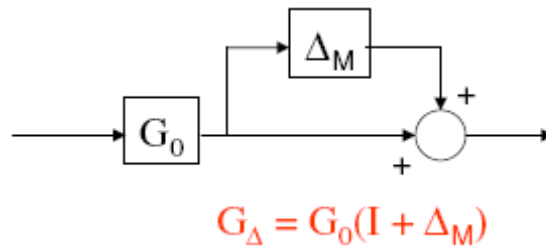


Figure 17 Multiplicative Uncertainty From [20].

The first consideration in defining the uncertainty to be added to a model is to define it as structured or unstructured. An unstructured uncertainty is a bounded perturbation that is included or added to the model, but where very little of the nature of the perturbation is known. For example, there is no transfer function that describes the general behavior of an unstructured uncertainty.

Structured uncertainties involve perturbations that are more understood than unstructured. In general, there are more constraints on the nature of a structured uncertainty than an unstructured uncertainty. Structured uncertainties can result from bounded variations in model parameters such as changes in the physical components of a system over time due to wear and tear. They also result from combinations of multiple uncertainties, or both additive and multiplicative perturbations. Figure 18 shows a diagram of typical structured and unstructured model uncertainties [17].

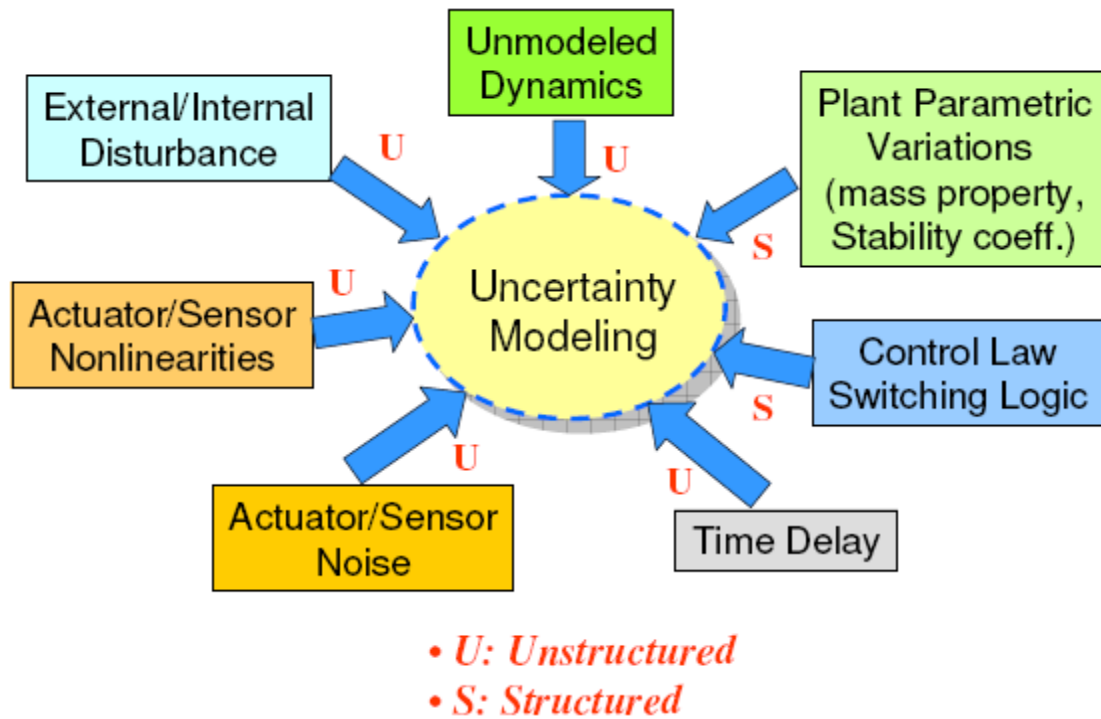


Figure 18 Structured and Unstructured Model Uncertainty Sources From [20].

In addition to helping shape the sensitivity and complementary sensitivity functions, the weighting functions also bound the system uncertainty [20]. For this reason, proper selection of the weighting functions becomes a crucial part of robust control design.

The segmented space telescope model used in this research does not contain any unstructured uncertainties. On the other hand, uncertainties on some of the physical parameters such as modal frequencies and damping are assumed. This affects the lower left quadrant where the squares of the natural frequencies are found in the following system  $A$  matrix

$$A = \begin{pmatrix} \ddots & & & & \ddots & & \\ & 0 & & & & I & \\ & & \ddots & & & & \ddots \\ \ddots & & & & \ddots & & \\ & -\omega_n^2 & & & & -2\xi\omega_n & \\ & & \ddots & & & & \ddots \end{pmatrix} \quad (3.19)$$

Uncertainty in the natural frequencies is a logical concern for a lightweight space telescope model such as this. Therefore, a percentage of uncertainty can be added to the natural frequencies to allow for explicit design of a robust controller based on an uncertain model.

## E. CONTROLLER SYNTHESIS

The robust controllers designed for this research were based on minimizing the closed loop system  $\infty$ -norm. Other robust control synthesis methods exist such as those based on a 2-norm, but they will not be discussed here. The  $\infty$ -norm method used here is a direct method denoted as  $H_\infty$ . This method designs a controller based on a nominal augmented plant as previously shown in Figure 12.

The  $H_\infty$  robust control design technique requires a properly constructed plant model to synthesize a robust controller. In order to achieve the robust performance and stability design objectives, the plant must be augmented with the appropriate weighting functions. A representation of this augmented nominal plant is shown in Figure 19.

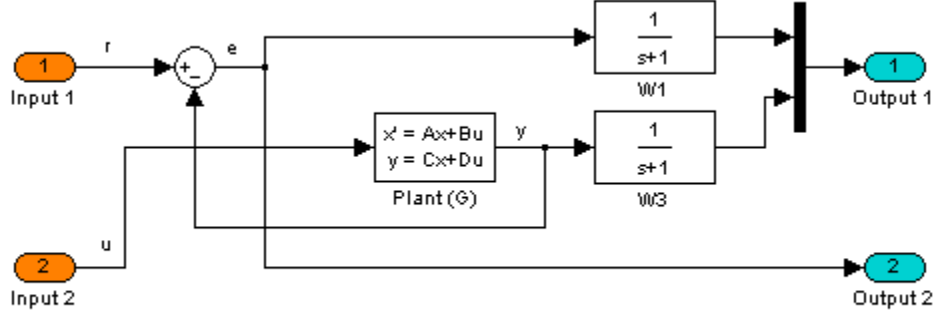


Figure 19 Augmented Nominal 2-Input, 2-Output Plant.

This augmented plant is often referred to as the 2-input, 2-output model. The two vector inputs to the augmented plant are the reference input and the control input, which the controller to be designed will provide. One of the vector outputs is the weighted error and weighted measured output signal combined, which is otherwise known as the performance measure. The other vector output is the error signal that is used as the input for the controller.

Once this 2-input, 2-output model has been constructed, the goal is to minimize the  $\infty$ -norm of the error signal to the command or disturbance input. A representation of how the weighting functions are included in the augmented model,  $P$ , is given as

$$P = \left( \begin{array}{c|c} W1 & -W1G \\ 0 & W3G \\ \hline I & -G \end{array} \right) \quad (3.20)$$

Since the original plant,  $G$ , was a state space model,  $P$  is also a state space model and can be partitioned as

$$P = \left( \begin{array}{c|cc} A & B_1 & B_2 \\ \hline C_1 & D_{11} & D_{12} \\ C_2 & D_{21} & D_{22} \end{array} \right) \quad (3.21)$$

where the  $A$ ,  $B$ ,  $C$ , and  $D$  matrices are the augmented state space matrices. The controllability and observability of the system can be determined using the submatrices

$B_1$ ,  $B_2$ , etc. As shown in [16], the following assumptions on the partitions of  $P$  are made before proceeding with the controller synthesis

- $(A, B_1)$  is controllable
- $(C_1, A)$  is observable
- $(A, B_2)$  is stabilizable
- $(C_2, A)$  is detectable
- $D_{12}^T (C_1 \ D_{12}) = (0 \ I)$
- $\begin{pmatrix} B_1 \\ D_{12} \end{pmatrix} D_{21}^T = \begin{pmatrix} 0 \\ I \end{pmatrix}$

An admissible controller exists if and only if the following conditions are met:

- $H \in (Ric)$  and  $X := Ric(H) > 0$
- $J \in (Ric)$  and  $Y := Ric(J) > 0$
- $\rho(XY) < \gamma^2$

where  $H$  and  $J$  are the following Hamiltonian matrices

$$H := \begin{pmatrix} A & \gamma^{-2} B_1 B_1^T - B_2 B_2^T \\ -C_1^T C_1 & -A^T \end{pmatrix} \quad (3.22)$$

$$J := \begin{pmatrix} A^T & \gamma^{-2} C_1^T C_1 - C_2^T C_2 \\ -B_1 B_1^T & -A \end{pmatrix} \quad (3.23)$$

$\gamma$  is a performance bound with  $\gamma > 0$ ,  $Ric$  is the solution to an algebraic Riccati equation of the form

$$A^T X + XA + XBX + C = 0 \quad (3.24)$$

and  $\rho$  is the spectral radius with

$$\rho(A) := \max_{1 \leq i \leq n} |\lambda_i| \quad (3.25)$$

The robust control design algorithm iterates on the value of  $\gamma$  between 0 and infinity with a bisection algorithm until such time as a solution to the Riccati equation



cannot be found. Once the specified tolerance threshold has been reached the iteration stops and the controller,  $K$ , can be computed from the following equations

$$K = \left( \begin{array}{c|cc} A_f & -ZL & ZB_2 \\ \hline M & 0 & I \\ -C_2 & I & 0 \end{array} \right) \quad (3.26)$$

where

$$M = -B_2^T X \quad (3.27)$$

$$L = -YC_2^T \quad (3.28)$$

$$Z = (I - \gamma^{-2} YX)^{-1} \quad (3.29)$$

$$A_f = A + \gamma^{-2} B_1 B_1^T X + B_2 M + ZLC_2 \quad (3.30)$$

Figure 20 shows the synthesized controller,  $K$ , attached to the augmented plant from Figure 19. Figure 20 is now identical to the original system presented in Figure 12.

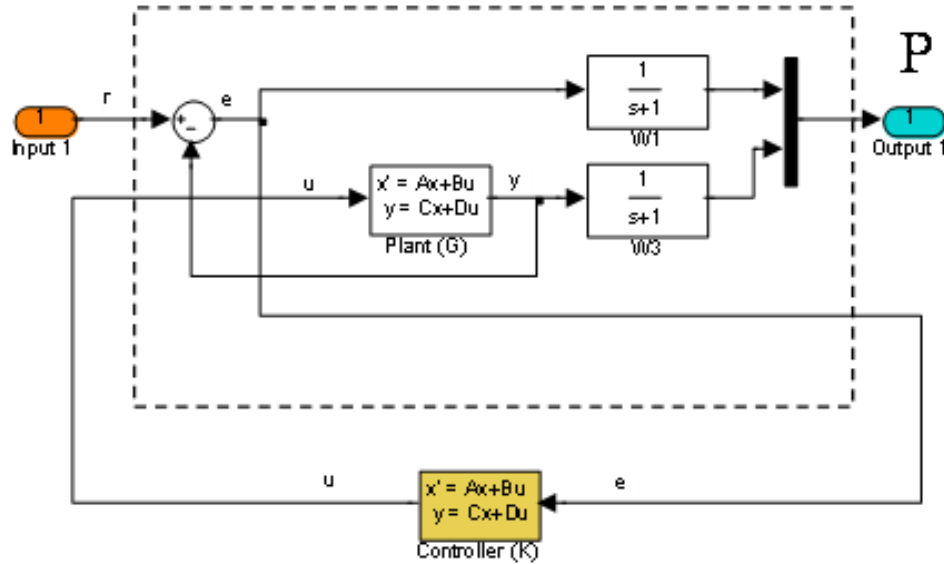


Figure 20 Augmented Plant and Controller.

The controller synthesis consists of designing the controller,  $K$ , such that the following cost function is minimized

$$\|T_{zr}\|_{\infty} < \gamma \quad (3.31)$$

where  $T$  is the closed loop transfer function. After this design process has generated the  $H_{\infty}$  controller, it can be implemented as a continuous system, or discretized prior to implementation. The application of these techniques to the segmented space telescope model will be discussed in Chapter V.

## IV. MODEL REDUCTION TECHNIQUES

### A. INPUT/OUTPUT REDUCTION

The robust controller synthesis process described in Chapter III can be rather computationally prohibitive. In the case of the analytical segmented space telescope model, the 332 states, 997 inputs, and 936 outputs are more than an average desktop computer can process. Therefore, some kind of model reduction is necessary. This chapter will present an innovative method developed to reduce the inputs and outputs as well as a standard method of state reduction.

#### 1. Singular Value Decomposition

The principle behind the reduction method developed is the projection of a vector into a subspace. In this case, a large vector of input values is projected into a vector of many fewer values. If the projection is chosen carefully, then the important or significant values of the original vector are preserved so that when the reduced vector is expanded back to the original number of values, it is still representative. The Singular Value Decomposition (SVD) is one such technique that, by its very nature, preserves the significant values.

In general, the SVD has the following form

$$SVD(H) = U\Sigma V^T \quad (4.1)$$

where  $H$ ,  $U$ ,  $\Sigma$ , and  $V$  are all matrices, and  $\Sigma$  is a diagonal matrix with the singular values arranged in decreasing size. The matrices  $U$  and  $V$  are also ordered such that the vector associated with the largest singular value is in column one and so on. A plot of all the singular values helps to identify how many singular values have a sufficient impact on the final system so that a logical place to truncate the singular value matrix can be found. For example, if there are 40 total singular values, but the last 25 are significantly smaller than the first 15, those last 25 values can be truncated and the most important aspects of the original system are still preserved. Since the column vectors of the  $U$  and  $V$  matrices are also rank ordered into decreasing importance, only the first 15 column vectors of those matrices will be retained. As will be shown in Chapter V, when  $H$  is

defined to be the transfer function of the inputs to the outputs for the analytical space telescope model, the large number of inputs or outputs of the original system can be projected into the column vectors of the truncated  $U$  and  $V$  matrices. The inputs are projected via the  $V$  matrix and the outputs are projected via the  $U$  matrix.

Once a controller has been synthesized for this reduced input/output model, the controller outputs can be projected back into the total number of original plant inputs through the truncated  $V$  matrix. Similarly, the original plant outputs are projected into the truncated  $U$  matrix so that they may be inputs for the reduced controller.

## 2. Zernike Polynomials

An innovative approach developed in this dissertation is the use of Zernike polynomials for model output reduction. Zernike polynomials are orthogonal and normal about a unit circle, making them especially applicable to optical applications where the optical components have circular apertures. Their orthogonal and normal nature as described in [21] is shown by

$$\int_0^1 R_n^m(\rho) R_{n'}^m(\rho) \rho d\rho = \frac{1}{2(n+1)} \delta_{nn'} \quad (4.2)$$

where  $R_n^m$  is the radial polynomial and  $\delta$  is the Kronecker delta. It is worth noting, however, that Zernike polynomials are but one of an infinite number of polynomial sets that are normal about a unit circle. Furthermore, variations on the Zernike polynomials exist depending on their particular application and usage. Derivations of the standard form of Zernike polynomials can be found in [22], [23]. A slightly modified form of Zernike polynomials known as the fringe Zernikes was developed at the University of Arizona and is used for this research [24]. The main difference is that the fringe Zernikes have been normalized to unity magnitude at the edge of the pupil. The expansion series of the fringe Zernike polynomials is given by

$$Z_n^m(\rho, \theta) = R_n^m(\rho) e^{im\theta} \quad (4.3)$$

where

$$R_n^m(\rho) = \sum_{s=0}^{n-m} (-1)^s \frac{(2n-m-s)!}{s!(n-s)!(n-m-s)!} \rho^{2(n-m-s)} \quad (4.4)$$

where  $Z_n^m$  and  $R_n^m$  both represent the Zernike polynomial,  $n$  and  $m$  are both integers with  $n \geq m$ ,  $n \geq 0$ , and  $\rho$  is a function of the aperture radii. The index,  $n$ , defines the order of the radial power, and  $m$  is the meridional frequency. The meridional frequency is in reference to the meridional or tangential plane of the aperture, which is a plane that contains both the optical axis and the chief ray. The chief ray is the ray that passes through the center of the aperture. Due to the alternating cosine and sine terms in the expansion, the polynomials can be defined somewhat differently based on how the index  $m$  is handled. Figure 21 shows a pictorial representation of the first 20 Zernike modes using the standard form.

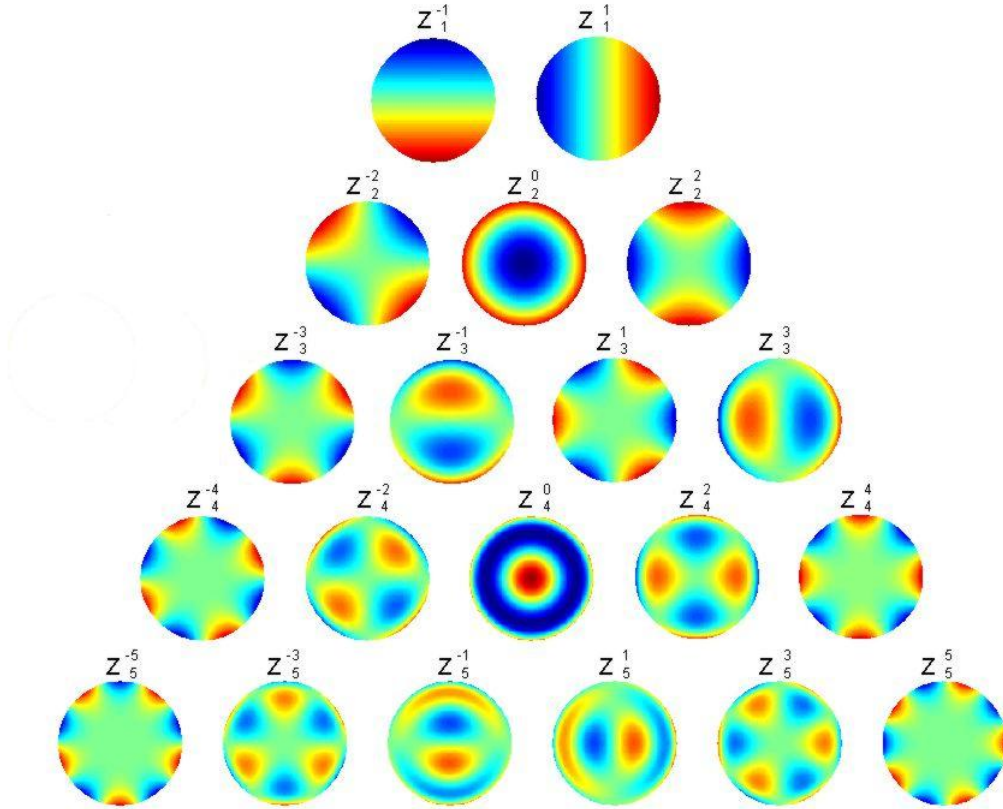


Figure 21 Twenty Common Zernike Modes From [25].

Zernike polynomials are usually derived in polar form but can be converted to the Cartesian form used in this research through the following equations:

$$x = \rho \cos(\theta) \quad (4.5)$$

$$y = \rho \sin(\theta) \quad (4.6)$$

Both the standard form and the fringe Zernikes have the same orthogonality properties. The main factor that sets the Zernike polynomials apart from other polynomial sets is a group of invariance properties that guarantee the existence of a unique polynomial for all permissible combinations of  $n$  and  $m$ . These invariance properties specify that the polynomial has the same form when the axes are rotated about the origin by a continuous function,  $F$ , with a period of  $2\pi$  and an angle of rotation of  $\phi$  [22]

$$Z(x, y) = F(\phi) Z(x', y') \quad (4.7)$$

where

$$\begin{aligned} x' &= x \cos \phi + y \sin \phi \\ y' &= -x \sin \phi + y \cos \phi \end{aligned} \quad (4.8)$$

It is important to note that as stated earlier, Zernike polynomials are normal about a continuous unit circle. The aperture for the segmented space telescope shown in Figure 5, or any Cassegrain configuration telescope for that matter, is not continuous due to the hole in the middle of the primary mirror where the light reflected from the secondary mirror passes through. In order to account for this discontinuity, a set of Zernike polynomials has been modified to be more appropriate for use on a unit ring instead of a unit circle [26]. For this research, however, the fringe Zernike polynomials were used since the primary goal was to develop a general technique. Modification to the annular polynomials as set forth in [26] is left for future work.

For lower order terms, the aberrations described by the Zernike polynomials take on other familiar names, for example, focus, coma, astigmatism, and so on. As with any series expansion, the more terms used, the more accurate the approximation will be. For this research, 21 Zernike polynomials are used to represent the wavefront. The selection of 21 Zernikes was based on an analysis of the singular values of the original system. For comparison purposes, [12] uses 8 Zernike modes for wavefront estimation and [13] uses 15 Zernikes. Additional research could be performed using different numbers of

polynomials, however, that effort was outside the scope of this research. Table 2 contains a listing of these 21 polynomials in Cartesian form. For completeness, the piston term is included, but it is a non-controllable mode in this application. For those polynomials associated with a more common name, the common name is also given.

#	Polynomial	Term
0	1	Piston
1	x	X-tilt
2	y	Y-tilt
3	$-1+2(x^2+y^2)$	Focus
4	$x^2-y^2$	Astigmatism plus defocus
5	2xy	Astigmatism plus defocus
6	$-2x+3x(x^2+y^2)$	Coma plus tilt
7	$-2y+3y(x^2+y^2)$	Coma plus tilt
8	$1-6(x^2+y^2)+6(x^2+y^2)^2$	3rd order spherical plus focus
9	$x^3-3xy^2$	5th order aberration
10	$3x^2y-y^3$	5th order aberration
11	$-3x^2+3y^2+4x^2(x^2+y^2)-4y^2(x^2+y^2)$	5th order aberration
12	$-6xy+8xy(x^2+y^2)$	5th order aberration
13	$3x-12x(x^2+y^2)+10x(x^2+y^2)^2$	5th order aberration
14	$3y-12y(x^2+y^2)+10y(x^2+y^2)^2$	5th order aberration
15	$1+12(x^2+y^2)-30(x^2+y^2)^2+20(x^2+y^2)^3$	5th order aberration
16	$x^4-6x^2y^2+y^4$	7th order aberration
17	$4x^3y-4xy^3$	7th order aberration
18	$-4x^3+12xy^2+5x^3(x^2+y^2)-15xy^2(x^2+y^2)$	7th order aberration
19	$-12x^2y+4y^3+15x^2y(x^2+y^2)-5y^3(x^2+y^2)$	7th order aberration
20	$6x^2-6y^2-20x^2(x^2+y^2)+20y^2(x^2+y^2)+15x^2(x^2+y^2)-15y^2(x^2+y^2)^2$	7th order aberration
21	$12xy-40xy(x^2+y^2)+30xy(x^2+y^2)^2$	7th order aberration

Table 2 Table of Zernike Polynomials From [24].

The innovative output reduction technique using Zernike polynomials is based on the fact that the majority of the outputs from the segmented space telescope model are slope measurements from a Shack-Hartmann wavefront sensor. Based on the work of Southwell in [27], these slopes can be related to the partial derivatives of Zernike polynomials given by

$$S^x = \sum_{k=1}^M a_k \frac{\partial Z_k(x, y)}{\partial x} \quad (4.9)$$

$$S^y = \sum_{k=1}^M a_k \frac{\partial Z_k(x, y)}{\partial y} \quad (4.10)$$

where  $S^x$  and  $S^y$  are the  $x$  and  $y$  slope measurements,  $Z_k$  are the Zernike polynomials from Table 2,  $a_k$  are the expansion coefficients in terms of the Zernike polynomials, and  $M$  is the number of polynomials used, in this case 21. The Zernike polynomials are a function of  $x$  and  $y$ , so they must be evaluated at the actual lenslet locations. The process for doing this will be described in Chapter V.

Putting Equations (4.9) and (4.10) into matrix form yields

$$\underline{S} = dZ\underline{a} \quad (4.11)$$

Pre-multiplying both sides of Equation (4.11) by the pseudo-inverse of the matrix of Zernike partial derivatives yields the polynomial coefficient vector

$$\underline{a} = dZ^\dagger \underline{S} \quad (4.12)$$

This technique is used for the first time in this research as a means of performing model reduction to facilitate the design of a robust controller. Chapter V will show how this was accomplished on the analytical model. The original system output of Shack-Hartmann slopes has been replaced by an output of Zernike polynomial coefficients. In the case of the segmented space telescope model, what was originally 732 slope measurements is reduced to 21 coefficient outputs. Clearly, the amount of reduction is equal to the number of Zernike polynomials used.

As will be discussed in Chapter V, the SVD method can be used to reduce both the inputs and the outputs of the model. In this research, the Zernike polynomials were only used to reduce the number of outputs. After the output reduction with Zernike polynomials, an SVD method was used to reduce the number of inputs. Neither of these methods has any affect on the number of states of the system, which is addressed next.



## B. STATE REDUCTION WITH HANKEL SINGULAR VALUES

The Hankel singular value method of model reduction uses a balanced stochastic approach, described in [28], [29], [16], and [30]. It begins by assuming that the system model,  $G$ , is stable and can be partitioned as shown

$$G = \left( \begin{array}{c|c} A & B \\ \hline C & D \end{array} \right) \quad (4.13)$$

From this model, the controllability and observability grammians,  $P$  and  $Q$ , are computed by the following equations

$$P = \int_{-\infty}^{\infty} e^{At} B B^T e^{A^T t} dt \quad (4.14)$$

which satisfies the Lyapunov equation

$$AP + PA^T + BB^T = 0 \quad (4.15)$$

and

$$Q = \int_{-\infty}^{\infty} e^{A^T t} C^T C e^{At} dt \quad (4.16)$$

satisfying

$$A^T Q + Q A + C^T C = 0 \quad (4.17)$$

where  $B$  and  $C$  come from the state space model. The Hankel singular values are then the square root of the product of the largest eigenvalues and the controllability and observability grammians as shown by

$$\sigma_{H_i} = \sqrt{\lambda_i(PQ)} \quad (4.18)$$

Next, a balanced realization is created to balance the controllability and observability grammians. A nonsingular transformation matrix,  $T$ , is introduced such that

$$G = \left( \begin{array}{c|c} \hat{A} & \hat{B} \\ \hline \hat{C} & \hat{D} \end{array} \right) = \left( \begin{array}{c|c} T \hat{A} T^{-1} & T \hat{B} \\ \hline \hat{C} T^{-1} & \hat{D} \end{array} \right) \quad (4.19)$$

which results in the following controllability and observability grammians

$$\hat{P} = T P T^T \quad (4.20)$$

$$\hat{Q} = (T^{-1})^T Q T^{-1}. \quad (4.21)$$

The transformation matrix,  $T$ , can be chosen such that  $\hat{P}$  and  $\hat{Q}$  are diagonal matrices with identical values as shown by

$$\hat{P} = T P T^T = \Sigma \quad (4.22)$$

and

$$\hat{Q} = (T^{-1})^T Q T^{-1} = \Sigma \quad (4.23)$$

where  $\Sigma$  are the Hankel singular values. To determine  $T$ , the singular value decomposition is used.

The Hankel singular values can be placed into a diagonal matrix such that  $\sigma_{\min}(\Sigma_1) \square \sigma_{\max}(\Sigma_2)$

$$\sigma_H = \begin{pmatrix} \Sigma_1 & 0 \\ 0 & \Sigma_2 \end{pmatrix} \quad (4.24)$$

These Hankel singular values can then be plotted to determine how many should be retained and how many should be truncated. The states that are truncated are the least controllable and least observables states of the system, so truncating them will have minimal effect on the system.

The reduced model,  $G_R$ , can be shown to be bounded by the size of the truncated singular values through the following inequality

$$\|G_R - G\|_{\infty} \leq 2tr(\Sigma_2) \quad (4.25)$$

The total number of system states is therefore reduced to the number of Hankel singular values retained.

## V. APPLICATION TO SEGMENTED SPACE TELESCOPE MODEL

### A. MODEL REDUCTION

As described in Chapter II, the segmented space telescope model is extremely large and complex. Before a robust controller can be synthesized for the model, the number of inputs and outputs must be reduced to ease the computational burden. The following discussion will explain two different model reduction techniques used to accomplish this. The first is a Singular Value Decomposition reduction for both inputs and outputs. The second technique first performs a Zernike polynomial reduction on the outputs followed by a Singular Value Decomposition reduction on the inputs. The margins and performance of both controllers are compared against each other.

#### 1. SVD Only Reduction

Recall that the space telescope model is a state space model. It is essentially comprised of four separate matrices, which define a standard state space model as shown by

$$\begin{aligned}\dot{x} &= Ax + Bu \\ y &= Cx + Du\end{aligned}\tag{5.1}$$

A Singular Value Decomposition cannot be performed on a state space model but must be performed on an individual matrix. Therefore, a single matrix representation of the output is defined as

$$y = H(s)u\tag{5.2}$$

where

$$H(s) = C(sI - A)^{-1}B + D\tag{5.3}$$

By letting  $s$  go to zero, the steady state value of this transfer function is obtained which neglects any dynamics of the system

$$H(0) = -CA^{-1}B + D\tag{5.4}$$

Since no dynamics are present, this transfer function can also be thought of as a reconstruction matrix. As discussed in Chapter IV, the SVD of  $H$  yields  $U$ ,  $\Sigma$ , and  $V$  matrices. A plot of the singular values from  $H$  is shown in Figure 22.

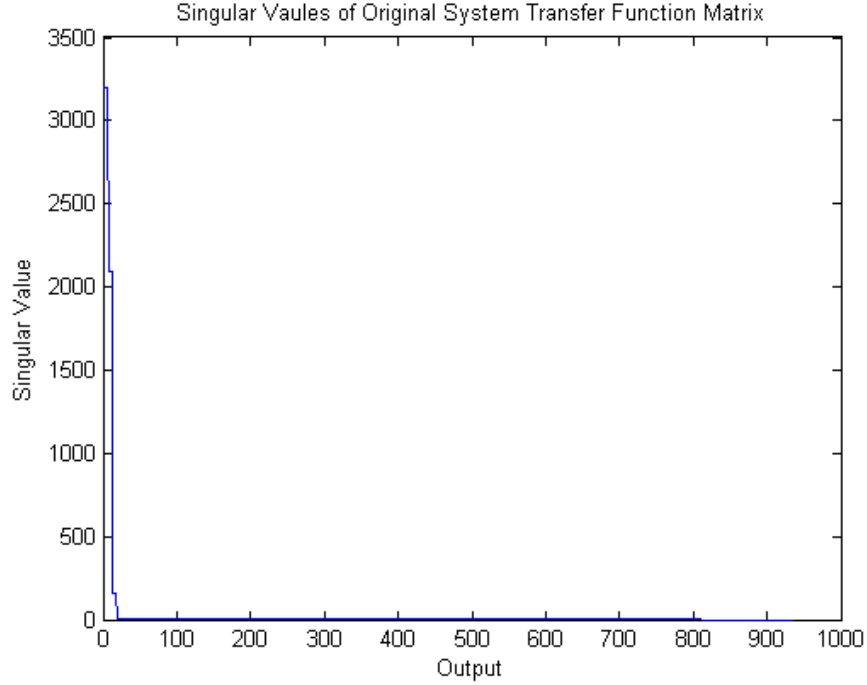


Figure 22 Singular Values from Original System.

The number of rows in the  $U$  matrix corresponds to the total number of sensor outputs in the system. The column vectors represent coefficients of the entire output vector. To reduce the number of system outputs, the columns of  $U$  can be truncated to the desired number of outputs. In this research, 21 outputs were desired, so only the first 21 columns of  $U$  were retained. The reduced size of  $U$  is therefore  $[936 \times 21]$ . Now, define a matrix  $P$  to be the transpose of the reduced  $U$  matrix

$$P = [U_1 \dots U_{21}]^T \quad (5.5)$$

At this point a reduced system output vector,  $\bar{y}$ , can be defined as

$$\bar{y} = Py \quad (5.6)$$

In the same way that the  $U$  matrix from the SVD of  $H$  was used to reduce the number of system outputs, the  $V$  matrix from the SVD of  $H$  can be used to reduce the

system inputs.  $V$  has 997 rows, corresponding to the system inputs. By again selecting the first 21 columns of  $V$  and truncating the rest, we can define a matrix  $M$  with dimensions  $[997 \times 21]$  as

$$M = [V_1 \dots V_{21}] \quad (5.7)$$

The total system input vector,  $u$ , can therefore be defined as

$$u = M\bar{u} \quad (5.8)$$

where  $\bar{u}$  is the reduced input vector. Substituting  $\bar{u}$  and  $\bar{y}$  into the original state space model in Equation (5.1) yields the following input/output reduced state space model

$$\begin{aligned} \dot{x} &= Ax + BM\bar{u} \\ \bar{y} &= PCx + PDM\bar{u} \end{aligned} \quad (5.9)$$

This model is rewritten with new  $\bar{B}$ ,  $\bar{C}$ , and  $\bar{D}$  matrices

$$\begin{aligned} \dot{x} &= Ax + \bar{B}\bar{u} \\ \bar{y} &= \bar{C}x + \bar{D}\bar{u} \end{aligned} \quad (5.10)$$

where

$$\begin{aligned} \bar{B} &= BM \\ \bar{C} &= PC \\ \bar{D} &= PDM \end{aligned} \quad (5.11)$$

At this point, the number of inputs and outputs in the system have been sufficiently reduced such that a robust controller can be synthesized. The only thing that remains is to reduce the number of states of the system. The segmented space telescope model has 332 states. It is possible to generate a robust controller based on a system with this many states; however, decreasing the number of states will facilitate real time implementation. For this research, a state reduction was performed and the procedure for that reduction will be discussed after first applying the innovative method for input/output reduction using Zernike polynomials.

## 2. Zernike Reduction

The process of performing an input/output reduction with Zernike polynomials is actually quite similar to the SVD reduction process previously discussed; however, to avoid confusion and to highlight the subtle differences the entire process will be presented. As before, the original system is given in the state space model shown in Equation (5.1). The key difference in this reduction method occurs at this point. Before anything else is done, the output from the model is reduced into Zernike polynomial coefficients as described in Chapter IV.

The output slopes from the Shack-Hartmann wavefront sensor are equated to the partial derivatives of the Zernike polynomials. Any number of Zernike polynomials may be used; 21 were used for this research. The matrix of Zernike partial derivatives,  $dZ$ , is formed with dimensions of  $[732 \times 21]$  where the number of rows corresponds to the number of Shack-Hartmann slope measurements and 21 is the number of Zernike polynomials used. In order to populate the  $dZ$  matrix with actual values, the physical locations of the lenslets in the model are used. Refer to Figure 23, which shows the lenslet locations and numbering scheme.

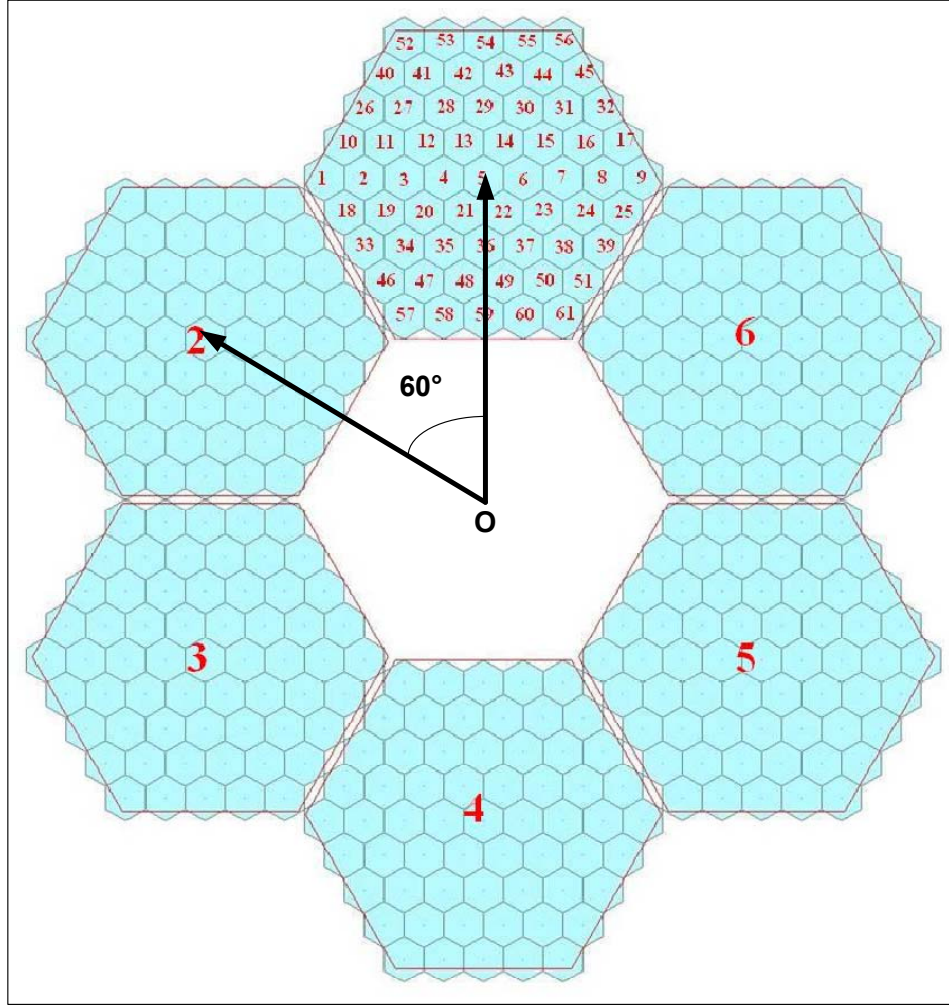


Figure 23 Mirror Segment and Lenslet Orientation.

First, assuming the physical diameter of each lenslet to be 1, the  $x$   $y$  coordinates for the center of each lenslet in segment 1 are computed in relation to the center of lenslet 5, which is at the center of the segment. For example, lenslet 4 has coordinates of  $(-1 \ 0)$  and lenslet 15 has coordinates of  $\left(1.5 \ \frac{\sqrt{3}}{2}\right)$ . The  $y$  coordinates for the lenslets in this segment are then translated a distance of  $9 * \frac{\sqrt{3}}{2}$  from the center of the entire array,  $O$ . Next, the coordinates for the remaining five segments are computed by rotating about a circle, each segment being displaced  $-60^\circ$  from the previous in the segment numbering scheme. Finally, all coordinates are scaled to the actual lenslet diameter and normalized about a unit circle. Then they are substituted into the Cartesian

Zernike polynomial partial derivative equations, which populate the  $dZ$  matrix. The normalized distance from the center of the array is the same as that for lenslets 52 and 56.

The pseudo-inverse of the matrix  $dZ$  is then used to define a new output vector  $y'$

$$y' = dZ^\dagger y \quad (5.12)$$

The  $dZ$  matrix formed from the  $x$  and  $y$  coordinates of the analytical model has a favorable condition number of 9.98. Recall, however, from Chapter II, that the original system model contains more outputs than the 732 Shack-Hartmann slopes. There are 936 total outputs, which include measurements from other sensors as well as the system states. Therefore, a slight modification is made to the pseudo-inverse of the  $dZ$  matrix by adding a block of zeros at the end so that the matrix dimensions match those of the original system. The modified  $dZ^\dagger$  is shown by

$$\text{Zernike reduction matrix} = \left( \begin{array}{c|c} dZ^\dagger & 0 \end{array} \right) \quad (5.13)$$

where the dimensions of the  $dZ^\dagger$  matrix are  $[21 \times 732]$  and the block of zeros has dimensions of  $[21 \times 204]$  yielding a final dimension of  $[21 \times 936]$  for the Zernike reduction matrix.

At this point the output reduced system model has the following form

$$\begin{aligned} \dot{x} &= Ax + Bu \\ y' &= dZ^\dagger Cx + dZ^\dagger Du \end{aligned} \quad (5.14)$$

which can be rewritten as

$$\begin{aligned} \dot{x} &= Ax + Bu \\ y' &= C'x + D'u \end{aligned} \quad (5.15)$$

where

$$C' = dZ^\dagger C \quad (5.16)$$

$$D' = dZ^\dagger D \quad (5.17)$$

Now the process for reducing the system inputs follows very closely to that used in the SVD reduction.

A transfer function matrix,  $H$ , is now defined as

$$H(s) = C'(sI - A)^{-1}B + D' \quad (5.18)$$



Letting  $s \rightarrow 0$

$$H(0) = -C'A^{-1}B + D' \quad (5.19)$$

The SVD for this transfer function of the output reduced system model is taken, which yields the  $U$ ,  $\Sigma$ , and  $V$  matrices as before. Figure 24 shows the singular values from this matrix.

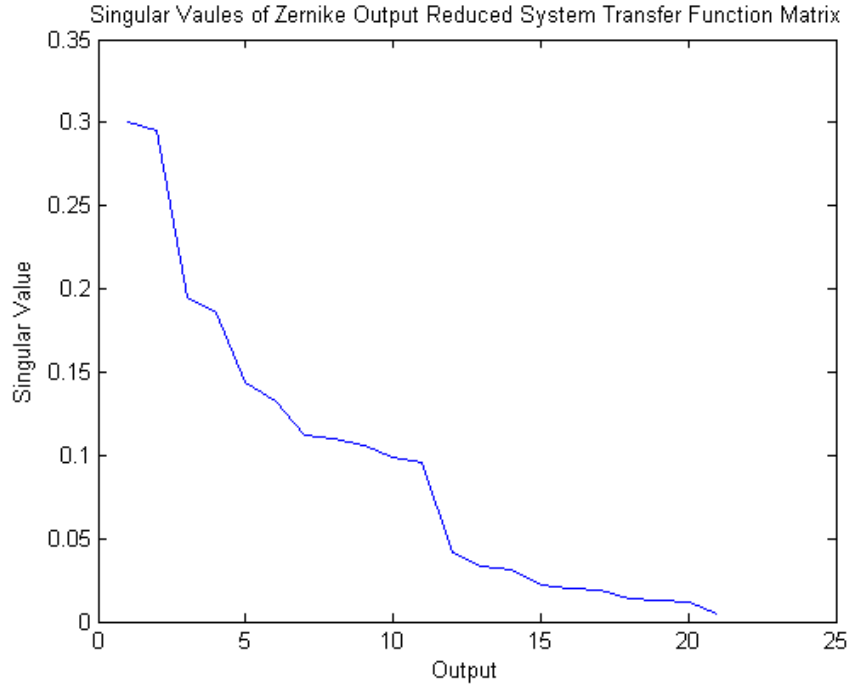


Figure 24 Singular Values from Zernike Output Reduced System.

Since the system has already been output reduced, the  $U$  matrix is not needed this time, and only the  $V$  matrix is used to reduce the inputs. As before, 21 columns of  $V$  are retained so that  $V$  has dimensions of  $[997 \times 21]$ . Defining  $M'$  to be

$$M' = [V_1 \dots V_{21}] \quad (5.20)$$

the total system input vector,  $u$ , can therefore be defined as

$$u = M'u' \quad (5.21)$$

Substituting this into the Zernike reduced system model yields

$$\begin{aligned} \dot{x} &= Ax + BM'u' \\ y' &= C'x + D'M'u' \end{aligned} \quad (5.22)$$

This model can be simplified as before to

$$\begin{aligned}\dot{x} &= Ax + B'u' \\ y' &= C'x + D'u'\end{aligned}\tag{5.23}$$

where

$$B' = BM' \tag{5.24}$$

and  $D'$  is modified from Equation (5.17) to be

$$D' = dZ^\dagger DM' \tag{5.25}$$

At this point, the original system state space model has had its inputs and outputs reduced by two different methods: an SVD only method to reduce both inputs and outputs; and a Zernike polynomial method to reduce the outputs, followed by an SVD method to reduce the inputs. From this point, the remaining steps in designing a robust controller are identical.

### 3. State Reduction

The original system state space model contains 332 states. Neither of the input/output reduction techniques discussed has changed or altered the number of states. As mentioned above, a state reduction is not needed to generate a controller; however, the designed controller will have the same number of states as the system it is designed to control. Therefore, it may be advantageous to reduce the number of system states prior to generating the controller in order to facilitate real time implementation on a system.

Equations (5.10) and (5.23) both represent input/output reduced state space models, one for each reduction technique used. From this point on, the discussion will use the nomenclature used in Equation (5.10), although nomenclature from either equation would be suitable.

The number of system states is reduced using the Hankel Singular Value state reduction techniques discussed in Chapter IV. A plot of the Hankel Singular Values from the input/output reduced system model is shown in Figure 25.

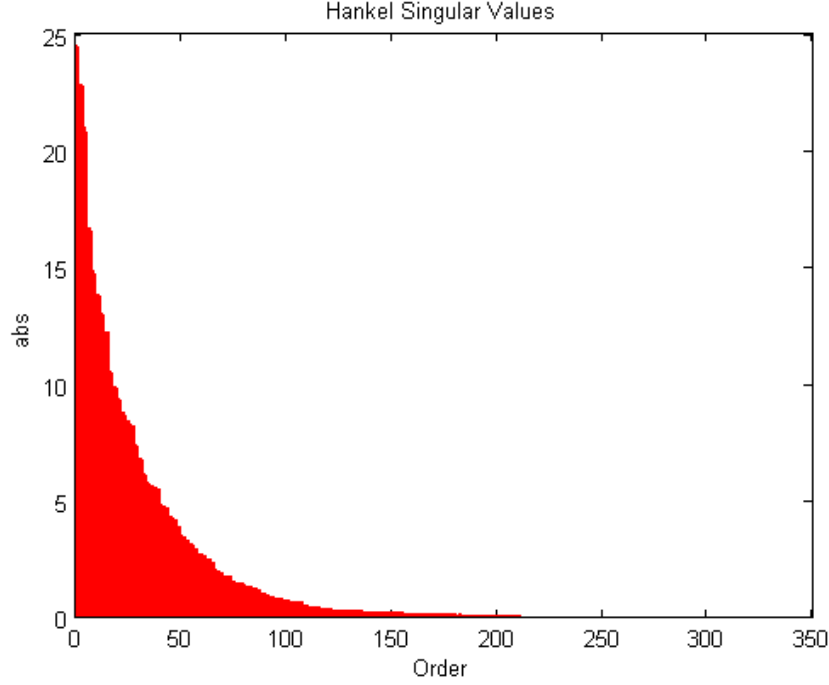


Figure 25 Hankel Singular Values.

Based on this graph, the decision was made to reduce the number of system states to 240, thereby retaining the most significant singular values. By defining  $\bar{x}$  as the Hankel reduced state, the new system state space model can be written as

$$G_R = \begin{cases} \dot{\bar{x}} = A'\bar{x} + \bar{B}'\bar{u} \\ \bar{y}' = \bar{C}'\bar{x} + \bar{D}\bar{u} \end{cases} \quad (5.26)$$

where  $A'$ ,  $\bar{B}'$ ,  $\bar{C}'$ , and  $\bar{y}'$  all reflect the reduced number of states. This system contains 240 states, 21 inputs, and 21 outputs. From here it is possible to proceed with the robust controller synthesis.

## B. ROBUST CONTROLLER SYNTHESIS

After the model is sufficiently reduced to allow synthesis of a robust controller, the next step in the process is to generate the 2-input, 2-output construct as shown in Figure 19. Part of this process involves incorporating the weights,  $W_1$  and  $W_3$ .  $W_1$  is the weight on the error between the reference signal and measured output;  $W_3$  is the weight

on the measured output. For this design, first order transfer functions were chosen for each and are shown in Equation (5.27) and Equation (5.28). Figure 26 shows a Bode plot of  $W_1$  and the inverse of  $W_3$ .

$$W_1 = \frac{0.5s + 17.32}{s + 0.3465} \quad (5.27)$$

$$W_3 = \frac{10s + 2095}{s + 2116} \quad (5.28)$$

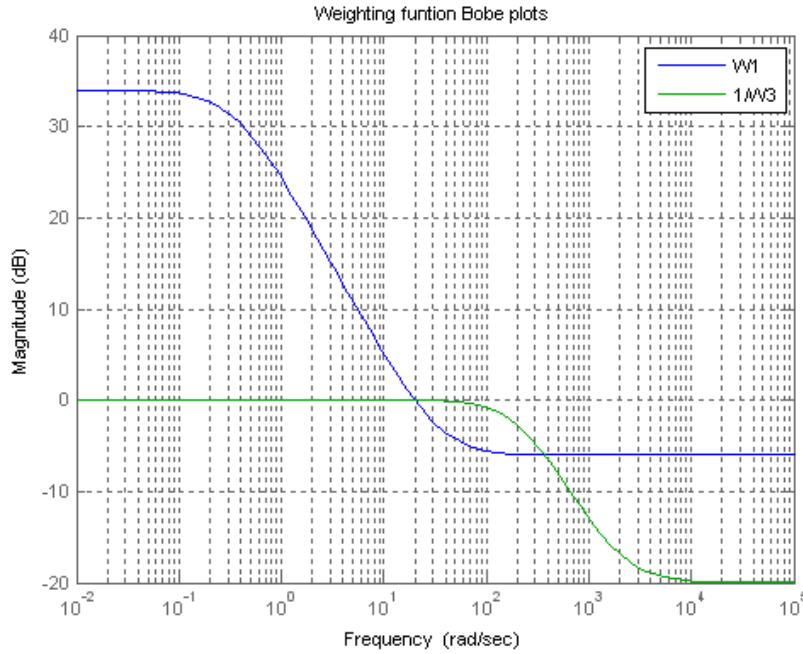


Figure 26 Model Weighting Function Bode Plot.

Each weighting function specifies a low frequency gain, a crossover frequency, and a high frequency gain. The effect is analogous to classical loopshaping techniques. These transfer functions were determined based on their ability to achieve the desired bandwidth for the closed loop system, while at the same time not being so restrictive as to preclude the synthesis of a robust controller. The desired control bandwidth for the space telescope model was 10 Hz. The classical controller designed for the model was unable to achieve this bandwidth, which was a driving motivation for this research into robust control techniques.

The result of augmenting the reduced system model with these weighting functions is a system in the form shown in Figure 19. The total number in inputs in this augmented system is 42, resulting from 21 inputs from the reference signal and 21 inputs from the control signal. There are 63 total outputs in the augmented system resulting from 21 error signal outputs multiplied by  $W_1$ , 21 measured outputs multiplied by  $W_3$ , and 21 error signal outputs sent to the controller. The augmented model has 440 states. The  $H_\infty$  robust controller that is synthesized for this system has 21 inputs, 21 outputs, and 440 states regardless of whether the model reduction is performed with the SVD only method or the Zernike polynomial / SVD combination. This controller can now be used to check the performance on the original plant model. The results from these simulations are given in Chapter VI.

### C. PERFORMANCE AND STABILITY MARGINS

The first analysis of the quality of the two robust controllers designed is accomplished by examining the poles of the controllers. Figure 27 and Figure 28 show the location of the poles for the closed loop system from each controller. The closed loop system combines the  $H_\infty$  controller with the full plant and assumes negative unity feedback. The poles for each controller are plotted on the same scale.

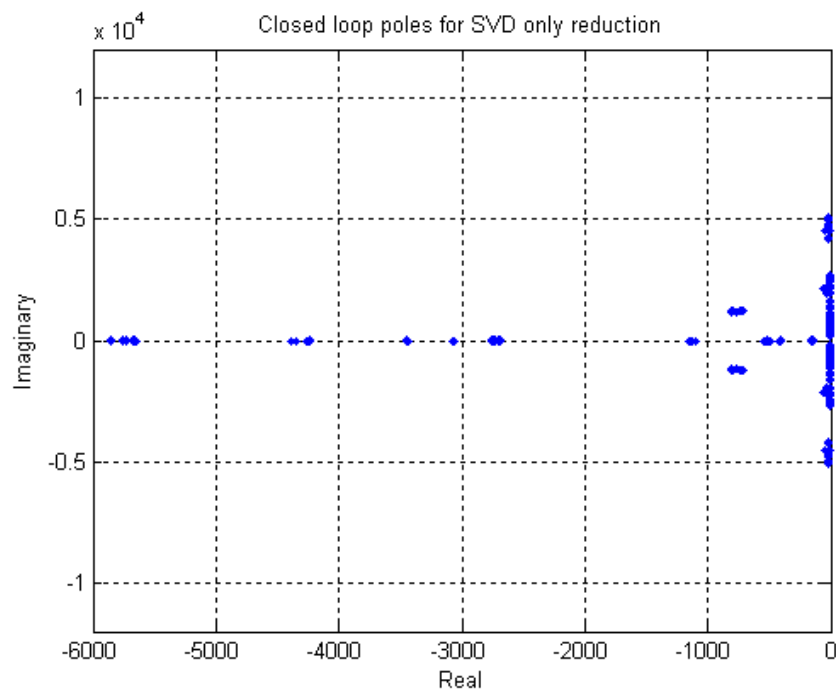


Figure 27 Closed Loop Poles for SVD only Reduced Model.

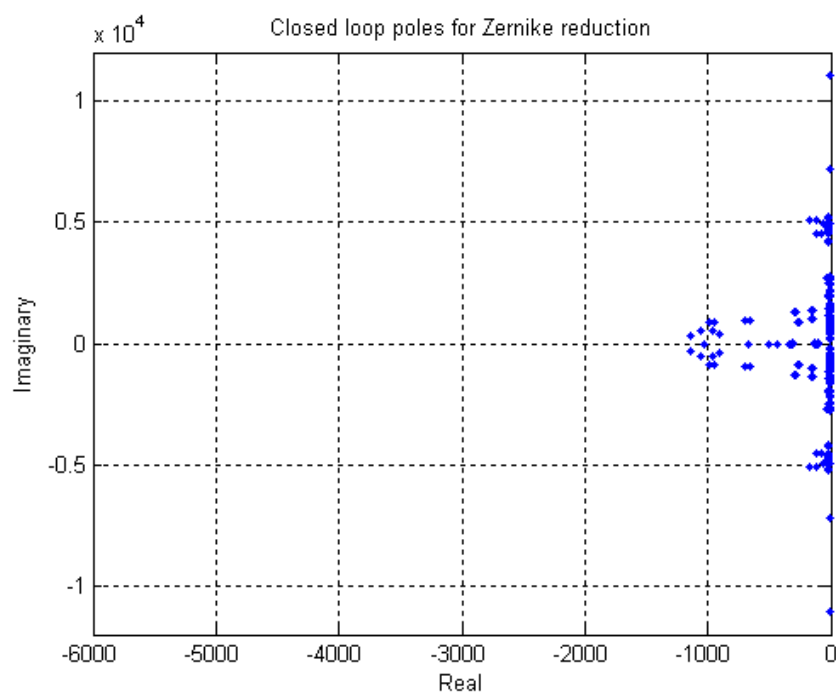


Figure 28 Closed Loop Poles for Zernike Polynomial Reduced Model.

The following show the same results zoomed in on the area near the imaginary axis.

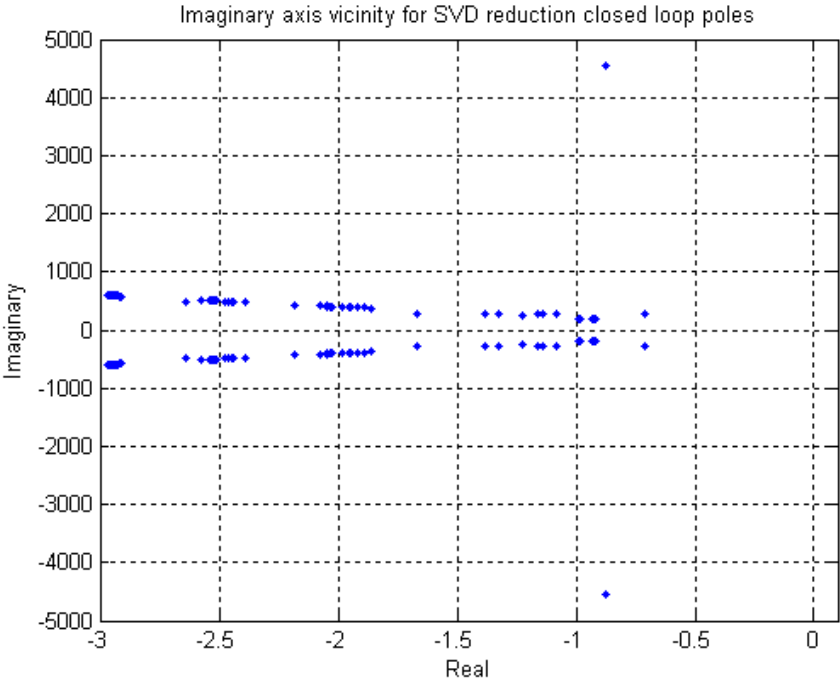


Figure 29      Imaginary Axis Vicinity for SVD Reduction Closed Loop Poles.

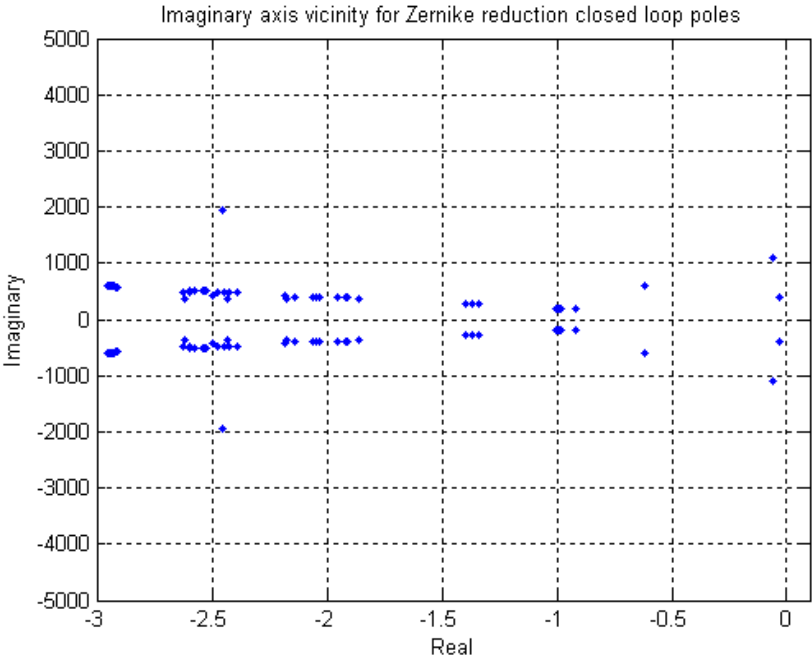


Figure 30      Imaginary Axis Vicinity for Zernike Polynomial Reduction Closed Loop Poles.

As can be seen in the plots, the controller for the Zernike polynomial reduced model has poles much closer to the imaginary axis; however, in both cases all poles are in the left half-plane, indicating the stability of the closed loop systems. Table 3 summarizes the poles that are closest to the imaginary axis for each of the model reduction techniques for both closed loops systems.

<u>SVD Reduced Model</u>	<u>Zernike Reduced Model</u>
$-0.7118 \pm 268.69i$	$-0.0327 \pm 406.1887i$
$-0.8729 \pm 4545.6023i$	$-0.0623 \pm 1098.7036i$
$-0.9149 \pm 182.9182i$	$-0.6178 \pm 588.1804i$

Table 3 Closed Loop Poles Closest to  $j\omega$  Axis.

The next level of analysis looks at the singular values of the plant, the controllers, and the closed loop systems. Recall that a singular value plot is the MIMO equivalent to the Bode magnitude plot of a SISO system. Figure 31 shows the singular values for the input/output reduced plant with all 332 states. Computing the singular values on the full plant with all inputs and outputs was too computationally intensive.

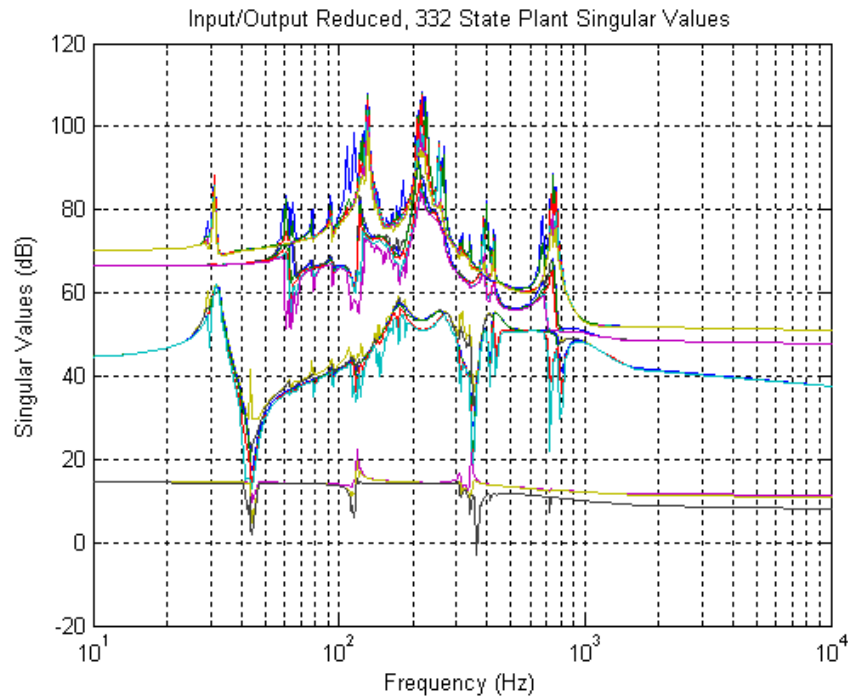


Figure 31 Singular Values for Original System Model,  $G_{red}$ .



As evident in this plot, the main natural frequencies of the plant occur between 31 and 760 Hz. A properly designed controller will provide stability and negate any adverse effects due to these resonances in achieving the desired closed loop performance.

The singular values for the controller from the SVD only reduced model and from the Zernike polynomial reduced model are shown in Figure 32 and Figure 33. The controller is represented by  $K_{SVD}$  or  $K_{Zern}$  depending on how the model reduction was performed. In both cases, the plots have been zoomed in on the applicable range of frequencies between 31 and 760 Hz where the controllers have been designed to handle the resonances. Based on a visual comparison, it appears that both controllers should be able to compensate for the resonances in the system and provide stability. This observation will be verified for the closed loop system.

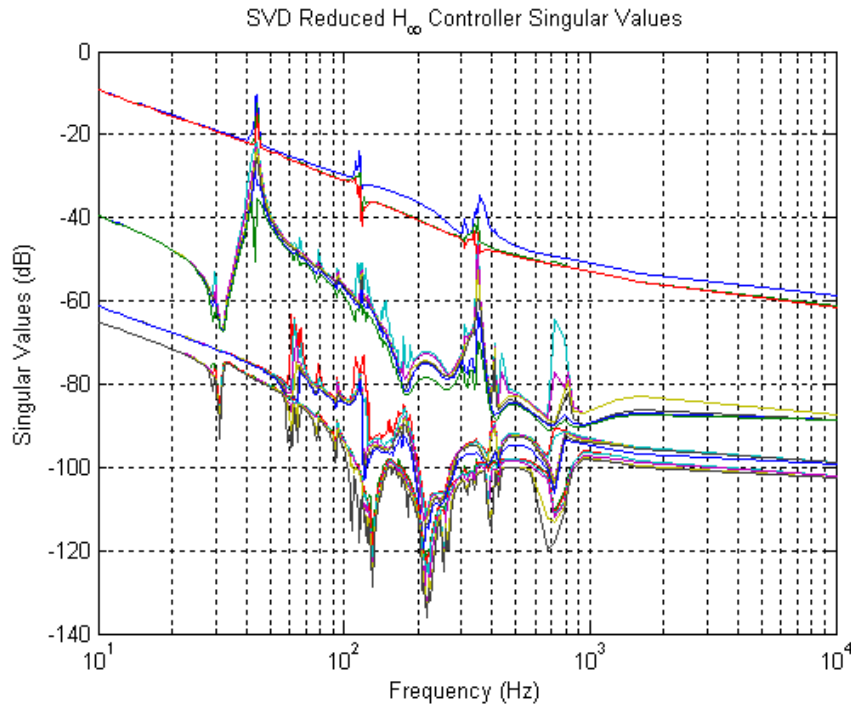


Figure 32 Singular Values for  $H_\infty$  Controller,  $K_{SVD}$ .

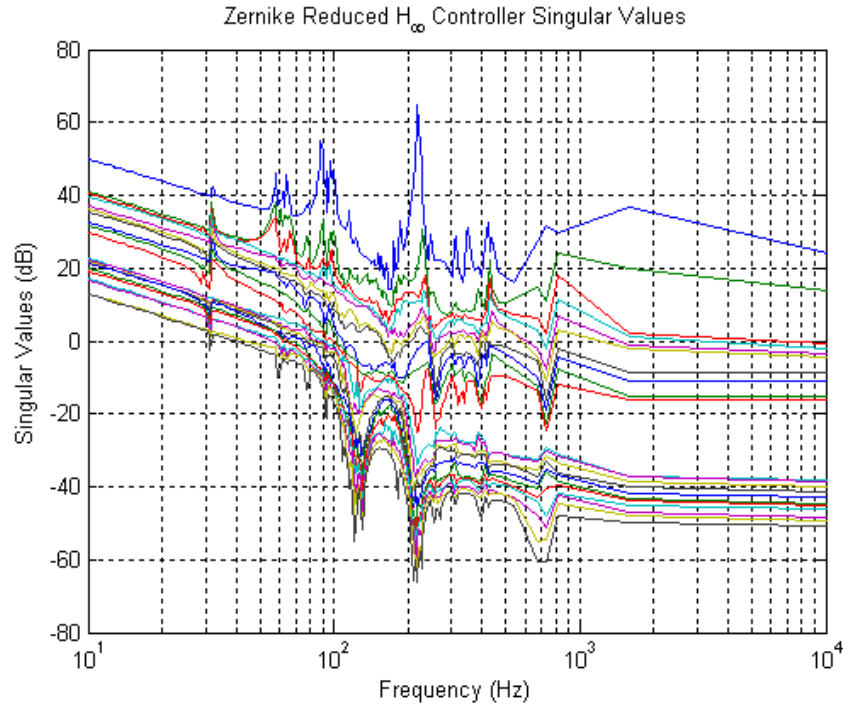


Figure 33 Singular Values for  $H_\infty$  Controller,  $K_{Zern}$ .

The next analysis is to examine the open loop singular values shown in Figure 34 and Figure 35. The open loop system is calculated as either  $GK_{SVD}$  or  $GK_{Zern}$ . Notice in these two plots that the curve is smoother for the controller based on the Zernike reduced model. There are fewer residual peaks left from the natural frequencies of the system. This is an indication that the controller for the Zernike reduced model more closely matches the original system. It is better able to compensate for the plant's natural frequencies. While not an indication of performance or robustness, this is an indication that the controller should be stable.

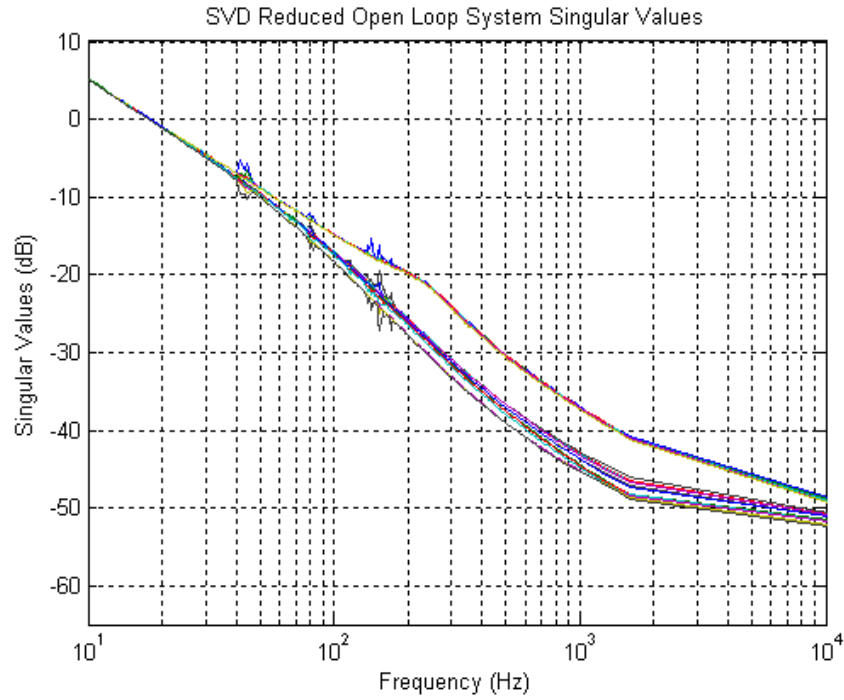


Figure 34 Open Loop System Singular Values for  $GK_{SVD}$ .

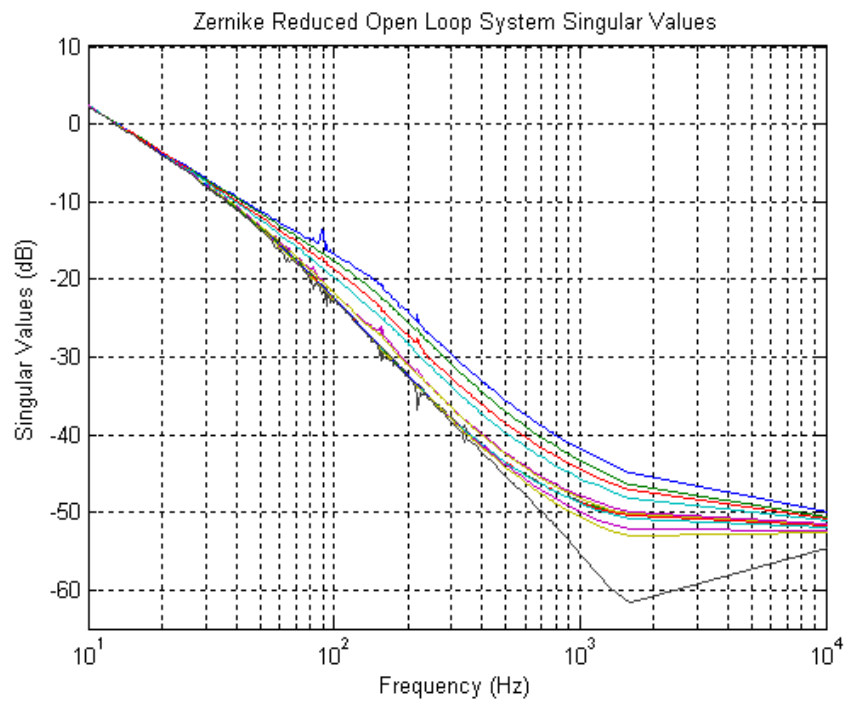


Figure 35 Open Loop System Singular Values for  $GK_{Zern}$ .

Next, the closed loop system is formed by providing a unity negative feedback loop to the open loop systems  $GK_{SVD}$  and  $GK_{Zern}$  as shown by

$$y = \frac{GK_{SVD}}{1 + GK_{SVD}} r \quad (5.29)$$

$$y = \frac{GK_{Zern}}{1 + GK_{Zern}} r \quad (5.30)$$

The singular value plots from both closed loop systems are shown in Figure 36 and Figure 37.

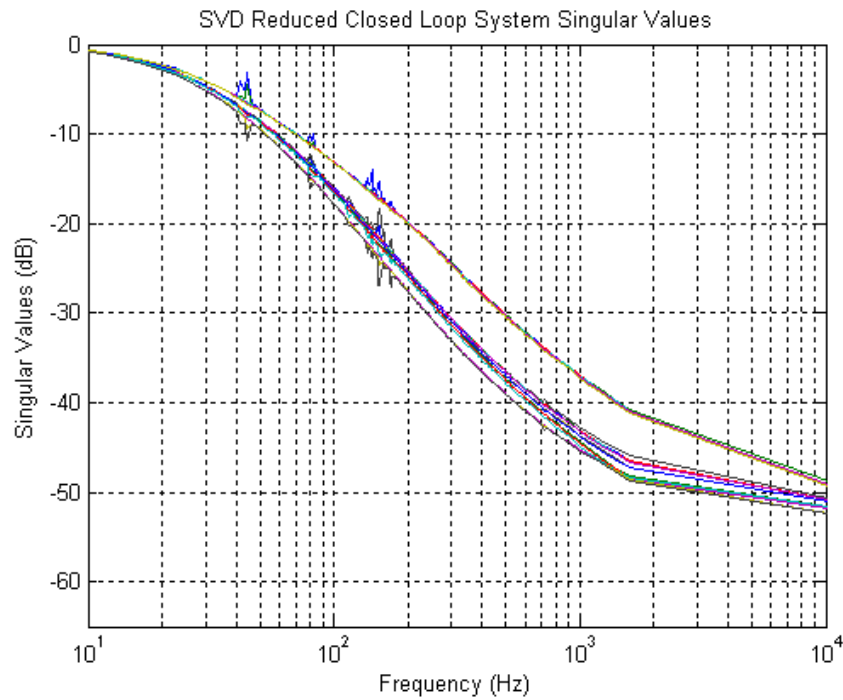


Figure 36 Closed Loop System Singular Values for  $GK_{SVD}$ .

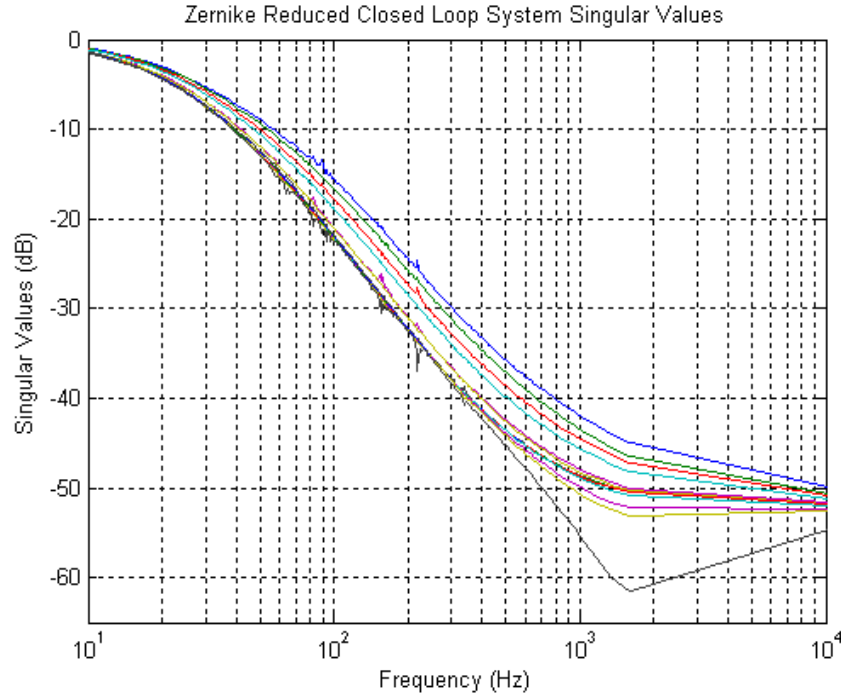


Figure 37 Closed Loop System Singular Values for  $GK_{Zern}$ .

As with the open loop singular value plots, the smoother shape of the Zernike reduced controller closed loop singular value plot indicates that it more closely matches the natural frequencies of the original plant. This observation will be checked in the simulation analyses.

The shape of the open and closed loop singular value plots for both controllers matches the desired shape specified by the weighting functions shown in Figure 26. The weighting functions specified a low frequency performance requirement with a gain no larger than 5 dB at 10 Hz. It also satisfies the high frequency robustness requirement of no more than -15 dB at 1000 Hz.

Also evident in the singular value plots is the control bandwidth for each controller. The bandwidth was determined by identifying where the singular value plots crossed the -3dB line for the closed loop system. The SVD reduced model controller has a control bandwidth in the range of 20-24 Hz, whereas the Zernike reduced model controller bandwidth resides from 15-19 Hz. Both of these bandwidths are higher than

that obtained using classical control methods leading to the conclusion that the robust control techniques employed in the design process provide better performance and are better able to accomplish disturbance rejection.

#### D. ANALYTICAL RESULTS

This chapter will present simulation results for the two different robust controllers developed for the segmented telescope model. One controller was designed based on a model whose inputs and outputs were both reduced by the SVD technique; the model for the other controller had its outputs reduced with Zernike polynomials and inputs reduced with the SVD technique. The Hankel singular value state reduction and all other aspects of controller design were identical.

A simple Simulink model shown in Figure 38 was used to validate the performance of both controllers.

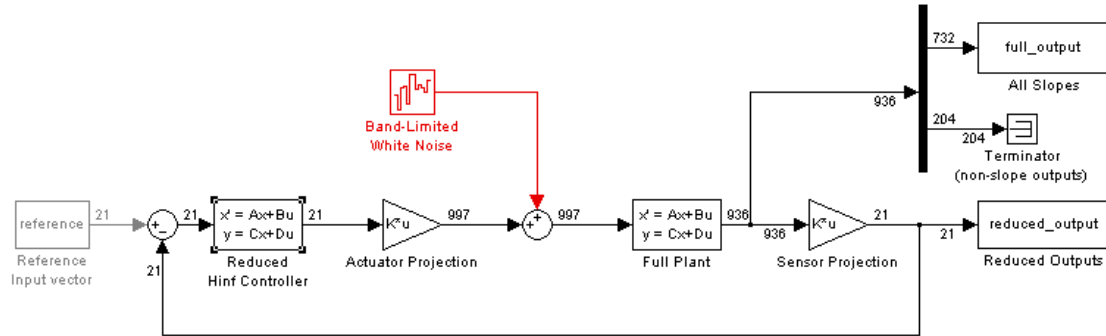


Figure 38 Segmented Space Telescope Controller Validation Model.

The full plant used for both cases was the original 997 input, 936 output, 332 state model. The controller for both cases had 21 inputs and 21 outputs. The number of states in the controller does not have to match the number of states in the original plant as long as the inputs and outputs go through the appropriate projection. The full output that was sent to the workspace for plotting consisted of only Shack-Hartmann slope data. The phase diversity and other outputs were discarded and not plotted. The actuator projection is the SVD reduction of the inputs, which consists of the first 21 columns of the  $V$  matrix

obtained from the SVD. This recreates the full control,  $u$ , from the modified control,  $\bar{u}$ , generated from the reduced controller. Equation (5.8) describes this process.

For the case of the Zernike polynomial reduced model, the following conditions apply. The reference input vector and the reduced output sent to the workspace were both the Zernike polynomial coefficients. The sensor projection is the pseudo-inverse of the  $dZ$  matrix formed from the partial derivatives of the Zernike polynomials. The reduced output becomes that as shown in Equation (5.12).

For the case of the SVD only reduced model, the following conditions apply. The reference input vector and the reduced output sent to the workspace were both the coefficients of the full output vector. The sensor projection is the transpose of the first 21 columns of the  $U$  matrix formed from the SVD of the model. The reduced output becomes that as shown in Equation (5.6).

The band-limited white noise was used to add disturbances to the simulation. In some cases no disturbance was added, but when it was added, it provided a random step to all control inputs at a specified time interval. Figure 39 shows what this would look like. This type of disturbance can be thought of as a changing initial condition as would be encountered if the space telescope performed a slewing maneuver to acquire a new target.

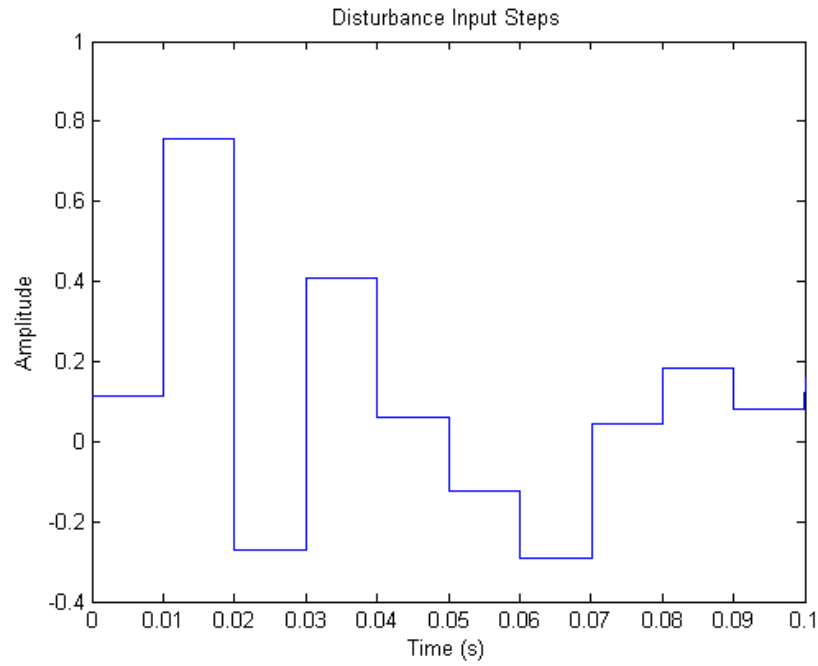


Figure 39 Disturbance Input Representation.

## 1. System Performance

The first test of the controller performance was how well the system could track a step input of 0.2 on all reference inputs. Figure 40 and Figure 41 show the results for both controllers.



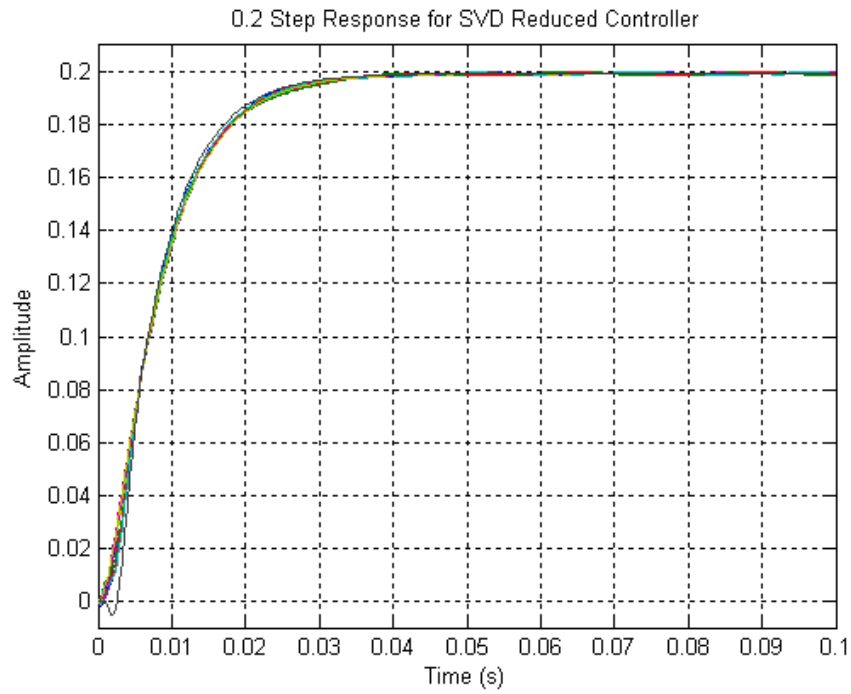


Figure 40 Step Input for SVD Only Reduced Model.

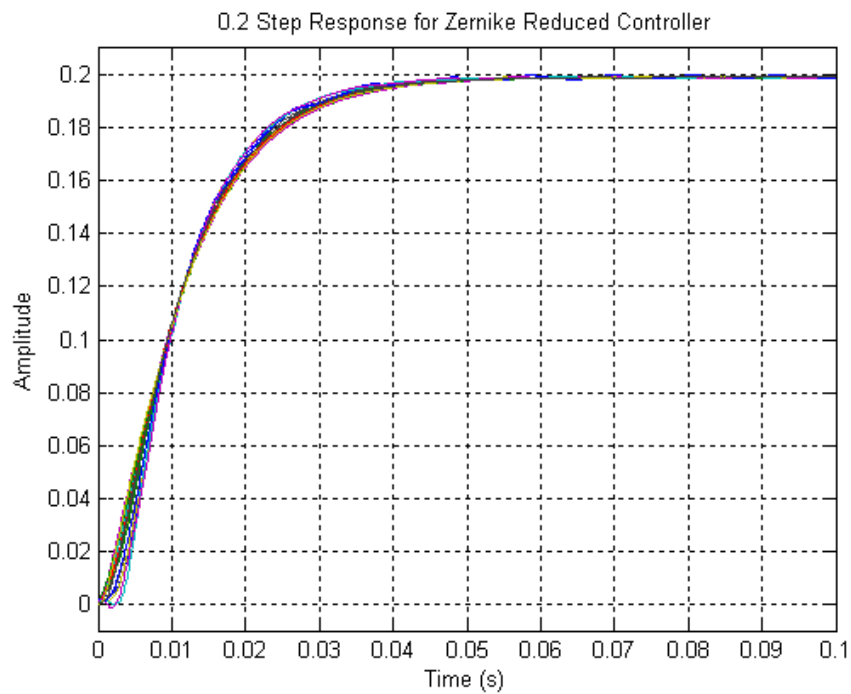


Figure 41 Step Input for Zernike Polynomial Reduced Model.

These plots were only used to verify that each controller is capable of achieving a desired steady state response to a specified reference input. In this case, both controllers are capable of accomplishing this. No attempt was made at comparing the performance of the two controllers based on these plots, however, since the output is different in each case. For the SVD reduced controller, the output is a coefficient of a total output vector, whereas the output of the Zernike reduced controller is a Zernike polynomial expansion coefficient.

## 2. Disturbance Rejection

Now that both controllers have been shown to be stable and can achieve a desired steady state, it is time to compare their performance. The performance criterion is to achieve a planar wavefront, or in other words, the slopes from the Shack-Hartmann wavefront sensor should approach zero. An equivalent statement is that the expansion coefficients of the Zernike polynomials all become zero. If the Zernike polynomial expansion coefficients are zero then there are no aberrations in the wavefront with the possible exception of a piston component, which is not measurable in this setup. All other aberrations should be zero.

In order to make a valid comparison, the output from each controller needs to represent the same data. Recall, however, that the output from the SVD reduced controller was not a Zernike polynomial expansion coefficient, but rather a coefficient on the total output. This difference can be remedied by converting the full slope output from the SVD reduced controller in a Zernike polynomial expansion coefficient. This is done by multiplying the full output by the pseudo-inverse of the  $dZ$  matrix from Equation (5.12). In the simulation block diagram, this is represented by the extra block in green in Figure 42.

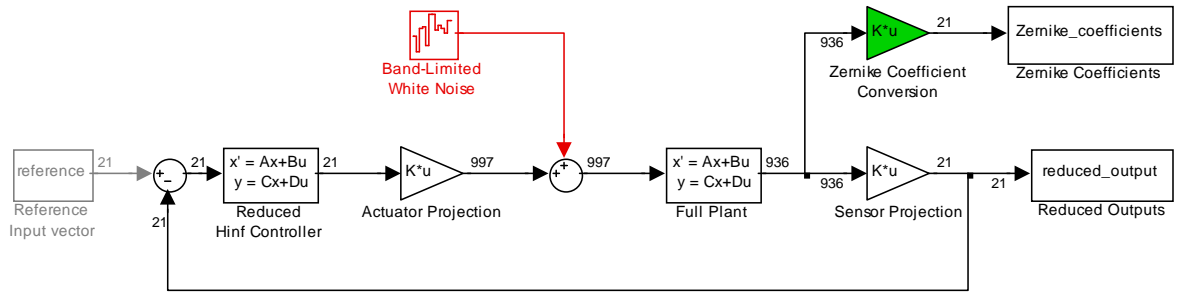


Figure 42 Simulation Model with Zernike Coefficient Conversion.

The simulation was run for 4.1 seconds with a reference input of zero. The band limited white noise disturbance represented in Figure 39 was set to provide a new random step disturbance every second. The output from the SVD reduced controller, converted to Zernike polynomial expansion coefficients, is shown in Figure 43.

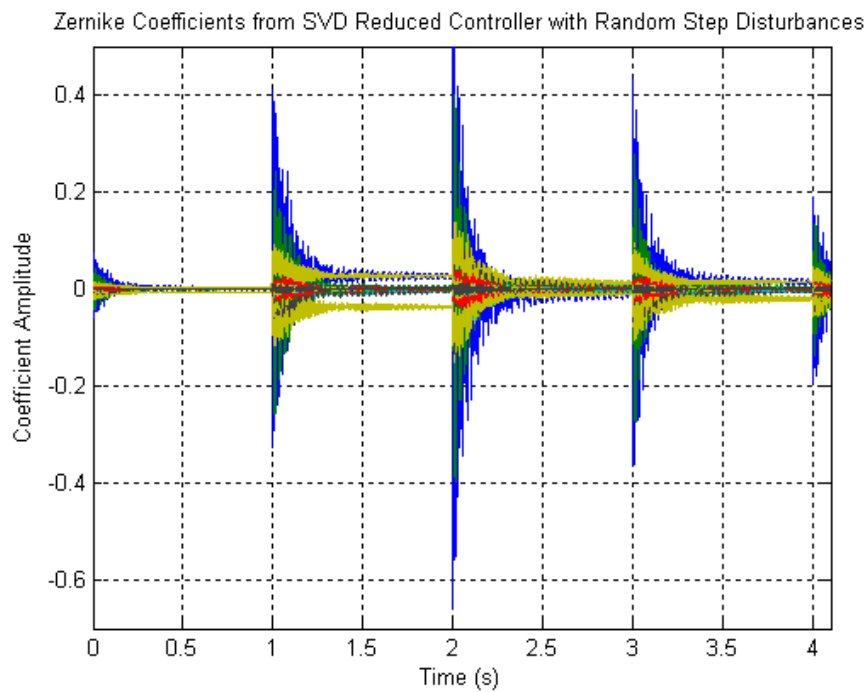


Figure 43 Zernike Polynomial Coefficients in Presence of Random Disturbance for SVD Reduced Controller.

Notice how the controller does a good job of bringing the disturbance back close to zero in about 0.5 seconds. However, some of the coefficients asymptotically go to other non-zero values and exhibit oscillatory behavior around those values. In some cases, the coefficients are off by as much as  $\pm 0.04$ . This result can be compared with that of the Zernike reduced controller shown in Figure 44.

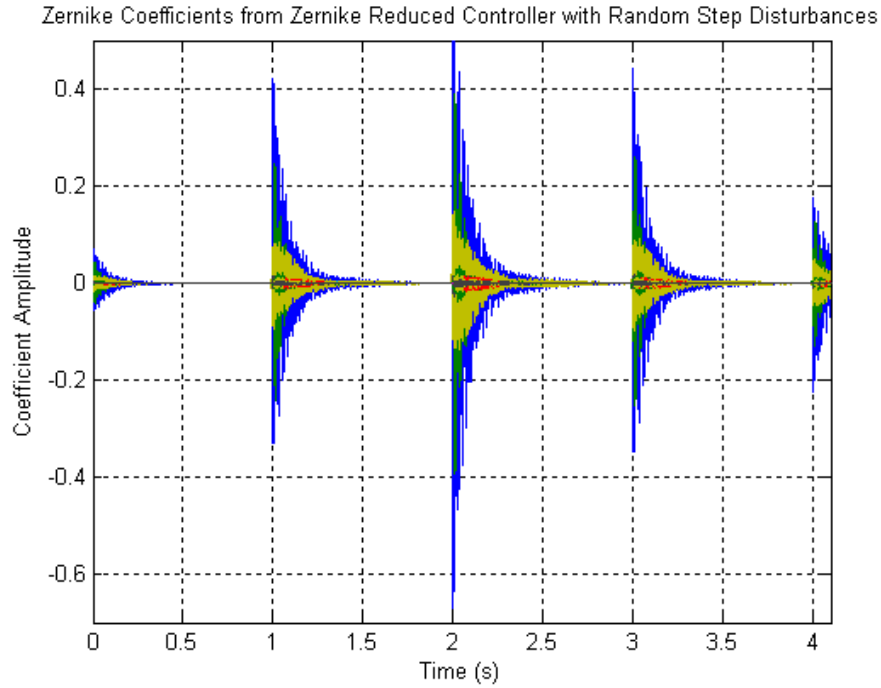


Figure 44 Zernike Polynomial Coefficients in Presence of Random Disturbance for Zernike Reduced Controller.

Notice here that in roughly the same amount of time the Zernike reduced controller drives all Zernike polynomial coefficients to a zero value with negligible deviation from zero and negligible oscillatory behavior in the steady state. The conclusion from this simulation is that the  $H_{\infty}$  robust controller synthesized for the Zernike polynomial reduced model is better at achieving a planar wavefront in the presence of disturbances. This is not an unexpected conclusion, since the Zernike polynomial reduction was theorized to be uniquely suited to reduce the Shack-Hartmann wavefront sensor outputs of the segmented space telescope model.

## **VI. EXPERIMENTAL APPLICATION TO ADAPTIVE OPTICS TESTBED**

### **A. SYSTEM IDENTIFICATION**

This chapter will describe the work to adapt the robust control techniques for use on the Spacecraft Research and Design Center's adaptive optics testbed, as described in Chapter II. As noted in the literature [9], this is not the first use of a robust controller designed for a laboratory testbed. The intent here is not to replicate the previous work done, but to validate the design process used for the analytical model on testbed hardware.

To do this, a robust controller was designed for the first deformable mirror / wavefront sensor closed loop system on the SRDC testbed. It was originally thought that since the first deformable mirror was an extremely thin membrane mirror, it would be lightweight and prone to have low natural frequencies just as a lightweight segmented space telescope mirror would. This would allow verification of the robust control techniques on systems with unmodeled system dynamics.

The difficulty is that no model of the actual hardware exists. Therefore, it was necessary to perform a system identification on the mirror to determine its natural frequencies. Using a position sensing device it was determined that the lowest natural frequency was around 918 Hz, much higher than originally thought. It is believed that the electrostatic actuators provide a degree of rigidity to the system, thus reducing the amount of dynamics that might be present in the system. In the design of actual flight systems, this would actually be a benefit as there would be less uncertainty in the system that the controller must be able to handle. For the purposes of this research, however, it meant that a new approach had to be developed.

### **B. ROBUST CONTROLLER SYNTHESIS**

Since the natural frequencies of the membrane deformable mirror were around 918 Hz, it was decided that the mirror could be modeled as a static system and a robust controller designed for this static system. During real time wavefront correction,

disturbance inputs could be injected into the system and the robust controller performance measured in the presence of these disturbances.

The best choice for a static system model is the reconstruction or influence matrix of the system. Recall that the reconstruction matrix is obtained by actuating (poking) each of the mirror actuators in turn, allowing sufficient settling time, and measuring the resulting effect on the wavefront with the Shack-Hartmann wavefront sensor. In classical control applications, the wavefront,  $\phi$ , is measured and multiplied by the inverse (or in this case the pseudo-inverse) of the reconstruction matrix,  $R$ , to determine the control input,  $u$

$$u = R^\dagger \phi \quad (6.1)$$

In the case of the membrane deformable mirror on the Spacecraft Research and Design Center AO testbed, the control input is a vector of 37 actuator voltages, one for each actuator. The wavefront measurement is a vector of 254 slopes, two for each Shack-Hartmann lenslet. The reconstruction matrix therefore has dimensions of [254 x 37]. The large difference between the number of rows and columns in this matrix is one factor that increases the condition number to the rather high value of 33,628. This can lead to numerical error when taking the pseudo-inverse of this matrix by the Moore-Penrose method as given by

$$X^\dagger = X^T (XX^T)^{-1} \quad (6.2)$$

What is needed then is a way to reduce the number of measurements. The previously discussed method of model reduction with Zernike polynomials is quite appropriate for this task. By using the Zernike polynomial output reduction method employed on the analytical model and projecting the 254 slope measurements into 21 Zernike polynomials, the resulting vector has only 21 coefficients. This reduced reconstruction matrix now has dimensions of [21 x 37], with a reduced condition number of 257 and a less complex model on which to design a robust controller. This reduced reconstruction matrix is used with the following weighting functions to generate the robust controller

$$W_1 = \frac{0.5s + 17.32}{s + 0.3465} \quad (6.3)$$

$$W_3 = \frac{10s + 2095}{s + 2116} \quad (6.4)$$

A plot of these weighting functions is show in Figure 45.

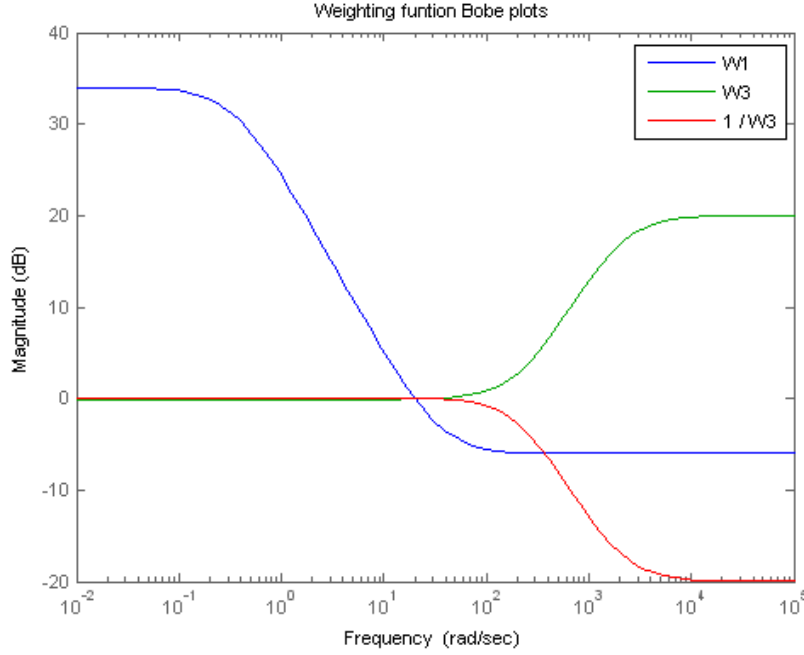


Figure 45 AO Testbed Robust Controller Weighting Functions.

The resulting  $H_\infty$  controller is a state space model with 21 inputs, which are the Zernike polynomial expansion coefficients, 37 outputs, which are translated into actuator voltages, and 42 states. When the controller is implemented on the testbed, these 42 states must be integrated for each iteration through the control loop. In order to minimize the computational effort associated with all these integrations, the continuous  $H_\infty$  controller is discretized for implementation according to the following set of equations

$$\begin{aligned} x(k+1) &= Ax(k) + Bu(k) \\ y(k) &= Cx(k) + Du(k) \end{aligned} \quad (6.5)$$

The singular value plot of the AO testbed controller is shown in Figure 46.

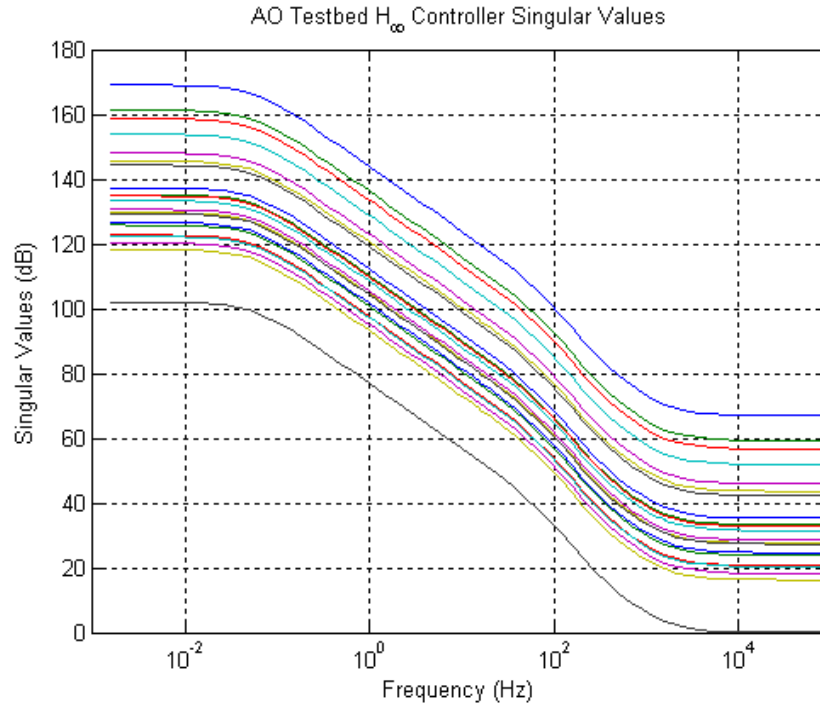


Figure 46 AO Testbed Controller Singular Values.

Figure 47 and Figure 48 show the testbed open loop and closed loop singular values.

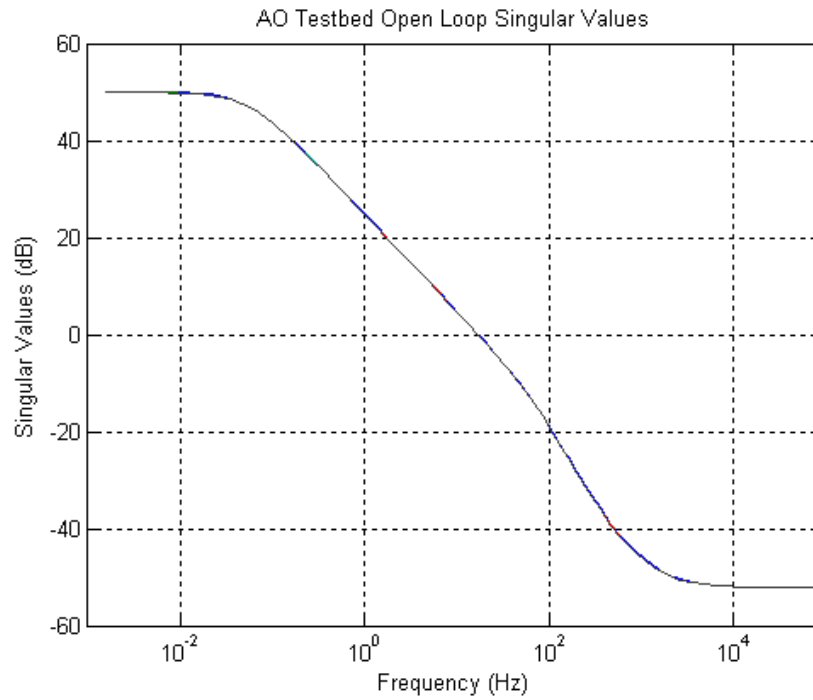


Figure 47 AO Testbed Open Loop Singular Values.



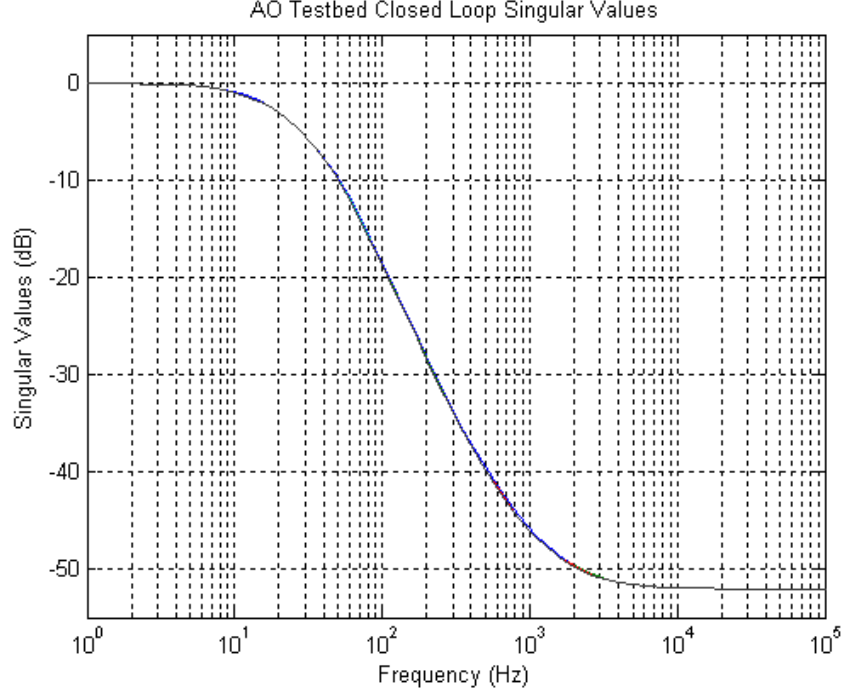


Figure 48 AO Testbed Closed Loop Singular Values.

The smoothness of these plots is attributable to the fact that there are no dynamics or resonances in the model used. There is nothing in these plots to indicate that the  $H_\infty$  controller designed for the testbed will be ineffective at correcting the wavefront aberrations. The experimental results will show this to be the case.

## C. EXPERIMENTAL RESULTS

### 1. System Performance

The results of the AO testbed controller will be compared with the results obtained using a classical reconstruction matrix approach. The wavefront estimation was performed by relating the Shack-Hartmann wavefront sensor slope measurements to the partial derivatives of the Zernike polynomials as shown in Equations (4.9) and (4.10). The control law used an iterative feedback loop based on the reconstruction matrix as developed in [3] and given as

$$\underline{u}_{n+1} = \underline{u}_n - gR^\dagger \underline{a}_n \quad (6.6)$$

where  $g$  is a gain, and  $\underline{a}$  is the vector of Zernike polynomial expansion coefficients for each iteration,  $n$ . Before describing the performance, it is necessary to describe the evaluation criteria used.

The first performance measure used is the peak-to-valley wavefront aberration. This figure of merit is a sum of the absolute values of the minimum and maximum deviation from a planar wavefront. The resulting number is a representation of the number of waves of aberrations present. The piston, tip, and tilt aberrations present in the wavefront are neglected in order to allow examination of the underlying higher order aberrations. The peak-to-valley wavefront error is then represented in a three-dimensional circular plot.

The second performance measure is the root mean square (RMS) error. This figure of merit is the square root of the wavefront variance and is given as

$$\sigma_\phi^2 = \frac{1}{\pi} \int_{-1}^1 \int_{-\sqrt{1-x^2}}^{\sqrt{1-x^2}} [\phi(x, y) - \phi_0(x, y)]^2 dx dy \quad (6.7)$$

This variance is related to the Zernike polynomial coefficients through the following relationship, where the reference wavefront,  $\phi_0$ , is assumed to be planar

$$\phi(x, y) - \phi_0(x, y) = \sum_{k=1}^M a_k Z_k(x, y) \quad (6.8)$$

The RMS error can then be written as

$$\sigma_\phi = \sum_{k=1}^M \sqrt{a_k^2 \frac{1}{\pi} \int_{-1}^1 \int_{-\sqrt{1-x^2}}^{\sqrt{1-x^2}} [Z_k(x, y)]^2 dx dy} \quad (6.9)$$

where  $a_k$  has been pulled in front of the integral because it is a constant.

The control loop was run for 100 iterations with each controller. At the end of each run, the wavefront was sampled with a science camera to determine the final wavefront peak-to-valley error. A representation of the wavefront for each simulation was plotted. The RMS error for each iteration was also plotted. The results of the classical controller are shown in Figure 49 and Figure 50. A gain value of 0.1 was used.

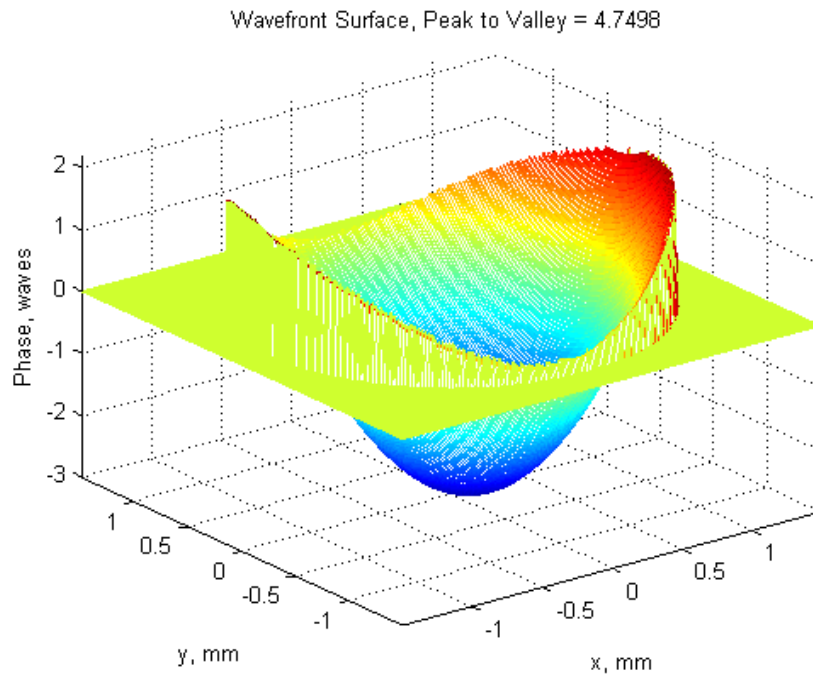


Figure 49 Classical Controller Peak-to-Valley Wavefront Error.

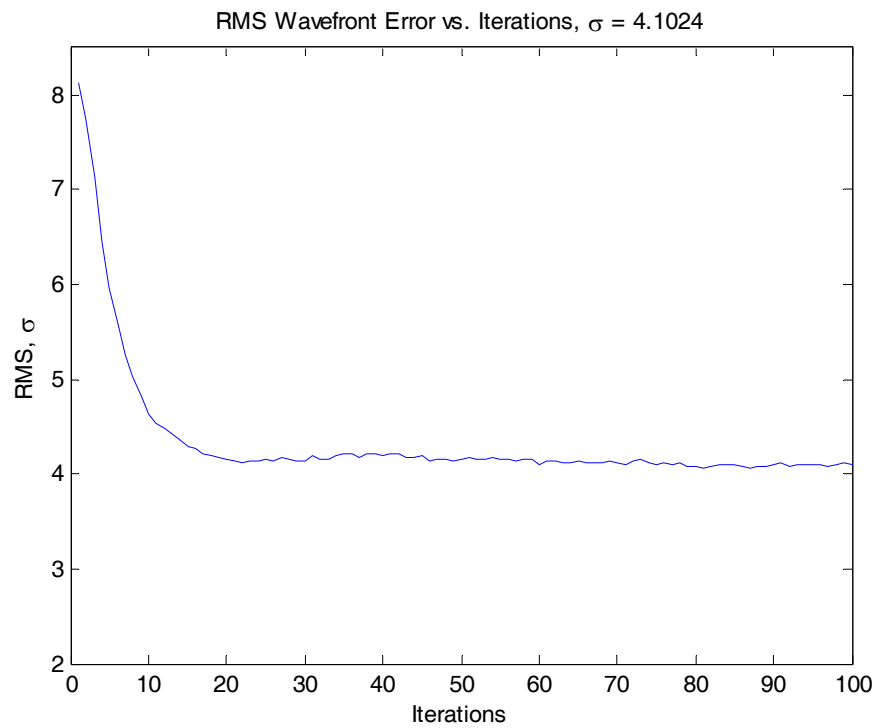


Figure 50 Classical Controller RMS Wavefront Error.

As can be seen, a steady state wavefront error was obtained after about 25 iterations.

Next, the robust controller was used with all the same settings and parameters. The only change was the replacement of the line of code representing the classical controller in Equation (6.6) with the code to represent the discrete robust controller in Equation (6.5). The wavefront estimation algorithms were identical. The peak-to-valley and RMS results from 100 iterations with the robust controller are shown in Figure 51 and Figure 52.

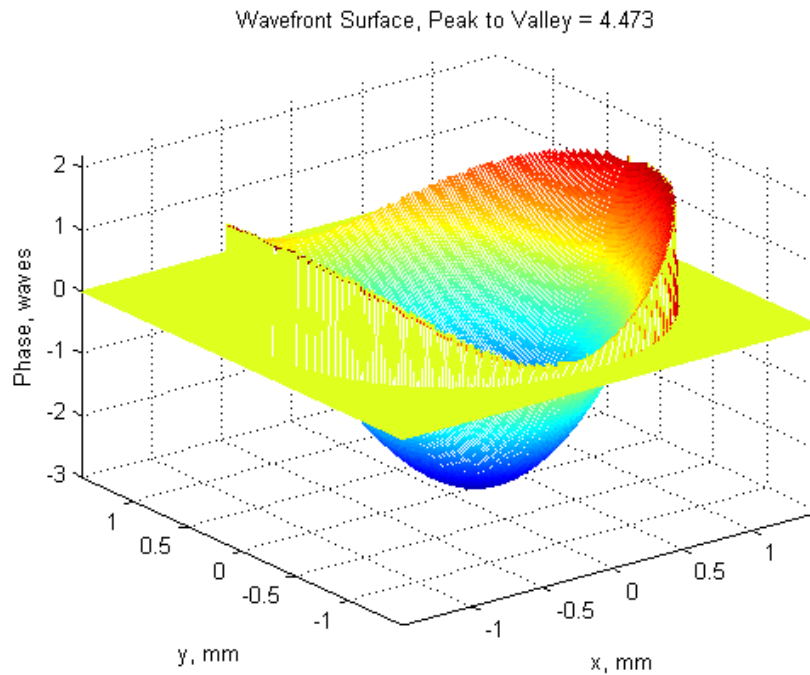


Figure 51 Robust Controller Peak-to-Valley Wavefront Error.

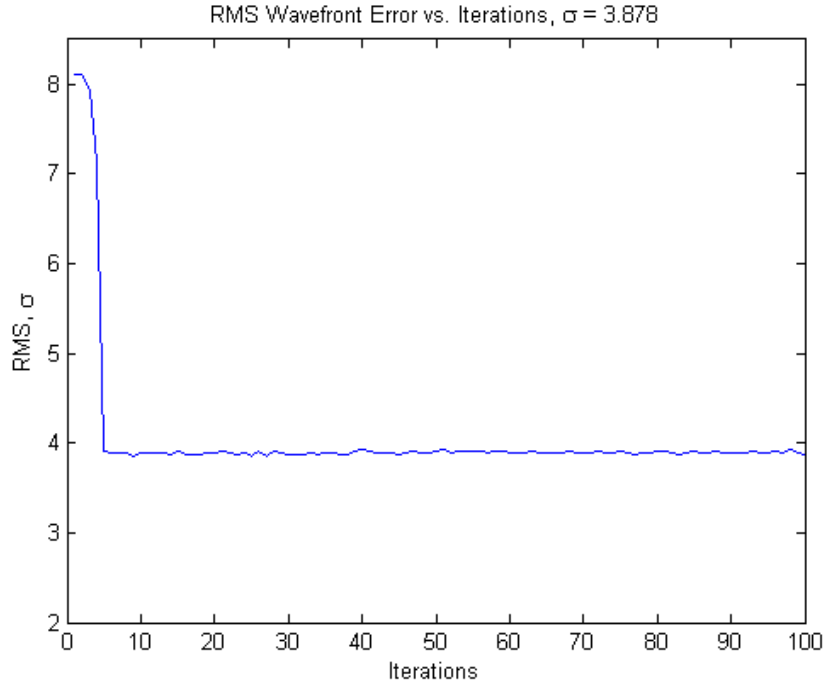


Figure 52 Robust Controller RMS Wavefront Error.

As seen in the plots, the robust controller outperforms the classical controller in peak-to-valley wavefront aberration, final RMS value, and the number of iterations required. Increasing the gain on the classical controller can improve the response time, but this also leads to instability. Other attempts to design robust controllers for AO testbeds have yielded lower absolute peak-to-valley and RMS values [9]. The purpose here, however, was not to achieve the lowest absolute error, but rather to experimentally verify the robust control synthesis procedures used on the analytical model. The improved performance of the robust controller over the classical controller is taken as verification of this approach. The higher error values obtained here are most likely the result of a rudimentary wavefront estimation algorithm. Improving the centroiding algorithm used for wavefront estimation is left for future work, but that work was outside the scope of this research.

## 2. Disturbance Rejection

Additional comparison simulations were run on the AO testbed with a disturbance on the control voltages applied to the deformable mirror. The disturbance used was a

sinusoidal input at varying frequencies. In each test case, the robust controller proved superior at suppressing the disturbance input while achieving the results obtained from the simulation with no sinusoidal disturbance. The following set of figures show results for each controller for two different disturbance frequencies, 1.3963 Hz and 6.2832 Hz. The final error results from the simulations are summarized in Table 4.

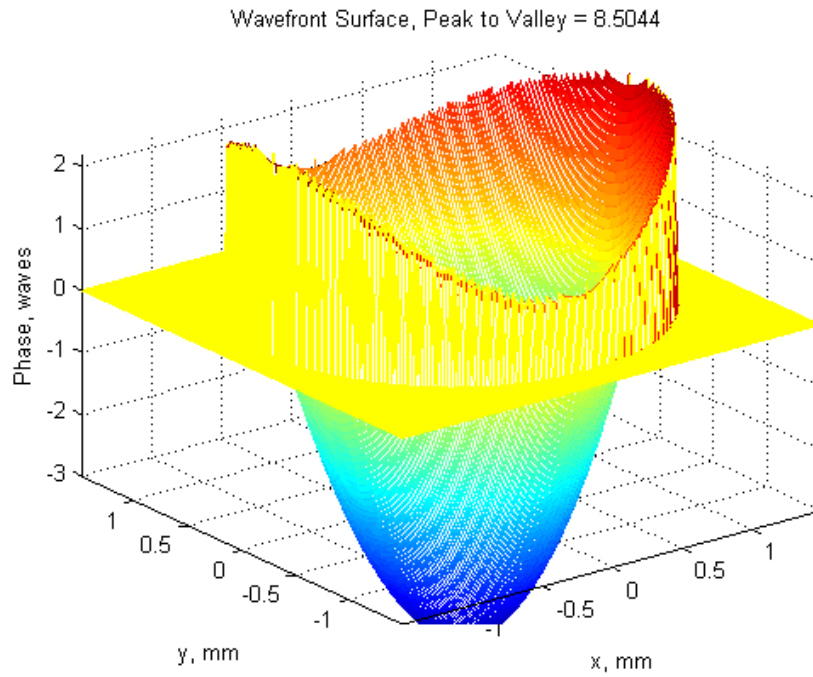


Figure 53      Classical Controller Peak-to-Valley Wavefront Error with 1.3963 Hz Disturbance.

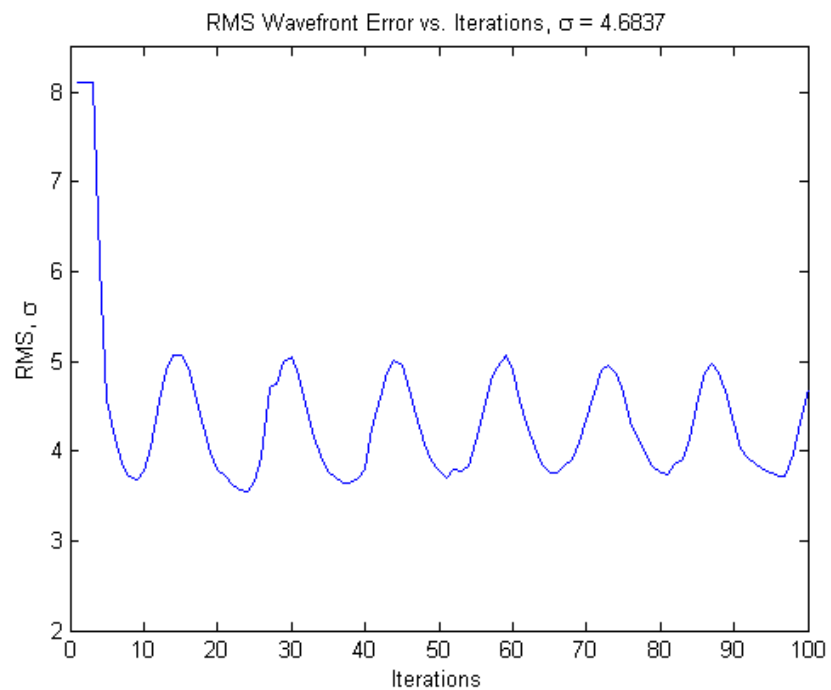


Figure 54 Classical Controller RMS Wavefront Error with 1.3963 Hz Disturbance.

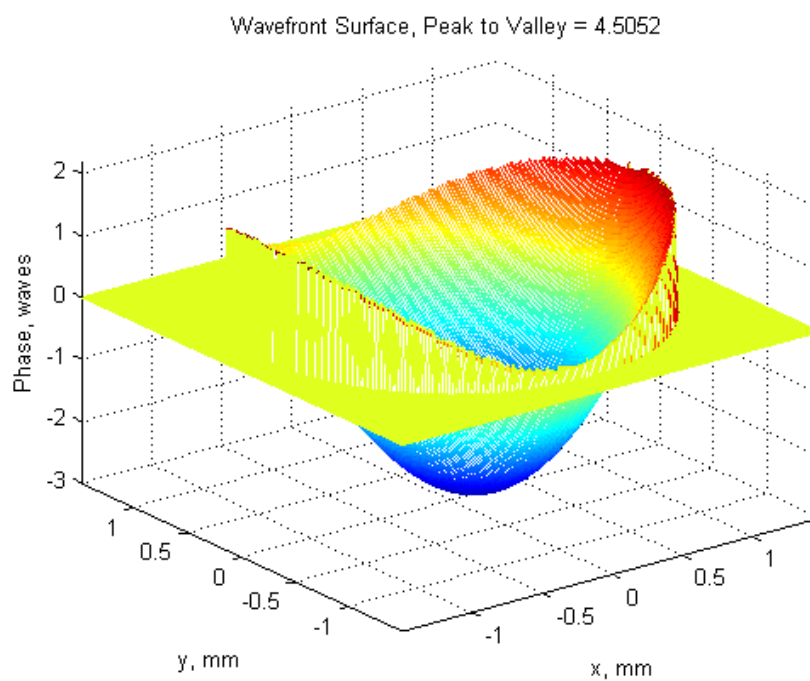


Figure 55 Robust Controller Peak-to-Valley Wavefront Error with 1.3963 Hz Disturbance.

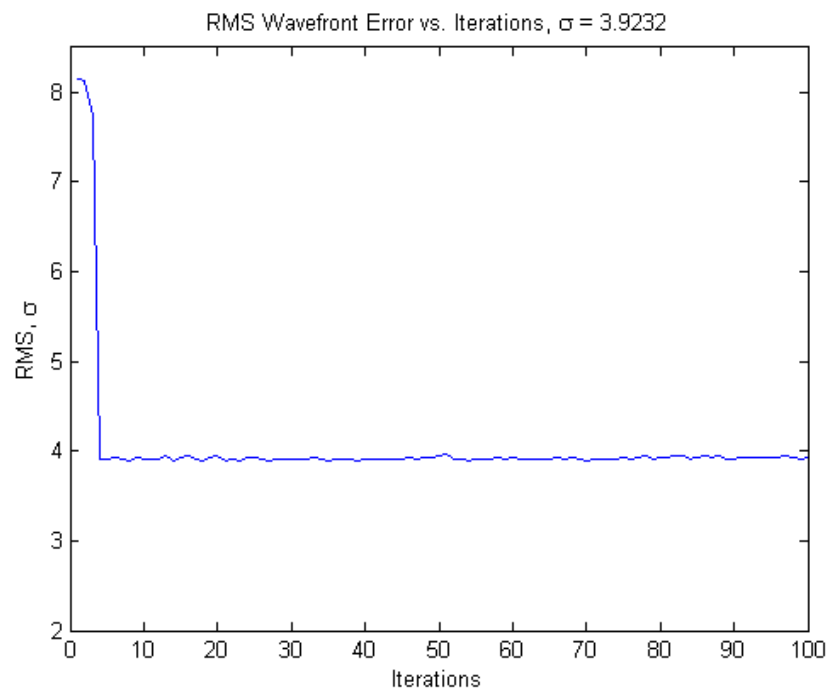


Figure 56 Robust Controller RMS Wavefront Error with 1.3963 Hz Disturbance.

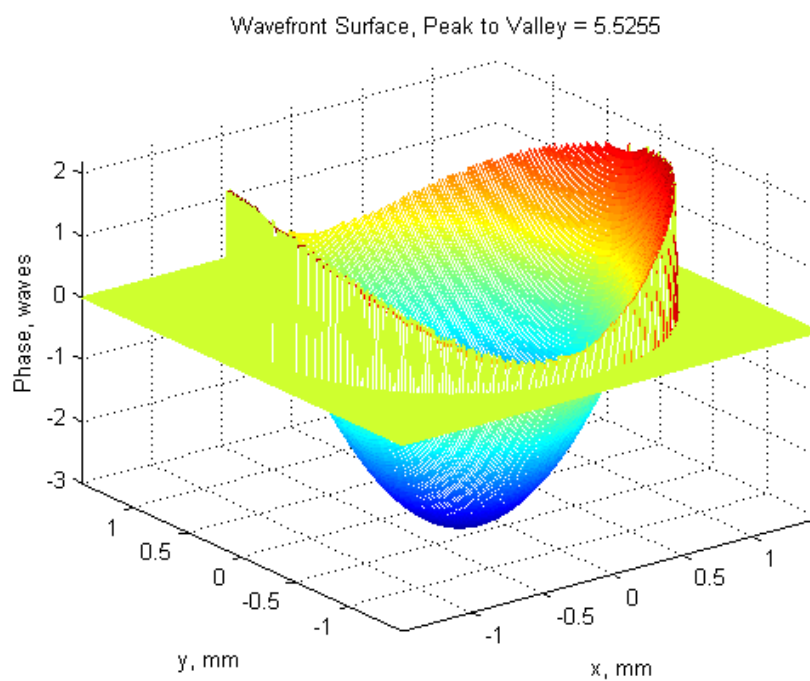


Figure 57 Classical Controller Peak-to-Valley Wavefront Error with 6.2832 Hz Disturbance.



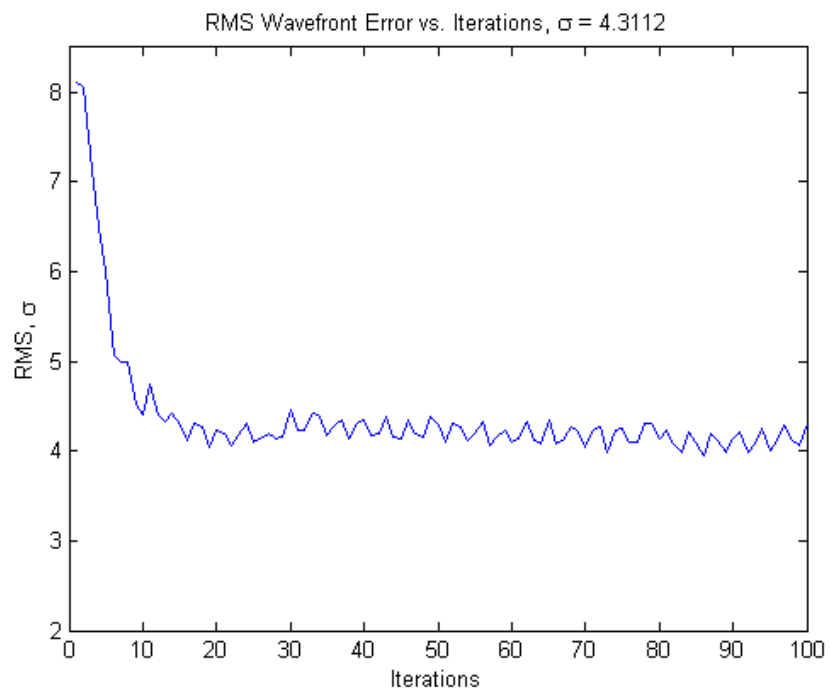


Figure 58 Classical Controller RMS Wavefront Error with 6.2832 Hz Disturbance.

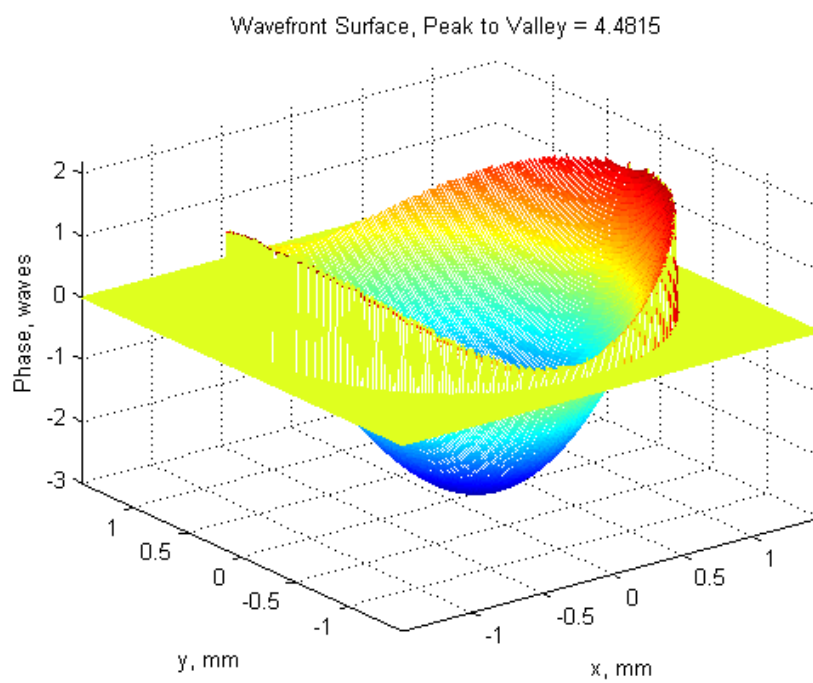


Figure 59 Robust Controller Peak-to-Valley Wavefront Error with 6.2832 Hz Disturbance.

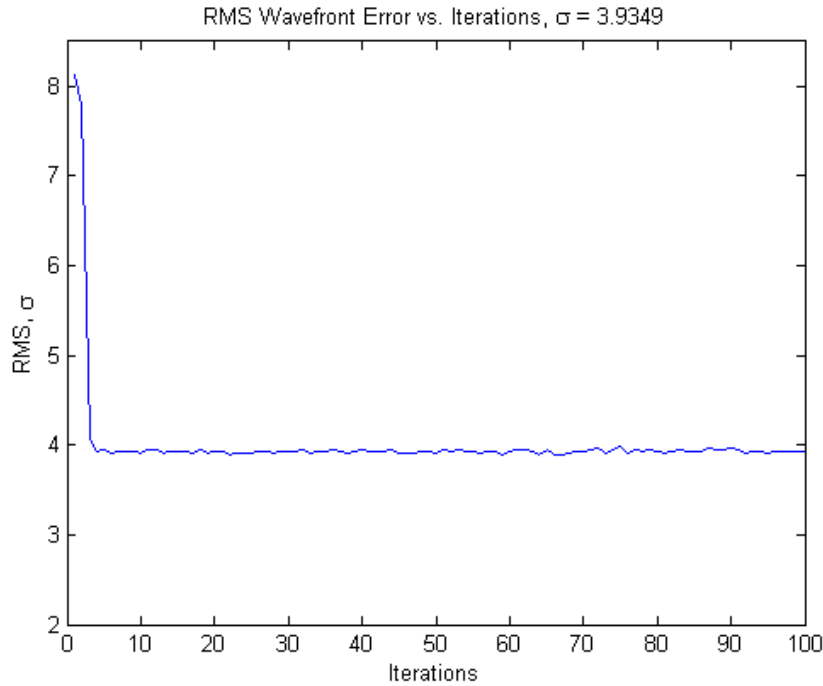


Figure 60 Robust Controller RMS Wavefront Error with 6.2832 Hz Disturbance.

	<u>Peak-to-Valley Wavefront Error</u>	<u>RMS Error (<math>\sigma</math>)</u>	<u>Iterations</u>
<b><u>1.3963 Hz Disturbance</u></b>			
Classical Controller	8.5044	4.6837	8
Robust Controller	4.5052	3.9232	4
<b><u>6.2832 Hz Disturbance</u></b>			
Classical Controller	5.5255	4.3112	20
Robust Controller	4.4815	3.9349	4

Table 4 AO Testbed Disturbance Rejection Simulations.

Clearly, the robust controller is better able to handle disturbances than the classical controller is. This is accomplished in fewer iterations as well. In each case, the robust controller achieved its steady state wavefront error in 4 iterations, whereas the classical controller took approximately 10 iterations and even then was not able to completely dampen the disturbance input. Similar results were obtained for other test frequencies. The additional benefit of the robust controller is that no a priori knowledge of the disturbance frequency was necessary. It handled all tested frequencies equally well. It is this ability of the robust controller to provide robust performance in the presence of uncertainty that makes it desirable for these applications.

## VII. SUMMARY, FUTURE WORK, AND CONCLUSIONS

### A. SUMMARY

This research has provided an important contribution to the field of control systems for adaptive optics systems. It has demonstrated the design of a robust controller for a complex AO system. While not the first use of  $H_\infty$  control for AO systems, it is the first analytical work for a space based AO telescope with a high degree of complexity due to the number of actuators, sensors, and states. To accomplish this, an innovative use of Zernike polynomials was used to perform model reduction. Zernike polynomials had previously not been used in this fashion with the intent of facilitating the design of a robust controller. This application was possible due to the fact that the sensor outputs for the AO system model consisted largely of Shack-Hartmann wavefront sensor slopes. Zernike polynomials are uniquely suited to describe this type of data.

An analytical model that originally had 997 inputs and 936 outputs was reduced to 21 inputs and 21 outputs. The reduction was performed by a Singular Value Decomposition approach and the Zernike polynomial approach, and the results were compared. Additionally, a Hankel singular value reduction was performed to reduce the number of states in the system from 332 to 240. Both input/output reduction approaches allowed the successful synthesis of a robust controller. The controller from the SVD reduced model had a closed loop control bandwidth between 20 and 24 Hz, while the controller from the Zernike reduced model had a closed loop control bandwidth between 15 and 19 Hz. Both of these bandwidths exceeded the required 10 Hz bandwidth that the existing classical control techniques were unable to achieve.

While classical controllers have many advantages and are much simpler to design and implement, the ever increasing complexity of AO systems and growing number of sensors and actuators means that alternative methods need to be developed. The work presented here has demonstrated that robust control techniques are worthy of further research for implementation in these types of systems.

Finally, the robust controller synthesis design techniques used for the complex analytical model were experimentally verified on an AO testbed. While the AO testbed system was much simpler than the analytical space telescope model, the same techniques and algorithms used for the analytical model were used for the testbed.

Both controllers achieved similar absolute wavefront correction results; however, the robust controller was able to achieve the steady state wavefront error in only 4 iterations, whereas the classical controller took approximately 25 iterations. The real advantage of the robust controller was seen in the rejection of a disturbance input. The robust controller was essentially impervious to the disturbance input in the test cases. This was possible for any desired sinusoidal disturbance frequency without any a priori knowledge of the disturbance frequency. For classical control, a notch filter can be used for disturbance rejection. However, to design the filter, the disturbance frequency has to be known accurately. The superior performance of the robust controller on the testbed versus the classical controller is further verification that the techniques implemented in this research are valid.

## **B. FUTURE WORK**

A number of issues arose during this research, demonstrating areas where further work could be accomplished. The first suggestion for additional research would be to experiment with different numbers of Zernike polynomials. Twenty-one polynomials were used in this research, which go to seventh order aberrations. Using more polynomials could improve accuracy of the wavefront estimation. The tradeoff would come in increased complexity and possibly longer calculation times due to the larger number of polynomials. Additionally, the Zernike polynomials could be modified for an annular ring as set forth in [26] to account for the central hole in the primary mirror.

Another possibility would be to experiment with performing a state reduction at different stages in the process. In this work, a state reduction was performed immediately after the inputs and outputs were reduced. Alternative approaches would be to perform state reductions on the original full plant, the augmented 2-input, 2-output system model, the synthesized robust controller, or any combination of multiple state reductions at these

stages. An important consideration for the segmented space telescope model is that it was originally given in modal form where the  $A$  matrix had a convenient block diagonal structure. A state reduction destroys this structure, so easy identification of the natural frequencies is no longer possible.

Additionally, the robust controller synthesized in the research was calculated based on a direct  $H_\infty$  method. Other robust controller synthesis techniques exist such as the  $\mu$ -synthesis method, which might yield promising results. This would also allow further research into ways of introducing uncertainty into the segmented space telescope model.

On the adaptive optics testbed, refinement of the wavefront estimation algorithms would most likely provide lower absolute error measurements. There are also a number of other classical and optimal control algorithms that could be implemented and compared on the testbed. Upgrading the Basler camera on the testbed used for wavefront sensing to a higher frames per second rate would also improve the system performance.

Eventually, the techniques presented here could be implemented on a testbed with a segmented primary optic. The Spacecraft Research and Design Center has such a mirror for future work. Implementing robust control techniques on this mirror could be done in conjunction with the research currently being performed at the SRDC on an improved wavefront sensing technique known as Redundant Spacings Calibration [1].

## C. CONCLUSIONS

This research has contributed to the state-of-the-art in the following areas:

1. An  $H_\infty$  robust control technique has been used for surface control of a flexible space telescope model including structural dynamics.
2. Robust control techniques have been able to provide a desired control bandwidth that was not possible with classical control.

3. A new model reduction technique using Zernike polynomials and singular value decomposition has been developed. This technique has been found to provide better performance to reduce the wavefront aberration in the space telescope model.
4. A robust control technique has been applied experimentally to the adaptive optics testbed of the Naval Postgraduate School Spacecraft Research and Design Center. The robust control technique has been found to be superior to classical control in response time and disturbance rejection.

$H_\infty$  robust control techniques offer many advantages for complex AO systems, particularly those that are subject to high amounts of model uncertainty, such as lightweight segmented space telescopes. As future system become more complex, and performance requirements become more stringent, the techniques discussed in this dissertation will become increasingly important.

It is important to note that just because a robust controller *can* be designed for a particular system, this does not necessarily mean that it *should*. Classical control methods, optimal control techniques, and even adaptive controllers all offer certain benefits. The ultimate solution will most likely be a combination of approaches to reduce overall system risk, guarantee stability, and maximize performance. In the case of space systems, the extremely high development and launch costs require multiple levels of redundancy to prevent loss. The techniques explored in this research will undoubtedly be applicable to future designs.

## LIST OF REFERENCES

- [1] R. Eastwood, A. M. Johnson, and A. Greenaway, "Calculation and correction of piston phase aberration in synthesis imaging," *Journal of the Optical Society of America*, future publication (2008).
- [2] NASA image, retrieved November 14, 2008, [http://meta-religion.com/Astronomy/images/Exploration/hubble\\_sucesor\\_3.jpg](http://meta-religion.com/Astronomy/images/Exploration/hubble_sucesor_3.jpg).
- [3] M. Allen, "Wavefront Control for Space Telescope Applications Using Adaptive Optics," M.S. thesis, Naval Postgraduate School, Monterey, CA, 2007.
- [4] R. A. Gonsalves, "Nonisoplanatic imaging by phase diversity," *Journal of the Optical Society of American*, vol. 19, no. 7, pp. 493-495, April 1994.
- [5] R. K. Tyson, *Principles of Adaptive Optics*, Ed. 2, San Diego: Academic Press, 1998.
- [6] B. W. Frazier and R. K. Tyson, "Robust Control of an Adaptive Optics System," *IEEE Proceedings of the thirty-fourth southeastern symposium on system theory*, pp. 293-296, November 2002.
- [7] B. W. Frazier, R. K. Tyson, J. Ackman, and M. Smith, "Closed loop results of a compact high-speed adaptive optics system with  $H_\infty$  control," *Proceedings of SPIE*, vol. 5169, pp. 37-42, 2003.
- [8] B. W. Frazier, J. Roche, R. K. Tyson, Y. P. Kakad, and B. G. Sherlock, "Robust control of an adaptive optical system," *Proceedings of the Institution of Mechanical Engineers*, vol. 218, pp. 353-358, 2004.
- [9] B. W. Frazier, R. K. Tyson, M. Smith, and J. Roche, "Theory and operation of a robust controller for a compact adaptive optics system," *Society of Photo-Optical Instrumentation Engineers*, vol. 43, no. 12, pp. 2912-2920, December 2004.
- [10] K. Li, E. B. Kosmatopoulos, P. A. Ioannou, and H. Ryaciotaki-Boussalis, "Large Segmented Telescopes, Centralized, Decentralized, and Overlapping Control Designs," *IEEE Control Systems Magazine*, pp. 59-72, October 2002.
- [11] D. W. Miller and S. C. O. Grocott, "Robust control of the Multiple Mirror Telescope adaptive secondary mirror," *Society of Photo-Optical Instrumentation Engineers*, vol. 38, no. 8, pp. 1276-1287, August 1999.
- [12] M. Whorton and G. Angeli, "Modern control for the secondary mirror of a Giant Segmented Mirror Telescope," *SPIE Future Giant Telescopes Conference*, SPIE 4840-23, August 2002.

- [13] L. Baudouin, C. Prieur, F. Guignard, and D. Arzelier, "Robust control of a bimorph mirror for adaptive optics system," *Optical Society of America Journal of Applied Optics*, vol. 47, no. 20, pp. 3637-3645, July 2008.
- [14] B. Wie, Q. Liu, and K. W. Byun, "Robust  $H_\infty$  Control Synthesis Method and Its Application to Benchmark Problems," *AIAA Journal of Guidance, Control, and Dynamics*, vol. 15, no. 5, pp. 1140-1148, September-October 1992.
- [15] R. Y. Chiang and M. G. Safonov, " $H^\infty$  Synthesis Using a Bilinear Pole Shifting Transform," *AIAA Journal of Guidance, Control, and Dynamics*, vol. 15, no. 5, pp. 1111-1117, September-October 1992.
- [16] K. Zhou and J. C. Doyle, *Essentials of Robust Control*, Upper Saddle River, New Jersey: Prentice-Hall, Inc., 1998.
- [17] J. B. Burl, *Linear Optimal Control*, Menlo Park, California: Addison Wesley Longman, Inc., 1999.
- [18] A. Carrier, "Modeling and Shape Control of a Segmented-Mirror Telescope," Ph.D. dissertation, Stanford University, Palo Alto, CA, 1990.
- [19] Flexible Optical BV (OKO Technologies), *Adaptive Optics Product Guide*, Grafische Communicatie, Rotterdam, the Netherlands, pp. 51-54, 2006.
- [20] R. Y. Chiang, "Robust Control: Toolbox, Theory, and Applications," course notes, Spring 2006.
- [21] V.N. Mahajan, "Zernike Annular Polynomials and Optical Aberrations of Systems with Annular Pupils", *Supplement to Optics & Photonics, Optical Society of America*, vol. 5, no. 11, pp. 8125-8127, December 1994.
- [22] M. Born and E. Wolf, *Principles of Optics*, Ed. 7, Cambridge: Cambridge University Press, 1999, pp. 905-910.
- [23] F. Roddier, *Adaptive Optics in Astronomy*, Cambridge: Cambridge University Press, 1999, pp. 27-29.
- [24] J. C. Wyant, Zernike, University of Arizona, College of Optical Sciences, retrieved November 14, 2008, <http://www.optics.arizona.edu/jcwyant/zernikes/ZernikeEquations.htm>.
- [25] A. Roorda, "Optics and Optical Quality of the Human Eye," University of California Berkeley, retrieved November 15, 2008, [http://vision.berkeley.edu/roordalab/Pubs/Optics\\_of\\_the\\_Eye.ppt#368,77,Slide 77](http://vision.berkeley.edu/roordalab/Pubs/Optics_of_the_Eye.ppt#368,77,Slide 77).



- [26] V. N. Mahajan, "Zernike annular polynomials for imaging systems with annular pupils," *Journal of the Optical Society of America*, vol. 71, no. 1, pp. 75-85, January 1981.
- [27] W. H. Southwell, "Wave-front estimation from wave-front slope measurements," *Journal of the Optical Society of America*, vol. 70, no. 8, pp. 998-1006, August 1980.
- [28] M. G. Safonov and R. Y. Chiang, "A Schur Method for Balanced Model Reduction," *IEEE Trans. On Automat. Contr.*, vol. AC-2, no. 7, pp. 729-733, July 1989.
- [29] R. K. Douglas, R. H. Chen, and J. L. Speyer, "Linear System Input-Order Reduction by Hankel Norm Maximization," *AIAA Journal of Guidance*, vol. 27, no. 1, pp. 150-154, June 2003.
- [30] R. Cristi, "Lectures on Robust Control," Department of Electrical and Computer Engineering, Naval Postgraduate School, Winter 2008, last retrieved February 2009, available at [http://web.nps.navy.mil/~cristi/robust\\_control/web/lectures.htm](http://web.nps.navy.mil/~cristi/robust_control/web/lectures.htm).

THIS PAGE INTENTIONALLY LEFT BLANK

## **INITIAL DISTRIBUTION LIST**

1. Defense Technical Information Center  
Ft. Belvoir, Virginia
2. Dudley Knox Library  
Naval Postgraduate School  
Monterey, California